Annual Report Hahn-Meitner-Institut / Helmholtz-Zentrum Berlin 2007/2008

SELECTED RESULTS

HELMHOLTZ ZENTRUM BERLIN
für Materialien und Energie

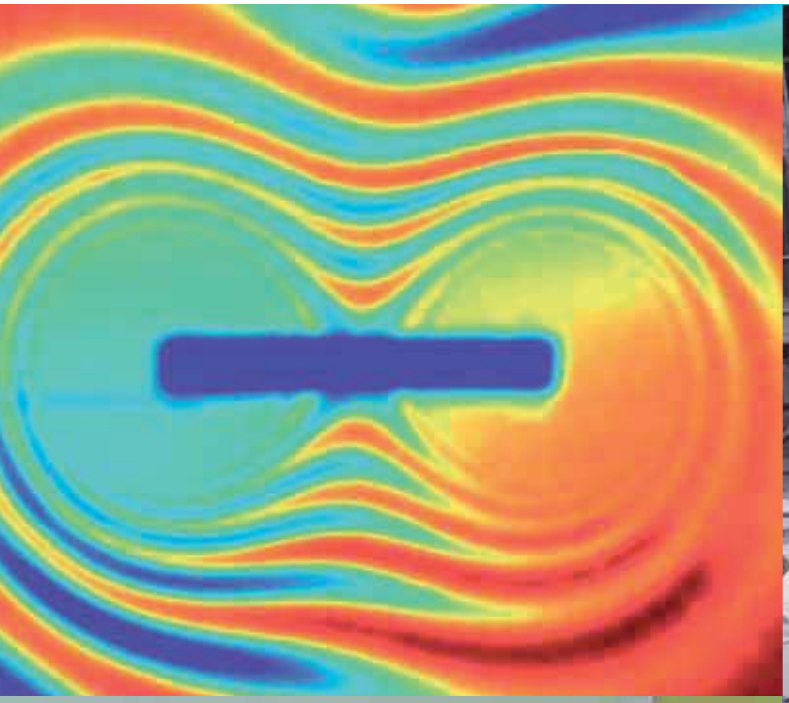

Legend to Cover Figures:

top left: Imaging of magnetic fields with polarized neutrons

top right: 50 years ago - BER I under construction

bottom left: $Cu(In,Ga)Se_2$ thin film solar cells mounted on the test satellite Delfi-C3

bottom right: Participants of the summer student programme learning about special analytics

Annual Report Hahn-Meitner-Institut / Helmholtz-Zentrum Berlin 2007/2008

SELECTED RESULTS

Table of contents

Foreword

The years 2007 and 2008, which this activity report covers, turned out to be of prime importance for the future of the Institute: not only were they the last years before the next Program-Oriented-Funding (POF)-evaluation but they were the years, which have led to the foundation of a new institute, the Helmholtz-Zentrum Berlin für Materialien und Energie (HZB to be formed by the merger of HMI and BESSY. This new Centre has started to operate on January 1st 2009.

The merger of HMI and BESSY, the two institutions in Berlin operating large facilities, had been in the discussion with strongly varying intensity and perspective over many years. It was in the last couple of years only, that the discussions about merging HMI and BESSY intensified and found support on the political level so that a clear perspective for realisation emerged. The necessary preparations on the scientific, legal and structural level required a strict plan in order to be ready on December 31st 2008 for the start of the new merged Centre on January 1st 2009. The resulting timetable also included the preparation of a Structure and Development Plan for the new Centre, which was evaluated by an international panel led by Professor R. Eichler then head of Paul-Scherrer-Institut (PSI). The panel supported the plan and made very helpful suggestions for the program and the structure of the new Centre. In a next step the Hahn-Meitner Institut Berlin (HMI) changed its name to Helmholtz-Zentrum Berlin für Materialien and Energie in preparation for the merger. This was a difficult step, because the old name stood for nearly 50 years of successful scientific history in the spirit of the two outstanding scientists Otto Hahn and Lise Meitner. With the legal registration of the new merged Centre in November 2008 the formal steps were completed everything was ready for the start on January 1st 2009. To be really ready for the new start, my successor Prof Dr. Anke Pyzalla took office as the new Scientific Director and Chief Executive on October 1st 2008.

Despite of all these fundamental changes occurring in the last two years science and service to the community flourished as the report clearly shows. Let me emphasize a few highlights: in the Solar Energy Division Dr. Bär has been appointed as a Junior Professor for Thin Film PV jointly with the Brandenburgische Technische Universität Cottbus and we have finally founded the PV-Kompetenz-Zentrum Berlin (Centre of excellence for thin film and nanotechnology for photovoltaics Berlin) as a separate structure within HZB. This allows us to make contracts

Airbus A 300: Researchers at HZB on a parabolic flight

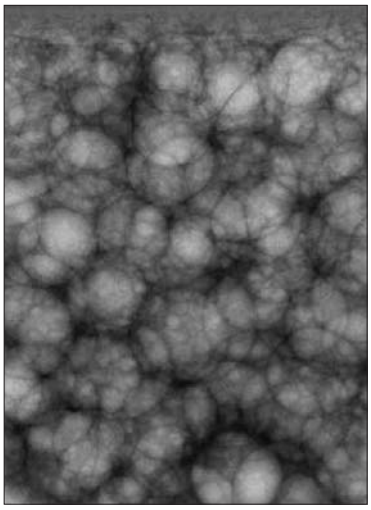

X-ray of a liquid metal foam

Spot on – Remembering 1998 when BESSY II started user operation

with industry for further joint development of PV technology including the provision of industrial scale equipment by the partners. A further step forward for our own technology department was moving of all members and laboratories into one coherent location. In order to prepare for a widening of our Renewable Energy program and to tackle a challenge of growing concern we had a very successful international workshop about photocatalytic fuel production. The workshop showed, that a our knowledge and experience in photovoltaics is an ideal base for such a program.

In the Structural Research Division the central task of serving the user community through BENSC continued to be very successful: the number and the quality of the proposals is steadily increasing, which is also reflected in the resulting number of high impact papers. In house research has produced very nice examples of the complementary use of neutrons and photons showing the strength and potential of this approach, which is now one of the main strategic pillars of the new Centre. Our instrument renewal program has been continued along the recommendations of the international advisory group. We are convinced that this will enhance the facilities performance significantly and enable new science to be tackled. A highlight of this program is the complete rebuilding of our time-of-flight instrument NEAT, which with its unique possibilities will bring NEAT back into the class of the leading instruments of this type. The construction of our High-Field-Magnet is progressing well after extended studies of the stability of the SC-wires. This ensures that the wires to be used and the making of the cable-in-conduit will meet the specifications for the performance of the magnet.

There were chances for celebrations in 2008, too: in June 2008 we celebrated the 50 anniversary of reactor based neutron research in Berlin. Many of our present users and colleagues from other Neutron Research Centres were attending the meeting and exchanged memories and experiences from the past to the present days.

The last but definitely not the least important task we had to deal with, were the preparations for the new round of POF-evaluations, which will take place in early 2009. All parts of the new HZB will be evaluated in 2009. The task has been as demanding as 5 years ago, but the resulting programs look very good thanks to the hard work of many of the scientists.

The motivation and the commitment of all members of the institute made all the achievements in research and service to the science communities possible. Many thanks to you! We also thank our associates for the continued support and the steady funding.

This is the last report, which I am responsible for, since I shall leave in mid 2009 after more than 15 years in responsible positions at HMI and HZB. It is a pleasure for me to see the new centre operating and I am sure it will reach its goals and will continue to provide excellent conditions for doing research. I wish all the staff the very best, the board of directors good luck and the HZB a splendid future.

View into the Neutron Guide Hall II at research reactor

Preparing a fuel cell for tomograhic imaging

Scientific Director (CEO) Prof. Dr. Michael Steiner (left)

Administrative Director Dr. Ulrich Breuer (right)

News and Activities 2007/2008

Prof. Dr. Anke Rita Kaysser-Pyzalla

Prof. Dr. Anke Rita Kaysser-Pyzalla took office as Scientific Director and Chief Executive of the new centre HZB on October 1st 2008.

After studying Mechanical Engineering and Mechanics Anke Kaysser-Pyzalla graduated at the TU Darmstadt and received a Dr.-Ing. degree in 1995 with a thesis in materials science at the Ruhr-Universität Bochum. As a Post-Doc she assumed responsibility for an instrument at the BER II reactor of the Hahn-Meitner-Institut. She then joined the TU Berlin as a group leader at the "Institute for Materials Science and Technology". In 2001, Anke Kaysser-Pyzalla submitted her "Habilitation", which focused on material characterisation with synchrotron radiation and neutrons, and received her "venia legendi" in materials science at the Ruhr-Universität Bochum. She then moved to Austria to the TU Wien to become a full professor for "Materials Selection, Materials Testing and Joining" at the "Institute of Materials Science and Technology" in 2003. Already two years later she became director and executive head of the department "Materials Diagnostics and Steel Technology" at the Max-Planck-Institut für Eisenforschung GmbH, Düsseldorf. Anke Kaysser-Pyzalla has been elected as a member of the academies "acatech" and the "Österreichische Akademie der Wissenschaften".

Anke Kaysser-Pyzalla's research interests are in materials science, in particular method developments for materials characterisation with synchrotron radiation and neutrons, function/property relations of materials, materials development and optimisation. She has served in various scientific committees, e.g. as vice-chair of the Photon Science Committee at DESY, in the ESRF User Organisation, in proposal selection committees at BESSY, ESRF, and FRM II. She is editor of the Journal of Applied Crystallography and member of the senate of the Deutsche Forschungsgemeinschaft DFG, the "Wissenschaftliche Kommission Niedersachsen", and a panel of the European Research Council.

In her function as the new Scientific Director for Research with Photons and Neutrons and as Chief Executive of the Helmholtz-Zentrum Berlin (HZB), Anke Kaysser-Pyzalla is determined to give a new impetus on the complementary use of neutrons and synchrotron radiation in research, as well as in further developing the HZB with its now two large scale facilities as a leading science centre for an international user community. She highlights the potential of a strong in-house scientific programme in magnetism, functional materials and energy research, and therefore strongly welcomes increasing co-operations between scientists who are focusing on energy research and those with neutron and photon research expertise. She sets a special accent to further strengthen the strong ties to universities,

Anke Kaysser-Pyzalla, new Scientific Director and Chief Executive of the HZB

e.g. through joint appointments of institute heads, by establishing joint working groups, and through groups headed by junior scientists, such as Helmholtz Young Investigator Groups.

Dr. Ina Helms, Head of the public relations department and HZB press relations officer

Ina Helms

Since 1st January 2007, the public relations department is headed by Ina Helms, a chemist and science journalist. She replaces Thomas Robertson, who went into partial retirement one year ago. Ina Helms worked freelance for various editorial and press departments, like the Technische Universität Berlin, Die Welt or the Max-Planck-Gesellschaft. She was formerly employed as editor at the Brockhaus-Lexikon Verlag.

Dr. Mirko Vogel was awarded the HMI Communication Award for his dissertation about organic solar cells.

Mirko Vogel

Mirko Vogel has won the HMI Communication Award 2007.
The 30-year old physicist illustrated in his dissertation “solar cells, malicious interfaces and how scientists fool them” the importance of interfaces in organic solar cells between electrodes and active matters(materials).

Prof. Dr. Susan Schorr, scientist at HZB and professor for Geo-Material Sciences

Susan Schorr

Susan Schorr, scientist at the department SE3, has been appointed professor for Geo-Material Sciences at the Freie Universität Berlin. She assumed office in February 2008.
In her function at the university, she is in charge of an Ph.D student who will do his research in the field of technology relevant structure analyse at the HZB.

Prof. Dr. Marcus Bär, Leader of the ‘Young Investigator Group Interface design’ at the Solar Energy department

Markus Bär

Since November 2007 Marcus Bär has been leading the new founded ‘Young Investigator Group Interface design’ at the Solar Energy department. The 32-year old engineer, formerly employed at the University of Nevada, USA, analyses advancements of thin-film solar cells at the HZB. In cooperation with the BTU Cottbus, he will give lectures about his research results and experiences.

Dr. Rutger Schlatmann, new coordinator of the PVcomB – Competence Centre Thin-Film- and Nanotechnology for Photovoltaics Berlin

Rutger Schlatmann

On 1st May 2008 Rutger Schlatmann took office as coordinator of the newly founded PVcomB – Competence Centre Thin-Film- and Nanotechnology for Photovoltaics Berlin .
Rutger Schlatmann was formerly employed at Helianthos, where he was in charge of various F& E-aspects, as patents or strategic business-planning.

HMI and BESSY team up to showcase their work

The merger of Hahn-Meitner-Institut and BESSY had hardly been made public when both institutes decided to get together to present their work at the 2007 “Long Night of Science”, the joint open day of the scientific institutes in Berlin. The HMI site at Wannsee remained closed and anything of interest – models, lab equipment, and other examples of the work undertaken there – were brought to Adlershof where they filled all the empty space in the experimental hall and the lobby of BESSY. Thus, in some areas, the blue HMI T-shirts outnumbered the green ones worn by the BESSY team.

For HMI, the joint presentation was not only a sign of the closer ties between the two institutes, it was also an opportunity to present its work to the huge audience visiting Adlershof during the Long Night each year. More than 4,000 visitors – vastly more than could usually be expected to visit the Wannsee site – had the opportunity to discover how neutrons reveal the structure of matter and how new solar cells are developed. Of course, those who only visited the HMI exhibition at BESSY missed some of the main attractions: the experimental halls around the research reactor and the proton therapy accelerator. So, in 2008, the

2007: HMI and BESSY – “a new option for Berlin” was the motto of the first joint presentation at the Long Night of Science.

2007: The blue team and the green team: in some parts of BESSY’s experimental hall there were more blue HMI T-shirts than green BESSY ones.

2008: Leading the way between partners to be

institute – now renamed Helmholtz-Zentrum Berlin für Materialien und Energie – opened its doors at Wannsee once again, presenting the instruments at the reactor, the proton therapy accelerator and many, many more labs in the Structure Research and Solar Energy Divisions. But since it was clear at that point that BESSY and the former HMI would become one institute in 2009, there was also an exhibition about the activities at Wannsee in the BESSY lobby. Preparing this extensive programme was hard work for the whole HZB team. But it was worth it: 2,200 people visited the institute at Wannsee and many more had the chance to learn about neutrons, proton therapy and solar energy during their visit to BESSY.

2008: Science enthusiasts surge onto the Helmholtz-Zentrum campus at Wannsee.

2008: Watching a 3D tomography presentation

“Sun & Science” – The Late summer Party

For the first time, on September 26th, the staff of BESSY and HZB celebrated their annual summer party together. The diverse open-air program combined on stage a mix of science shows, interactive games and live music as well as dance performances. At the same time, the visitors enjoyed the catering and participated in various activities, with bull-riding as a highlight.

Members of both institutes with their family and friends as well as neighbours enjoyed an entertaining late summer afternoon at the HZB Campus Wannsee.

Music from the Mia Carla Trio

Soap bubbles experiment

Get together

Summer Student Programme

Summer students in a photovoltaics laboratory

"What is the everyday life of a scientist like?" This and many more questions can be answered during the eight-week Summer Student Programme at Helmholtz-Zentrum Berlin für Materialien und Energie (HZB). Advanced students from physics, chemistry or engineering are invited to participate in the programme that will provide access to the daily work of the scientists. Further insights will be given by guided tours and lectures which will be held on the diverse research topics covered by the institute, in the two main areas of solar energy and structural research. This international programme will be held in English.

In the summers of 2007 and 2008, participants from 11 different countries came together and worked with the scientists here in Berlin-Wannsee and Berlin-Adlershof. The 20th anniversary of the Summer Student Programme was celebrated in 2008, and in the last two years the programme has been more successful than ever with more than 30 students attending each year. 2008 was the first time that scientists from BESSY participated and offered projects at the synchrotron source. All supervisors prepared projects and during July and August students took responsibility for their own research, working in small groups or individually, but with the support of the supervisors. All the students benefited from the programme and some exciting projects led to many interesting results. In the last two years, students of physics, chemistry, electronic engineering, chemical engineering, industrial engineering, computer science and materials science have joined the programme and it is notable that there have been a significant number of female students.

Kids & Youth

Science can be exciting, even before going to university. The HMI offered a variety of possibilities in 2007 for youthful visitors to become "young scientists".

Cool girls: what happens to a balloon in liquid nitrogen (minus 196° C)

26th April 2007: Girl's day

Girls'Day provides female pupils with an opportunity to gain practical insights into the world of work, particularly in technical and technology-related fields. The focus is on hands-on practical experience. The HMI supports this activity with scientific practice guided by female researchers.

20th September 2007 "Jugend Forscht"

"Jugend forscht" (young researcher) is a national initiative to promote science in the age group of pupils. The winners of the 2007 competition visited the HMI, after they met with the German chancellor Angela Merkel.

21st September 2007 BundesUmweltWettbewerb

The BundesUmweltWettbewerb (a nationwide environmental competition) aims to promote knowledge about the environment and to further budding creativity and initiative in the tackling of environmental issues. It is conducted by the Federal Ministry for Education and Research (BMBF). The award ceremony 2007 was hosted by the HMI.

Tough theory: studying and discussing the periodic table of elements

School Lab

Girls in the School Lab

Since 2007 the HZB-School Lab has largely extended its spectrum of activities and has attracted more and more students of primary and secondary schools from the Berlin-Brandenburg region, other German states, and neighbouring European countries like Denmark. On two days per week the School Lab now hosts and organises so-called project days, when school classes carry out experiments on topics such as magnetism, superconductivity, interference, solar energy, and materials research. In 2008 more than one thousand students have used the opportunity to visit the School Lab. To meet the increasing demands of primary schools, our program was complemented by special activities for the very young students.

In 2007 a weekly student workshop ("Schüler AG") was founded. Later on the workshop was split into one group for primary school and one for secondary school students to account for the different age and skills of the students. For their studies on ferrofluids the workshop members Timo Stein and Fabian Nickel were awarded the first prize of the regional Berlin Jugend forscht competition 2007. In the subsequent national Jugend forscht competition they were awarded the special prize of the Deutsche Physikalische Gesellschaft. In 2008 Timo Stein and Christopher Förster contributed a study on cosmological radiation to the Jugend forscht competition and were awarded the first prize for physics of the regional Berlin competition and the first prize for geosciences and astrophysics of the national competition, where in addition they were awarded the special prize of the Astronomische Gesellschaft Deutschland.

The School Lab also participated in events apart from the regular activities. In 2007 the lab team together with other Helmholtz School Labs organized a joined hands-on exhibition in the European Parliament in Brussels. In 2007 and 2008 the lab contributed to the Wissenschaftssommer in Leipzig and to the Lange Nacht der Wissenschaften with various programs. Recently it created and performed a play at Science on Stage in Berlin, an event meant to make science meet education. In the framework of JugendKulturService activities were organised during school vacations. By hands-on-experiments trainees and volunteers of the HZB were introduced to the scientific scope of the HZB.

School Lab (Michael Tovar) at Science on Stage

Die Lange Nacht der Wissenschaften 2008 provided an opportunity to exchange hands-on-experiments for visitor groups and to cooperate in other areas with BESSY. In 2009 a considerable part of the School Lab activities will be the coordination and development of further joint activities with BESSY with the medium-term aim to establish a School Lab on the BESSY campus.

Technology transfer for photovoltaics: the new PVcomB

In April 2007, the HMI and the TU Berlin signed a 'Memorandum of Understanding' (MoU) to start the new PVcomB – Competence Centre Thin-Film- and Nanotechnology for Photovoltaics Berlin. The driving force behind the new competence centre is the rapid boom of the solar industry, with the key area lying in the new East German federal states. Several companies have currently begun constructing production facilities for innovative thin-film solar cells. "These future technologies must be successfully established and developed over the long-term in Germany", emphasizes Prof. Michael Steiner. Together with the research institutes in Berlin, eight renowned industrial companies signed the MoU and will support the center's construction. Additional companies have already announced major interest in participating in a collaboration. Thus being brought on its way, the PVcomB commenced work in May 2008, when its new director, Dr. Rutger Schlatmann (see people p. 9), took up office. The first challenge was to find a building and infrastructure for the new centre as well as get financing and the organizational structure on its way. At the end of 2008, the location was finally found. A building of the Center of Photonics and Optical Technologies, located at the science and technology park Adlershof (WISTA), will be refurbished. Once finished in early summer 2009, the PVcomB will have around $500 m^2$ laboratories plus office space at its convenience.

Intermediate sized 30 × 30cm² Modules will be produced by the PVcomB

Bridging the gap between science and industry

Germany has gained a leading position in the photovoltaics (PV) market. To stay ahead, it is crucial to increase the technological effort in the rapidly expanding field of thin-film PV as well. Here, swift transfer from lab developments into cost effective production is a key factor. PVcomB's main goal is to support world wide growth of thin-film photovoltaic technologies and -products by providing the much needed technology transfer.

There exists a large gap between production of lab-sized photovoltaic cells and industrial-size modules. PVcomB bridges this gap by operating two dedicated pilot-lines for intermediate size PV modules with an area of 30 × 30 cm². This intermediate module size is well suited to address questions arising in industrial production. At the same time, alternatives will be developed and tested for each process and analytical step. The great variety of analytical tools available ensures that changes in the product-performance can be linked to fundamental material or process properties. A truly unique feature of PVcomB´s pilot-lines is that both thin-film silicon as well as CIS based modules will be studied within a single laboratory. This convenient arrangement offers the potential to unlock significant synergies in many topics common to all thin-film based technologies. Additionally, education and training will provide the industry with highly skilled thin-film PV professionals. The close involvement with universities and private education centers will allow highly-qualified engineers and scientists to be trained at the same time. These engineers and scientists are desperately needed in the booming solar industry.

The new logo of the PVcomB

New laboratory for new cluster-tool

The old clustertool: dismantling in the old laboratory…

To produce larger (test-)modules, larger machinery is needed. In March 2008, the department SE3 Technology opened up its new laboratory. Here, the new Cluster-Tool II was installed so that the scientists can now cover areas of 10x10 cm^2. The new clustertool gives more possibilities regarding deposition speed and area as well as more possible combinations of materials. In the two additional chambers, spuutering and physical vapour deposition (PVD)for new materials is now possible. One Example of these new materials is kesterite, in which the indium is replaced by zinc and tin.

Through the move in the new and larger laboratory, a larger and better equipped infrastructure is now available for developing thin-film solar cells.

… and with new components: the clustertool II shining in its new location.

The golden anniversary of neutron research in Berlin

When change is in the air it is a good opportunity to take stock, looking back on what has been achieved in the past. As luck would have it, the 50th anniversary of the beginnings of neutron research in Berlin coincided with preparations for the merger of the Hahn-Meitner-Institute and the Berlin Synchrotron Radiation Source BESSY.

Neutron scientists from other centres, users and retired employees joined in the celebrations with the staff of what in June became known as the Helmholtz-Zentrum Berlin für Materialien und Energie (HZB). They spent two days enjoying a varied programme of talks on neutron science in Berlin and elsewhere – past, present and future.

But before turning to hard science, it was time for pure celebration: seven representatives of other neutron sources and scientific organisations delivered birthday greetings on behalf of their institutions, and Hans-Gerhard Husung, Berlin's Permanent Secretary for Education, Science and Research, was the bearer of both the compliments of the local government and a promise of continued support in the future.

It fell to Jost Lemmerich to describe the early days of neutron science in Berlin. The idea of building a research reactor in Berlin was first put forward in 1955 in a declaration by professors at the local universities who wanted Germany to catch up on nuclear research – the field of science considered most important and promising at that time. Despite the difficulties connected with the special legal status of Berlin and the fact that West Berlin was an enclave within East Germany, Berlin's first research reactor – a 50 Kilowatt homogeneous reactor – went into operation in July 1958 and was used almost exclusively for irradiation experiments in nuclear chemistry.

BER I under construction

Alexander Belushkin (left) congratulates Michael Steiner on behalf of the Frank Laboratory of Neutron Physics (Dubna)

Shortly after the institute's second reactor BER II became operational in 1973, Hans Dachs introduced neutron scattering as a further method of investigation that was soon to become the primary way of using neutrons at HMI. The general development of neutron scattering was the topic of Andrew Taylor's introductory talk on *Expanding the Frontiers of Neutron Scattering*, while Michael Steiner and Ferenc Mezei told the story of neutron scattering in Berlin. Steiner outlined HMI's contribution to the development of neutron science over the last few decades and emphasized that HMI is a good example of how an institute with only a medium-flux reactor can rank among the best by investing in excellent instrumentation, e.g. the institute's

Lively discussions during the programme celebrating the golden anniversary of neutron research in Berlin

extreme sample environment equipment that attracts a considerable number of neutron users to Berlin.

A series of presentations called “Current trends in neutron science” followed. They offered a broad overview of developments in technology for neutron research – new sources and sample environments – and the use of neutrons in different fields of science: magnetism, soft matter, engineering materials and art history. Having taken a look at the past and the present, Alan Tennant’s talk concentrated on the future of neutron science at HZB with the new high field magnet providing magnetic fields of 25 or even 30 Tesla for neutron experiments being the most important current project. Developing instruments that will meet the demands of users working in the fields of soft matter and quantum magnetism are further priorities.

In his final statement, Michael Steiner stressed that only the use of different complementary methods will allow us to solve the questions posed by modern science. He recalled that Hans Dachs had had the vision of applying various complementary methods at HMI and that he had already entrusted a young scientist with exploring X-ray scattering as a complementary method to neutron research. With the merger of the former Hahn-Meitner-Institute and BESSY, Dachs’ vision of operating sources of neutrons and synchrotron radiation within one institute will now become reality.

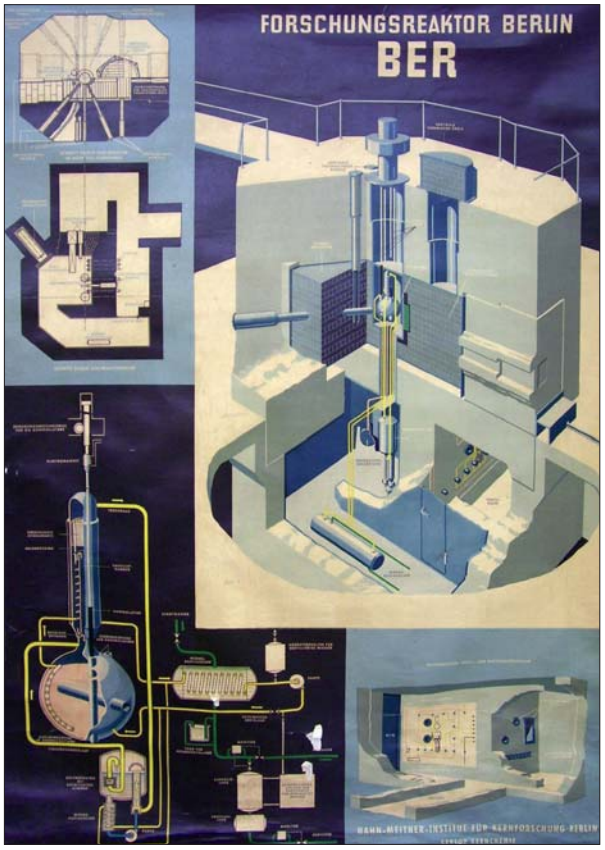

Poster showing the layout of HMI’s first research reactor BER I

Photovoltaics abroad

To promote the excellent science in photovoltaics, the scientists offered or supported many international workshops in 2007/2008. One of them took part in Africa, Nairobi: The summer school Cost-effective Photovoltaics Research was held from 19th August to 1st September 2007 at Jomo Kenyatta University of Agriculture and Technology in Nairobi, Kenya. It trained thirty young scientists from eight East African countries in both theoretical and experimental aspects of cost-effective photovoltaics. The summer school was prepared during the preceding two years by Dr. Dittrich, together with Prof. Lux-Steiner, from Hahn-Meitner Institute in Berlin and partners, it is funded amongst others by the Volkswagen Foundation.

At another far-away location in Thailand, the Photovoltaic workshop at Kasetsart University (Bangkok, Thailand) took place from 1st to 12th of August 2008. Here, students attended lectures and practical sessions to familiarize themselves with the basics in photovoltaics. The Workshop was organized by Dr. Dittrich (SE2). The workshop is planned to be repeated in 2009 as part of a new masters course.

Particpiants of the summer school Cost-effective Photovoltaics Research at the reception

Participants of the Photovoltaic workshop

Imaging in three Dimensions – Information day at the HMI

A detailed three-dimensional view of the inside of a material or of a device offers incalculable value for the industrial development. The HMI offers a wide range of imaging procedures, which can be used by industrial partners in different cooperation models. Some of these methods are only available at few places worldwide, one of them the HMI. To show the whole range of technical and cooperation possibilities, the HMI invited for a free information-day, or 'Industrietag' (industry day), on November 11th, 2007. The wide range of visitors showed a lively interest in the talks and the guided tours to the laboratories. Representatives from companies as well as research institutions presented examples from their work at the HMI. At the poster session, the visitors could talk directly to a scientist representing one imaging method.

Meeting the scientists during the postersession

Explanations at the model of the new high-field magnet to be built at the HZB

Solar exhibition and conference PVSEC

In both years, 2007 and 2008, the HMI took part in the exhibition of the PVSEC – European Photovoltaic Solar Energy Conference and Exhibition.
In Milano 2007 (Italy), three former graduate students of the HMI were awarded the "SolarWorld Einstein New Talent Award". The junior scientists focused their theses on the specific influence of grain boundaries on the electrical properties of chalcopyrite layers. In both years, the HMI shared a stand with sulfurcell, a spin-off of the HMI. The visitors could thus ask questions regarding the production as well as the research of thin-film photovoltaics.

Visitors admiring the flexible solar cell at the HMI-stand (Valencia, 2008)

Frank H. Asbeck (CEO Solar World), Tobias Eisenbarth, Caspar Leendertz and Mark Wimmer (left to right) at the award ceremony of the the "SolarWorld Einstein New Talent Award" (Milano, 2007)

School on Neutron Scattering

The HMI School on Neutron Scattering (NSSc) is part of the curriculum of the Faculty of Mathematics and Sciences of the Technical University Berlin and is sponsored by the European Union under its NMI3 Program. Professors Alan Tennant and Prof. Bella Lake were responsible for the schools in 2007 and 2008, several scientists of HMI contributed by tutoring the hands-on experimental work at the neutron scattering instruments at BENSC and by lectures.

The schools in 2007 and 2008 were held at the Berlin Neutron Scattering Center (BENSC) of the Hahn-Meitner-Institute (HMI) Berlin. About 30 students took part from 26th February to 2nd March 2007 and from 3rd to 7th March 2008 in the 28th and 29th school respectively.

The NSSc follows a given curriculum, starting with a theoretical introduction to methods of neutron scattering which comprises the basic principles of neutron scattering, an introduction to neutron sources, the different types of neutron instrument and sample environment.

However, the main emphasis lies on hands-on experience of the neutron scattering techniques at BENSC, including triple-axis spectroscopy, powder diffraction, small angle neutron scattering, reflectometry, time of flight spectroscopy, and tomography. The students are divided into streamed groups of 4 or 5 people and spend three hours on each instrument over a period of three days doing experiments.

Nikolay Kardjilov (HZB) shows the students a 250 million years old reptile skull at the CONRAD tomography station

Technology Transfer Prize goes to fuel cell researcher

In 2007, HZB's Technology Transfer Prize was awarded to Dr. Peter Bogdanoff of the institute's Solar Energy Division for his work on innovative catalysts for fuel cells.
The winner and his team were successful in making efficient catalysts for oxygen reduction in fuel cells without using the expensive element platinum. These results convinced the Toyota Motor Cooperation to invest in several collaborations with HZB.
The winners were selected by a jury composed of representatives of industrial companies, the Chamber of Commerce and Industry and the Technology Foundation Berlin. The main criteria for selection were the project's innovative potential and the prospects for using the new process on an industrial scale.
The prize was conferred on Peter Bogdanoff at an award ceremony in HZB's lecture hall by Dr. Florian Holzapfel, CTO of Q-Cells AG, which also donated the prize money of 5,000 EUR. In his welcome address, Prof. Michael Steiner emphasized the increasing importance of the transfer of knowledge between scientific institutions and industrial companies and the institute's commitment to supporting the industrial exploitation of results achieved by HZB's scientists. At the end of the ceremony, Peter Bogdanoff showcased prize winning technology and its potential for commercial applications.

Dr. Bogdanoff receives the Technology Transfer Price

AARD 2007: Franco-German Summer School on "Analysis in Art with Radiation"

Following the summer schools on ion tracks in Mühlhausen, 2003, and on "Physics with Ions - from Analysis to Nanotechnology" in Blainville-sur-Mer, Normandy, 2005, a German-French summer school was held on "Analysis in Art with Radiation" (AARD) in Mühlhausen, Thüringen, September 2007. This transdisciplinary subject intended to bring together natural science, its analytical methods, and questions related with cultural heritage. The school was chaired by Heinz-Eberhard Mahnke (HMI and FU Berlin) and Michel Menu (C2RMF), with the support of Oliver Hahn (BAM). It received financial support from the DFH-UFA (Saarbrücken), with additional support from the organizing institutes.

In both France and Germany, but elsewhere too, some user-time at large-scale facilities (e.g. neutron and photon sources, ion beam accelerators) is devoted to cultural heritage objects to complement investigations using "table top" methods. Participants learned how to use tomographic methods to look into papyrus rolls without unrolling them, why certain precious scripts, like the Qumran Scrolls, deteriorate, or, where the 'cracks' arise from in Leonardo da Vinci's Mona Lisa. A specialty of the school was practical courses on analytical computer programme packages (quantitative analysis of particle induced X-ray emission, X-ray fluorescence analysis (XFA) and ion beam analysis), and, as highlight, the course on a portable XFA system used for on-site investigations (e.g. paintings in churches).

Out of the regional richness in culture, the participants took home impressions from the Wartburg (a special exhibit connected to Saint Elisabeth), music by J. S. Bach (Eisenach, Mühlhausen Divi Blasii), and the intriguing story of the "Sky Disk of Nebra", recently discovered nearby.

The next German-French summer school is scheduled for September 2009 on "Nanophotonics in Nature and Art", from fundamentals of structural colouration to applications in biomimetics.

Heinz-Eberhard Mahnke, mahnke@helmholtz-berlin.de

Meetings, Conferences organized by HMI

Event	Organized together with	Location	Dates
Analysis in Art with Radiation AARD 07	UFA-DFH Université Franco-Allemande BAM Berlin	Hahn-Meitner-Institut Berlin	3rd to 9th September, 2007
PNAM Autumn School about Application of Neutrons and Synchrotron Radiation in Engineering Materials Science	TU Berlin	Haus am Schüberg, near Hamburg	17th to 21st September, 2007
NIAC Meeting 2007		Hahn-Meitner-Institut Berlin	24th to 26th September, 2007
Orbital 2007	University of Hamburg, Max-Planck-Institute for Solid State Research in Stuttgart	Max-Planck-Institut in Stuttgart, Germany	10th to 11th October, 2007
Workshop on Tomography in Materials Science using TEM and FIB		Hahn-Meitner-Institut	11th to 12th October, 2007
Dreidimensionale Einblicke in Werkstoffe und Geräte		Hahn-Meitner-Institut Berlin	16th November, 2007
29th Berlin School on Neutron Scattering	Technische Universität Berlin	Hahn-Meitner-Institut Berlin	3rd to 7th March, 2008
European Summer School on Photovoltaics and New Concepts of Quantum Solar Energy Conversion	European Society for Quantum Solar Energy Conversion (QUANTSOL)	Hirschegg, Austria	14th to 21st September, 2008
ICTMC-16 16th International Conference on Ternary and Multinary Compounds	Freie Universität Berlin	TU Berlin	15th to 19th September, 2008
European Cyclotron Progress Meeting – ECPM XXXVI	Charité Berlin	Hahn-Meitner-Institut Berlin	15th to 18th October, 2008
European Conference on Metallobiolomics	Helmholtz-Zentrum München, Deutsches Forschungszentrum für Gesundheit und Umwelt	Hahn-Meitner-Institut Berlin	3rd to 4th December 2008

High Field Magnet Project – Progress in Design and Construction

Hartmut Ehmler, Peter Smeibidl and Alan Tennant

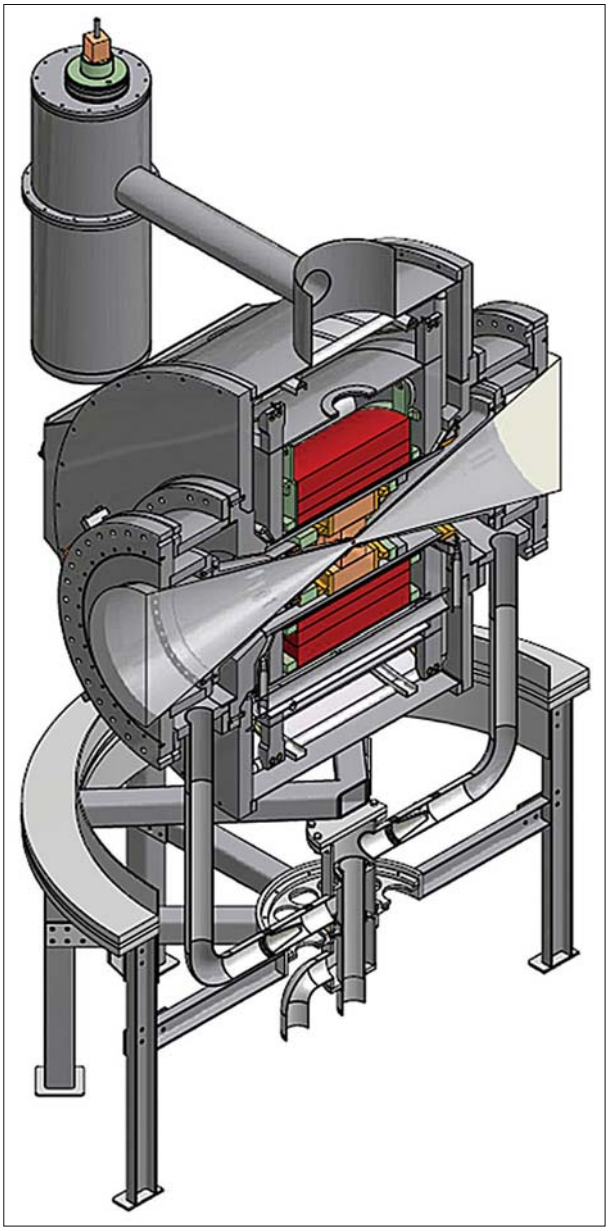

Fig. 1: Cross sectional view of the hybrid magnet system: The superconducting coil is shown in red. At its centre is the water cooled copper magnet. Cooling water is channelled to the resistive magnet through the pipes below the centre of the magnet. The small satellite cryostat (top left) contains the 20 Kiloampere current leads made from high temperature superconducting material.

A new research magnet for neutron scattering experiments under extreme fields is presently under construction at the Lise-Meitner Campus of the Helmholtz-Zentrum Berlin. The system will produce magnetic fields stronger than 30 Tesla in its final stage. Scientists expect that neutron scattering experiments in the new magnet will contribute to important insights in many fields of condensed matter research. Condensed matter systems with magnetic degrees of freedom cover the whole range from fundamental to applied science. The basic elementary excitations in certain types of chain materials ("spinons") allow us to observe the equivalent of quarks, i.e. one of the basic constituents of matter. Correlated electrons in certain layered compounds offer the chance to tailor high temperature superconductors, i.e. materials with an enormous potential for industrial applications. What these topics have in common is that their behaviour is dominated by the laws of quantum mechanics, and both neutrons and high magnetic fields are required in order to understand their microscopic behaviour, for fundamental physics as well as for material science.

A research contract with the National High Magnetic Field Laboratory (NHMFL) in Tallahassee, Florida was signed in March 2007. This world-leading laboratory in magnet science and technology has developed the concept of a “series-connected hybrid magnet” (SCH). The magnetic field will be produced by two coaxial coils connected in series: the large outer coil is a superconducting "cable-in-conduit" system and the smaller inner coil is made from copper. The reason for using a resistive inner coil is that, at present, no superconducting material is available that could carry high currents in these strong magnetic fields without degrading under the enormous acting forces. The design activities by NHMFL are focused on the detailed layout of the superconducting winding and the integration of all helium cooled components inside a cryostat. The superconducting cable underwent an extensive test programme which was successfully completed in autumn 2008. The cable is a novelty in itself and will carry more than twice as much current density as state-of-the-art superconducting cables. The detailed design of the coil winding includes calculations of the high mechanical stresses due to the magnetic forces. These forces cause strains within the conductor which have a negative impact on the superconducting properties. Therefore, tensile tests of full-size conductors under full current in a dedicated test facility at NHMFL were also necessary another world novelty in this field.

Fig. 2: Beside the neutron guide hall 2 (light blue) the new building for the magnet infrastructure has been under construction since summer 2008.

The magnet will need several supply media for operation: large quantities of high pressure water at 30 bar to cool the resistive copper coil, supercritical helium of 4 Kelvin to cool the superconducting circuit and, last but not least, an electrical current of 20,000 Ampere to provide the magnetic field. All the supply facilities are to be hosted in a separate infrastructure building which is currently being erected on site at the Lise-Meitner Campus, near the neutron guide hall 2 (NLH-2), where the neutron instrument ExED and the magnet will be installed. On three floors inside of the building all necessary technical components will be constructed. The cooling towers of the water cooling system will be located behind a sound insulating wall on top of the building.

The challenge for the small project control team is to organise and monitor the various activities in magnet design and construction of the infrastructure components. Project control has to manage the various subprojects and work packages with all important interfaces as efficiently as possible. For example: all project documents are stored in a central database with a work flow of check and release. Several external companies and collaboration partners are working together to maintain a tight schedule to achieve the aim of final commissioning of the magnet within the next three to four years.

Fig. 3: Location of the new High Field Magnet

Sample environment service beyond neutron and X-ray scattering

Klaus Kiefer, Dirk Wallacher, Michael Meißner - Helmholtz-Zentrum Berlin für Materialien und Energie

Fig. 1: The recently installed 17T System for LaMMB CM-17T.

BENSC is part of HZB's user facility for structural research with neutrons and synchrotron radiation and focuses on experiments under extreme sample conditions, i.e. involving the highest magnetic fields, the lowest temperatures and a wide range of pressures. Therefore, a broad range of mobile equipment, such as superconducting magnets, cryostats, furnaces, vacuum pumps and pressures cells, is available and is constantly being developed to adapt to the requirements of the sample environment for scattering experiments. Furthermore, in the last decade, there has been growing demand in the neutron and x-ray user community for new experimental set-ups and methods, both at the beamline and in the laboratory, to complement the scattering investigations by additional measurements. The BENSC sample environment group has reacted to this situation by initiating two major new projects that are being presented in this article. The first is the **La**boratory for **M**agnetic **M**easurements at **B**ENSC (**LaMMB**) which provides users with access to complementary bulk measurements using high level laboratory techniques. The second is a **D**edicated sample **E**nvironment which responds to the users' request for in-situ **G**as **A**dsorption experiments with neutron and X-ray **S**cattering (**DEGAS**). Both projects are presently under development. First results are very promising and the BENSC user community is already profiting from these facilities.

Laboratory for Magnetic Measurements at BENSC (LaMMB)

With its special emphasis on experiments involving high magnetic fields and low temperatures, BENSC is offering extreme physical conditions for structural research. Beamline based investigations, however, usually require complementary measurements. In recent years, the departments for structural research, SF-1 and SF-2, have operated a variety of research laboratories for sample characterisation and preparation. In order to install a service for BENSC users providing access to complementary measurements

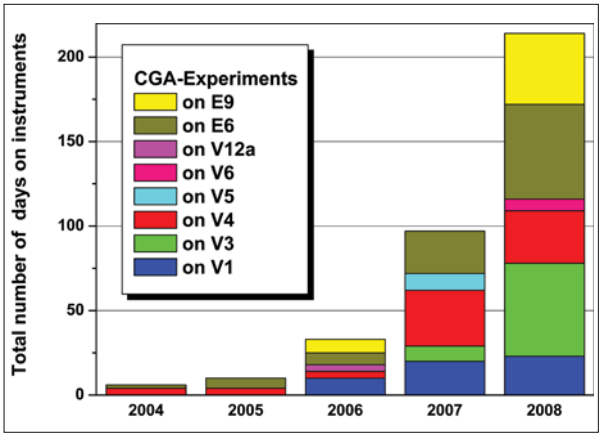

Fig. 2: Statistics showing the development of gas adsorption experiments at BENSC.

at extreme conditions, these laboratories have been combined to form LaMMB. At present, LaMMB offers four different measurement systems with magnetic fields up to 14.5 Tesla (T) and temperatures down to 260 mK. The measurement options are heat capacity, heat conduction, magneto-caloric effect, magnetization, magnetic susceptibility, AC/DC resistivity, and dielectric properties. With more than 100 measurement projects per year in 2007 and 2008, LaMMB has become a regular and important user service (Rüegg et al.).
In 2009, LaMMB will extend its range of experiments, aiming for lower temperatures and higher magnetic fields. Figure 1 shows the new cryogenic system CM-17T with magnetic fields up to 17 T and temperatures down to 8 mK which was installed at the end of 2008. First test measurements with this system have already been performed. The CM-17T's first magnetic measurement when it goes into operation will be low temperature magnetisation based on a cantilever magnetometer. For this purpose the CM-17T is equipped with a 17T primary superconducting magnet and a gradient coil. In addition to the primary 17T magnet, an 8T secondary magnet is located below the primary magnet. This is preparing the next stage of LaMMB's development towards sub-millikelvin temperatures with the help of a demagnetisation stage.

Controlled Gas Adsorption (DEGAS)
In the past, most of the neutron and x-ray scattering experiments have been carried out on samples which change their properties due to externally applied fields of an electro-magnetic nature, temperature or mechanical pressure, but which do not change with respect to their chemical composition. Only a small but fast-growing number of hard and soft matter investigations (Figure 2) deals with samples that are modified in-situ in the beam by simply adding or removing particles using gas ad- or desorption. Reasons for the growing interest in this type of experiment are manifold. In-situ gas adsorption studies in the context of structural research on materials for energy storage are certainly one of the main reasons (A. Remhof et al., p. 42), but also the detection of property changes in a soft or bio-material due, for example, to variations in the moisture of the sample opens up a wide field of applications. The controlled filling and emptying of voids in new nanostructured materials offers the option to change the contrast in a scattering experiment so that complex structures can be visualised (B. Smarsly et al., p. 38). In-situ synthesis and catalysis under extreme pressure and temperature conditions can also be easily investigated with neutrons, for instance to understand chemical processes while forming new materials (M. Russina et al., p. 54).

It is still proving a great challenge to create all the unique experimental conditions with regard to gas pressure and temperature in combination with the powerful neutron and synchrotron scattering methods. At BENSC we have started to develop several new sample environments for controlled gas adsorption (CGA) in which pressure, volume and temperature of a gas in neutron suited sample cells can be handled remotely (and with high precision) by the user via automated gas handling systems. Pressures from 10^{-5} bar to 300 bar and temperatures ranging from 1.5 K to 1300 K can be achieved by modular designed gas dosing systems and temperature controlling devices. For ultra high pressure experiments with hydrogen up to 10.000 bar, a unique gas supply system has been developed at BENSC

Fig. 3: Unique fully automated 10 kbar hydrogen gas-handling system for highest controlled gas pressures in combination with neutron investigations.

(Figure 3), while for controlled humidity and continuous gas flow experiments a sophisticated gravimetric system (based on a magnetic suspension balance) has been purchased for in-situ sample weighing during gas exposure up to 500 bars in a wide temperature range.
Since most of the "beamline" equipment provides unique opportunities to combine pressure and temperature it can also be utilised by internal and external users in the laboratory for approving new methods, characterising samples or preparing scattering experiments. For BESSY the first in-situ experiments in an x-ray setup is planned for 2009 to respond to the frequent user request in the last year.

New instruments for ANTOME

In April 2006, the Application Centre for Tomographic Methods in Materials Science (ANTOME) became the proud possessor of a ZEISS Cross-Beam 1540 EsB focussed ion beam system (FIB). This electron microscope, which was financed jointly by the European Union and the City State of Berlin, has been installed in the Microstructure Group in Department SF3.

The FIB combines an imaging column using field emission (SEM) technology and a high performance focussed ion beam column. It is mainly used in a wide area of materials for tomography by serial sectioning. It also comprises various detectors and analytical devices, such as an inlens detector, a high resolution electron backscattering detector, a secondary electron detector and detectors for energy dispersive X-ray analysis and for scanning transmission electron microscopy. The variety of detectors means the microscope can be utilised in a large number of research fields. And it is not just intended for internal use either: the many users of the Helmholtz-Zentrum Berlin für Materialien und Energie (HZB) and Technische Universität Berlin (TU Berlin) are also able to profit from the FIB.

Prof. Schubert's group at TU Berlin investigates biocompatible ceramic foam materials; Prof. Boit's group, also at TU Berlin, is interested in the failure diagnostics of integrated circuits. Materials for solar cells (layers preparation, microstructure analysis) are the focus of study in Prof. Schock's group (SE3, HZB). High precision transmission electron microscopy sample preparation and sharp tip preparation for atom probe tomography of metallic materials are performed by Prof. Banhart's group (SF3) while Prof. S. Eisebitt's group from BESSY is concerned with the preparation of specimens for lithography.

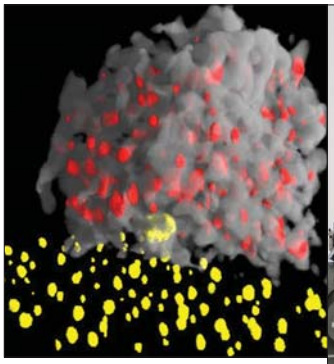

Fig. 2: Visualization of a 3D data set reconstructed from a tilt series of TEM images showing catalyst particles (red) on carbon black (gray). The carbon black particles are supported on a carbon foil with small gold particles (yellow) which have a typical diameter of about 5 nm.

Fig. 1 Construction of the Zeiss LIBRA transmission electron microscope

Fig. 3: Participants in HZB's tomography workshop in October 2007

Spring 2007 saw the arrival at HZB of the Zeiss Libra 200 transmission electron microscope (TEM) which passed the final acceptance tests later in the summer (Fig. 1). The installation of the new TEM completed the array of instruments at ANTOME which now offers the complete range of 3D-characterization methods from the nanometre scale up to specimen sizes of several decimetres. Moreover, it complements other methods employed at HZB, such as small angle scattering. Due to its modular design the microscope is one of the most versatile machines at HZB, making it possible to employ several imaging techniques, electron diffraction, electron energy loss and X-ray spectroscopy at a given specimen site with a lateral resolution in the nanometre range.

Current fields of investigation include technical and amorphous Al-alloys, thin film solar cells and magnetosoms in bacteria (in cooperation with MPI in Golm). One of the main methods employed is electron tomography (ET). For example, the size distribution and deposition characteristics of Se-modified Ru-catalysts on carbon black are investigated in three dimensions in cooperation with scientists in Department SE 5 at HZB. Fig. 2 shows an example of a three dimensional data set reconstructed from a tilt series of TEM images showing the catalyst particles (red) on carbon black (gray). The carbon black particles are supported on a carbon foil with small gold particles (yellow). Such images already allow qualitative discrimination of the catalyst locations with respect to the carbon black support, which is important for understanding the differences in the catalytic activity of the material.

To mark the completion of ANTOME the project partners organised a very successful two-day Workshop on Tomography in Materials Science using TEM and FIB in October 2007 (Fig. 3). Plans are currently being discussed for a similar workshop in the near future. The number of joint research projects with other groups at HZB and different research institutions, e.g. TU Berlin and Freie Universität Berlin, is steadily increasing.

The ANTOME project time line officially ended in July 2008. However, ANTOME's scientific work is continuing and branching out into other fields of activity, especially electron tomography.

N. Wanderka, M. Wollgarten

X-ray micro-imaging using different contrast modes and partially coherent synchrotron light

S. Zabler[1], A. Rack[2], I. Manke[1,3], H. Riesemeier[4], B. R. Müller[4], J. Goebbels[4], N. Kardjilov[3], M. Dawson[3], A. Hilger[3], J. Banhart[1,3]

■ 1 Helmholtz-Zentrum Berlin ■ 2 European Synchrotron Radiation Facility, ■ 3 Technische Universität Berlin ■ 4 Bundesanstalt für Materialforschung und -prüfung

Synchrotron-based micro-imaging is a valuable tool in materials research, life science, non-destructive evaluation, and palaeontology. The high brilliance at synchrotron light sources can be used to record images with an extremely low noise level and high spatial resolution within short acquisition times. Additionally, monochromatic radiation can be used to reduce artefacts while increasing the material contrast. The spatial coherence of the light source gives access to improved interfaces- and/or material-contrast by adding interferometric techniques to the available imaging modes. Novel contrast mechanisms which were applied to micro-tomography (μCT) are: X-ray fluorescence tomography (sensitive to the local chemical species distribution), refraction enhanced tomography (sensitive to inner surfaces and interfaces), diffraction tomography (contrasting the local texture of polycrystalline material grains) and holotomography (imaging the real decrement of the materials' refractive index) [1-3].

Over the past few years, the Helmholtz-Zentrum Berlin für Materialien und Energie (HZB), together with the Bundesanstalt für Materialforschung und –prüfung (BAM), has developed a micro-imaging station at Berliner Elektronenspeicherring-Gesellschaft für Synchrotronstrahlung (BESSY). Absorption contrast, refraction enhanced imaging as well as inline phase contrast μCT are the standard imaging modes [2]. The available contrast mechanisms were recently extended to holotomography [3].

The principle of holotomography is illustrated in Figure 1. Tomographic datasets are recorded at different sample-detector distances. Here, the phase contrast imaging mode yields to the formation of high-contrast interference fringes at materials interfaces and micrometre-sized inhomogeneities. This effect gains in strength the more the images are defocused, i.e. for larger sample-detector distances. Whilst the inline phase contrast mode is often used directly for imaging, numerical phase retrieval can be applied to one or several such images, yielding a projection map of the real decrement of the materials' refractive index (absorption images represent the imaginary part, usually 2-3 orders of magnitude smaller than the real decrement which is approximately the local electron density). These so-called phase-maps are used for reconstructing volume images. Figure 2 illustrates the differences between (a) absorption,

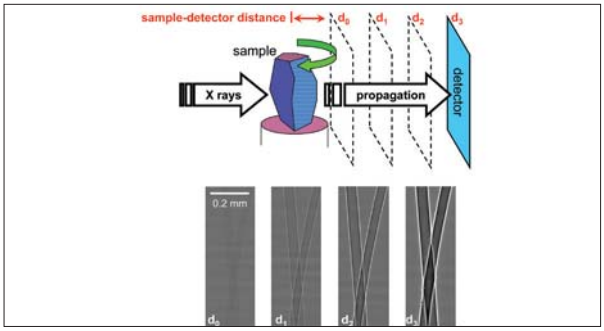

Fig. 1 Fresnel-propagated X-ray imaging illustrated for radiographs of two hairs recorded with increasing sample-detector distance [2,4].

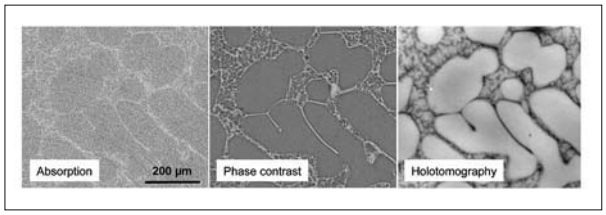

Fig. 2: Slices taken from three different tomograms of an AZ91 alloy: a) absorption contrast tomography, b) phase contrast tomography and c) holotomography [2].

(b) inline phase contrast and (c) holotomography for a tomographical slice showing the microstructure of a metallic specimen made from AZ91 alloy (Mg-particles in Mg-Al matrix). Holotomography features a highly improved density contrast which is important for imaging specimens of weak absorption (biological samples) and specimens with two or more material phases of similar density.

[1] J. Banhart (ed.), Oxford University Press (2008).
[2] A. King et al., Science 321, 382 – 385 (2008).
[3] C. G. Schroer et al., Appl. Phys. Lett. 79, 1912 (2001)
[4] A. Rack et al., Nucl. Inst. Meth.A,, 586, 327-344 (2008).
[5] P. Cloetens et al., Appl. Phys. Lett. 75, 2912-4 (1999).
[6] S. Zabler, PhD thesis, "X-ray imaging by partially coherent synchrotron light, applied to metallic alloys, tooth dentin and natural rock" (2007).

A decade of precision: proton therapy at HMI and Charité

A. Denker[1], C. Rethfeldt[1], J. Röhrich[1], D. Cordini[2], R. Stark[2], A. Weber[2], L. Moser[2], M.H. Foerster[2]
■ 1 Helmholtz-Zentrum Berlin für Materialien und Energie GmbH ■ 2 Charité

The use of protons in radiotherapy has obvious advantages compared to other clinically available irradiation techniques. Protons exhibit “inverse” depth dose distribution, i.e. the dose applied to the irradiated tissue increases with depth and vanishes after a steep maximum, the so-called Bragg peak (Fig. 1). The position of the Bragg peak can be adjusted precisely by varying the proton energy. In addition, the lateral scattering area of proton beams is much smaller than the penumbra of conventional X-ray or electron beams. Thus the irradiation dose applied with protons can be concentrated on the tumour, causing less collateral damage to healthy tissue and sensitive organs such as – in the case of the eye – the macula or the optic disc.

From 1998 onwards, eye tumours were treated with 68 MeV protons in the ion beam laboratory ISL at Hahn-Meitner-Institut in collaboration with the University Hospital Benjamin Franklin, now known as Charité - Campus Benjamin Franklin. ISL, providing light and heavy ion beams for research and applications in solid state physics and medicine, was closed down at the end of 2006. In order to ensure the continuation of the eye tumour therapy in Berlin - the only proton therapy facility in Germany to this day - a cooperation agreement was signed between Charité and HMI in December 2006. Accelerator operation continued with reduced manpower, which required changes in the set-up of the accelerators. Thus in spring 2007, a 2 MV tandetron was acquired from the Bundesanstalt für Materialforschung und -prüfung to replace the Van-de-Graaff-injector. The tandetron was dismantled, packed up, moved, and installed at its new location in the cyclotron vault. The first beam from the ion sources of the tandetron was obtained in September 2008.

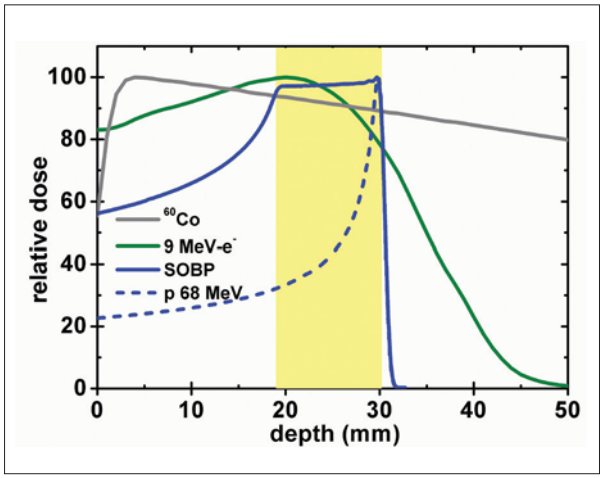

Fig. 1: Depth dose distribution of electron beams (dark green line) and X-rays (grey line), both used for conventional radiotherapy, in comparison with the depth dose distribution of a mono-energetic proton beam (dashed blue line). No dose is applied after the steep maximum, the so-called Bragg peak. By overlapping various proton energies it is possible to cover the target depth (yellow) with a homogenous dose (blue line).

A crucial point for proton therapy is reliability. In 2007, the accelerators were available for 92% of therapy time: Due to a fault in the cyclotron, one of the eleven therapy weeks in 2007 started one day late. During the twelve weeks scheduled for therapy in 2008, an up-time of more than 95% was achieved.

Tumour irradiation is performed during the radiotherapy week on four consecutive days, the first day of the week being used for quality control. Typical irradiation times for dose application are about 30 seconds to 1 minute for each fraction, while patient preparation and positioning take about 15 minutes to half an hour. Tumour control rates are above 96% [1]. In most cases, the patient’s visual acuity can be maintained to a satisfactory degree.

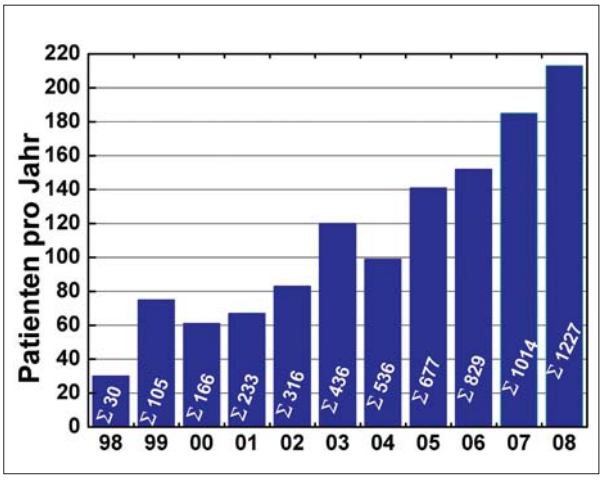

Fig. 2: Number of patients per year (blue bars) and the integral number of patients treated (white numbers).

**"If you can't see it, you can't hit it,
and if you can't hit it, you can't cure it."**

Harold Johns

Proton therapy of eye tumours requires positioning in the sub-millimetre range. For this purpose, small tantalum clips sutured to the eye globe serve as landmarks. While the patient is immobilised in the treatment chair, looking at a fixation light, clip and eye positions are determined with a digital X-ray system providing orthogonal images. The clip projections from the treatment plan are superimposed on the immediate X-ray images for position control. By correcting the coordinates of the chair and fixation light the patient is repositioned until both actual and target clip projections fit together perfectly.
In order to avoid a time-consuming trial-and-error approach to correction, the image processing software was further developed to compare both projections with each other by automatically detecting the clip positions from the X-ray pictures and calculating the necessary corrections of chair and light coordinates. This novel use of the positioning software facilitates the adjustment to the final treatment position. Perpendicular X-ray views allow precise patient positioning at a degree of accuracy below 0.3 mm. The installation of an on-site digital X-ray system for patient positioning is unique in proton therapy. The automated procedure reduces mean positioning time which makes therapy more tolerable for the patient and results in higher patient throughput.
The number of patients has continuously increased (Fig. 2). In 2007, 185 patients were treated in 11 therapy weeks and, in December, we were able to welcome the 1000th patient with a bunch of flowers (Fig. 3). The average number of patients treated per week continued to rise in 2008, with 18 patients being treated every weekday.

A particular challenge in 2007 was the treatment of a patient with Ankylosing spondylitis who had a spinal curvature of about 60°. A custom made tiltable seat with extra footrests and remote adaptation of the mask holder to position the patient in the isocentre had to be built, requiring four simulation sessions at intervals of more than a week.

Fig. 3: December 2007: The 1000th patient is welcomed with a bunch of flowers

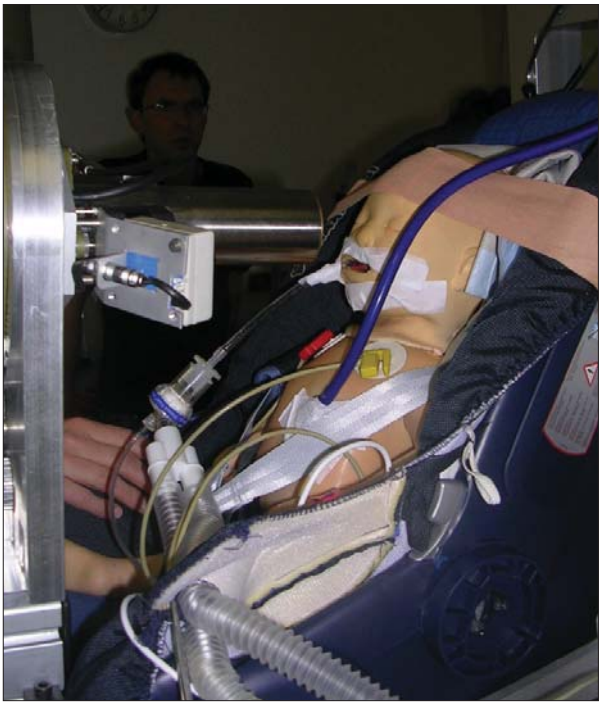

Fig. 4: Summer 2007: The sequence of treatment under anaesthesia being tested using a dummy baby

In 2008, the case of an infant posed even greater challenges, as the treatment of babies has to be performed under general anaesthesia. Prior to the treatment itself, preparation sessions using a dummy (Fig. 4) were held to test all the equipment and the sequence of events precisely.

Since the beginning of the therapy in 1998, more than 1,200 patients have been treated. The accelerator has operated smoothly and reliably. Greater precision has been achieved by improved beam delivery, better planning procedures, and enhanced treatment methods in close, multi-disciplinary cooperation between physicists, radiation therapists, and oncologists. And we will continue to provide unique therapeutic possibilities for patients in Germany.

[1] C. Mans, S. Hanning, C. Simons, A. Wegner, A. Janssen, M. Kreyenschmidt, *Development of suitable plastic standards for XRF*, Spec trochimica Acta, Part B: Atomic Spectroscopy 62B (2007) 116-122.

Corresponding author:
A. Denker
denker@helmholtz-berlin.de

BENSC User Operation

BENSC in Short

Berlin Neutron Scattering Centre (BENSC) is the administrative unit within Helmholtz-Zentrum Berlin (HZB) responsible for the instrumentation and user operation at the medium-flux research reactor BER-II. BENSC operates more than 20 instruments and has established itself as a major research facility for neutron science on an international scale with exceptionally high demand from European users. BENSC offers access to a great variety of neutron scattering and radiography instruments with some unique features suitable for research in many fields of science. At present, 14 instruments are in routine operation for external users. These instruments cover practically all neutron scattering and radiographic techniques, with the exception of backscattering. Several of them provide neutron intensities and resolutions which can compete with the best instruments available worldwide.

The major scientific fields actively pursued at BENSC are research on magnetism, soft-matter and biological materials, as well as on nano-sized and engineering materials. A unique and internationally recognised strength of BENSC is the large range of sample environment equipment available to carry out experiments under extreme conditions. Highest magnetic fields (up to 17.5 T) and lowest temperatures (down to 30 mK) are routinely offered to users together with extensive expert support by in-house scientists and technical staff. A further focus in sample environment is now available (specialised equipment for neutron scattering experiments under controlled gas atmosphere), to serve a rapidly growing user community in the fields of soft matter, biology and materials science

Personnel

An important change occurred in 2007. Professor Ference Mezei, director of BENSC for many years, retired from HZB and Professor Alan Tennant, head of the department of magnetism, was appointed BENSC director.

User Operation

At the 14 user instruments, 70% of the beam time is reserved for external users (who are selected on the basis of peer reviewed research proposals), and 30% for in-house research. A minor part of the beam time for external users (up to 20% of the total beam time of an instrument) is available for long-term collaborative groups, such as university groups (predominantly German), allowing them to plan research work for theses.

User and instrument statistics

Table 1 gives a short overview on the number of projects performed at BENSC by external users in the years 2007 and 2008. The overall development of the number of external proposals submitted to BENSC as well as the number of accepted proposals through the years 2002 to 2008 is displayed in Fig. 1. There are two calls for proposals per year, in spring and in autumn. The submitted proposals are peer-reviewed by an international Scientific Panel meeting at the HZB. The panel decides on the beam time allocation based on the scientific merits of the proposals.

	Projects		Visitors	
	2007	2008	2007	2008
Germany	66	72	141	151
Europe	95	92	180	175
Others	37	63	61	87
Sum	198	227	382	413

Table 1: Projects performed by external users (visitors) at BENSC in 2007 und 2008

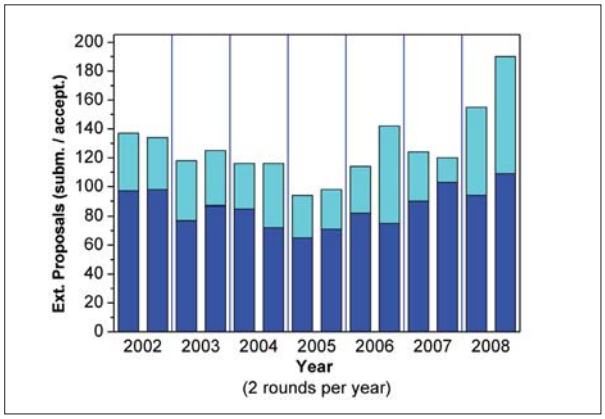

Fig. 1: Number of proposals submitted per round, from 2002 to 2008 (2 proposal rounds per year). The dark-blue part of a bar corresponds to the number of accepted proposals.

The number of proposals submitted has been consistent over the years except for a decline in 2005 which was due to an extended shut-down of several instruments. This shut-down had become necessary for the installation of the new neutron guide system for the second neutron guide hall of BENSC (built in 2004 - 2005). After this shut-down the number of proposals submitted has steadily increased again, most significantly in 2008. The overload factors for the major user instruments of BENSC in 2008-II are given in Figure 2. Here, the average overload factor is 1.7.

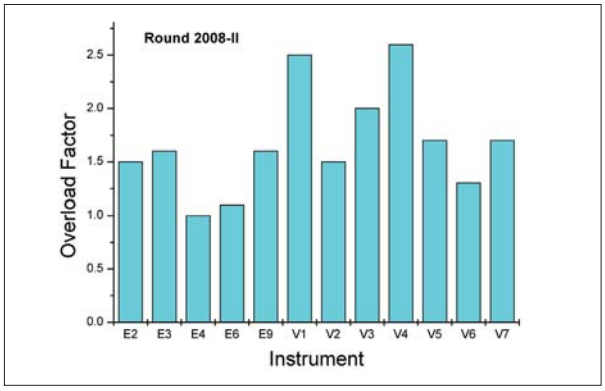

Fig. 2: Overload factors for the major user instruments in 2008-II. Average over all instruments: 1.7.

User Profile

The degree of international recognition for BENSC is illustrated by Figure 3 which shows the origin of the user groups in 2008-II. The figure demonstrates that BENSC has truly established itself as a major research facility for neutron science, with users from throughout the world.

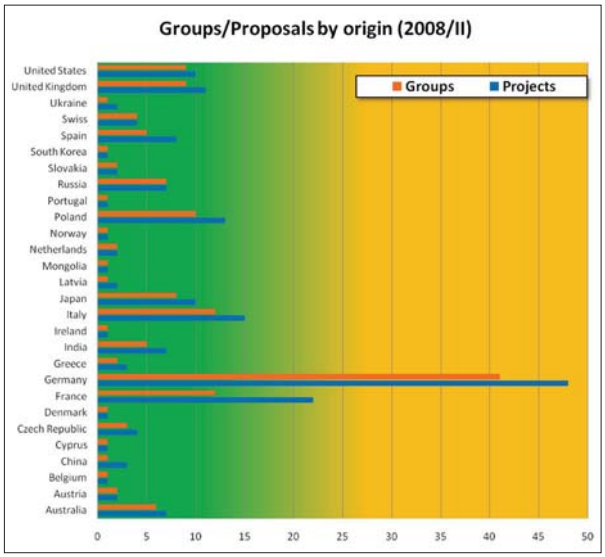

Fig. 3: Origin of users in round 2008-II.

European funding for BENSC

The user programme of BENSC, with its exceptionally large percentage of European users (see Fig. 4), has been highly rated and strongly supported by the European Commission since 1993. Over the last 4 years, a European Access programme has been organised under the 6th EU Framework Programme (FP6), where BENSC is a major partner in the "Integrated Infrastructure Initiative for Neutron Scattering and Muon Spectroscopy (NMI3)".

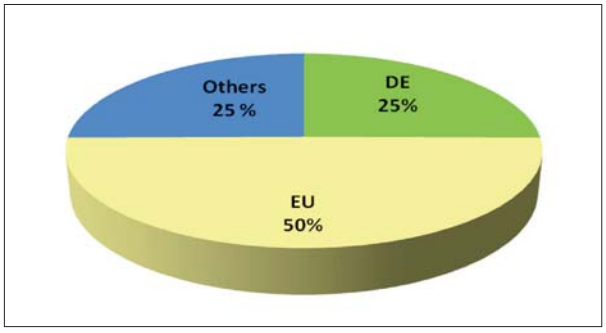

Fig. 4: Proposals from Fig. 3 (round 2008-II) summed up in three categories DE (Germany), EU (EU countries except Germany) and Others (other countries).

Science at BENSC

Figure 5 shows that the scientific topics covered by the external proposals can basically be grouped in three categories of similar size: biology and soft condensed matter (37%), magnetism (36%) and material science plus hard condensed matter (structure) together making 24%. It is interesting and informative to follow the development of these fields of study over the years of BENSC's existence. This is shown in Figure 6 which gives a year-by-year overview of the scientific topics of external as well as in-house projects performed at BENSC since its start in 1993. ▸▸

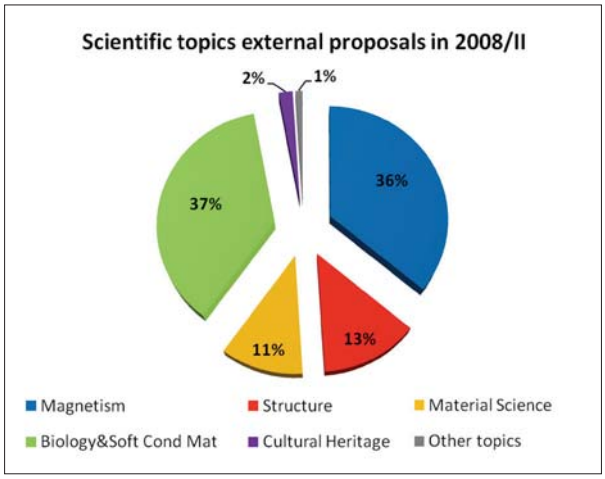

Fig. 5: Scientific fields covered by the external proposals in round 2008-II.

[continued]

BENSC User Operation

Figure 6 clearly demonstrates the increasing importance of neutrons for research on soft condensed matter and bio-related materials. Whilst the field of study of magnetism has stayed rather constant and at a high level (about 30%) over the years, the number of neutron scattering experiments on soft condensed matter and bio-related materials has increased almost linearly from below 10% in 1993 to about 30% in 2007, equal to that of magnetism.

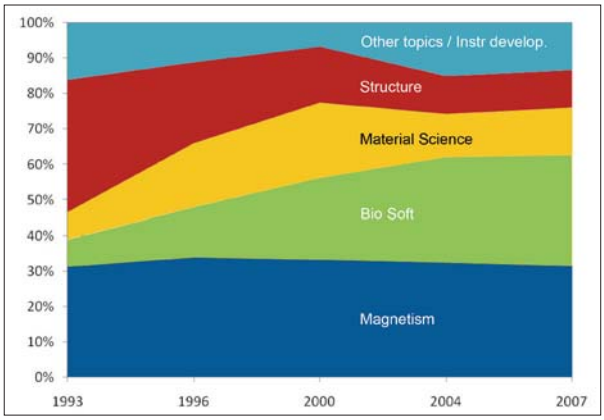

Fig. 6: Development of the scientific fields covered by experiments at BENSC between 1993 and 2007.

It is clear that there is also interdependence between the development of instrumentation for soft-matter experiments and the demand by users of such experimental facilities. When the trend displayed by Figure 6 was recognised, BENSC reacted pro-actively by increasing the experimental capacity, and the number of existing 'work-horse' instrument types for soft-matter experiments is being doubled from 2 to 4. Currently, a second very small-angle scattering machine (VSANS, in the new neutron guide hall) and a second reflectometer (BioRef, a collaborative research project of the University of Heidelberg) are being constructed. These new instruments will be commissioned in 2009.
In addition, a further focus in sample environment is the development of equipment for neutron scattering experiments under controlled gas atmosphere, to serve a growing user community. This new "Dedicated Environment for Combined Gas Adsorption and Scattering Experiments" (DEGAS) includes humidity chambers for investigating biological samples as well as equipment for in-situ adsorption experiments on, for example, metal-organic framework systems. Such mesoporous systems also represent a new scientific focus for material scientists and are being widely explored in terms of their catalytic or hydrogen storage potential. The increasing demand for this new equipment is demonstrated in the article on "News from the Sample Environment" of the present report.

Training the next generation of users

For almost 30 years, the annual Berlin School on Neutron Scattering has been held at HZB. Again in 2007 and 2008, 30 external students and young postdoctoral scientists from different countries were selected to attend this highly regarded training school. Following an introduction to the theory and methods of neutron scattering, the main emphasis was hands-on experience of the neutron scattering techniques at BENSC, including triple-axis spectroscopy, powder diffraction, small angle neutron scattering, reflectometry, time of flight spectroscopy and tomography.

Important events

Outstanding events at BENSC have been the 14th BENSC User Meeting in May 2007, the European Conference on Neutron Scattering (ECNS) in June 2007 (Lund, Sweden) and the celebration of 50 years of research with neutrons at HZB in 2008.
The BENSC User Meeting attracted 117 participants, 52 of them coming from HZB, 34 from other German institutes and 31 from foreign research institutions. The 15 invited lectures and 53 poster contributions gave ample opportunity for lively discussions and scientific exchange on the latest results from experiments performed at BENSC.
At the ECNS in Lund, there were an extraordinarily high number of scientific contributions from work undertaken at BENSC, as has been the case at previous conferences. Of the 612 posters presented at Lund, 17% were based on BENSC experiments performed by inhouse scientists and external users. This was the largest number of contributions from a single centre after the Laue-Langevin Institute (ILL, 24%) and much greater than that of other centres.
In July 2008, HZB celebrated the 50th anniversary of the first research reactor BER-I becoming critical. Numerous neutron scientists from other centres, current users and retired employees joined the staff of HZB in their celebration. During the two days, the participants enjoyed a varied scientific programme on past, present and future neutron science in Berlin and elsewhere.

Important forthcoming changes

By January 2009, two of Berlin's largest research centres, the Hahn-Meitner-Institut and the Berlin synchrotron radiation source BESSY, will merge to form the HZB - Helmholtz-Zentrum Berlin für Materialien und Energie GmbH. With this merger, a new era dawns in the user facilities of the joint institute. HZB will be one of the few centres worldwide that is able to offer the whole range of instruments for neutron and synchrotron radiation experiments in one laboratory structure. A common user entry point, a unified proposal procedure and one common scientific panel for both facilities will help to facilitate the synergistic use of neutron and synchrotron radiation.

NAA Laboratory and Irradiation Service

D. Alber, G. Bukalis, B. Stanik, F. Zepezauer
Helmholtz-Zentrum Berlin für Materialien und Energie

The laboratory for neutron activation analysis (NAA) in the BER II research reactor at Helmholtz-Zentrum Berlin provides irradiation services for universities, scientific institutions and industry.

Typical fields of application are:
- Trace elements analysis by means of NAA, for example in biology, medicine, geology and archaeology. Certification of reference materials.
- Irradiation experiments, such as isotope production for medical applications, sources for Mößbauer spectros copy and production of tracers for scientific and industrial applications.

The operation and further development of the irradiation devices and the NAA measuring systems at BER II is a central task of Department SF6.

Fig.1: Wheat plants enclosed in ampoules made of high purity silica

Irradiation devices

Three irradiation devices are available for different applications.

DBVK: irradiation device in the reactor core
DBVR: rotatable irradiation device in the Be-reflector of the reactor core
TBR: dry irradiation device outside the Be-reflector

DBVK and DBVR are used for long term irradiation experiments. Up to nine aluminum containers can be irradiated simultaneously. Usually the samples have to be enclosed in ampoules made of high purity silica. Short time irradiation experiments are carried out by means of TBR. The samples have to be enclosed in containers made of polyethylene.

Device	Φthermal	Φfast	Container
	[1/cm²s]	[1/cm²s]	
DBVK	1,5E+14	4,3E+13	6
DBVR	7,5E+12	1,9E+10	9
TBR	3,4E+12	2,2E+10	1

Table 1: Fast and thermal neutron flux at different irradiation positions

Irradiation Experiments 2007 and 2008

Most of the irradiation experiments (243 in 2007; 334 in 2008), were performed using the DBVK or DBVR. With these devices it is possible to irradiate up to 24 samples simultaneously in one aluminum container.

Internal users

Most of the internal users are from Department SF6, but irradiation and analyses were also performed for users from other departments (SF2, SF4, SE5, RE).

External users

Irradiation experiments and NAA were performed for users from German universities (Berlin, Mainz, Münster, Leipzig, Nürnberg) and from research institutes, such as Bundesanstalt für Materialforschung und -prüfung (BAM, Berlin), GSF Forschungszentrum für Umwelt und Gesundheit (Neuherberg), and Fraunhofer Institute (Dresden). For industrial companies neutron activation analysis was performed and radioactive materials were produced for tracer experiments.

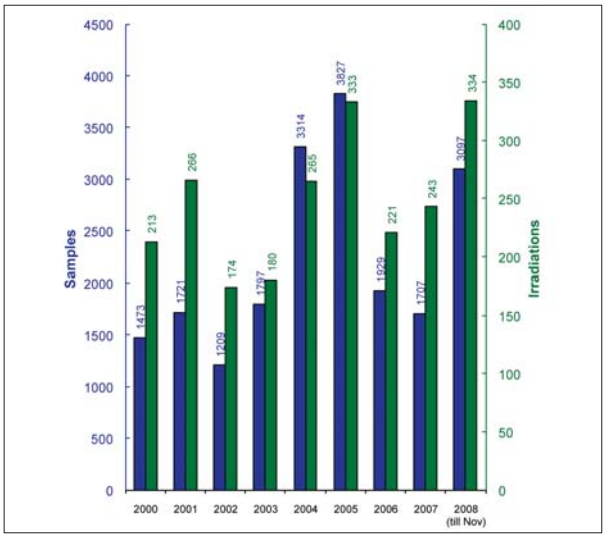

Fig.2: Statistics for irradiated samples and irradiation experiments

Scientific Highlights
Structural Research 2007/2008

(Photo: X-ray image of "Wie die Alten sungen, so zwitschern die Jungen")

Neutron- and synchrotron radiography – two complementary methods for liquid water detection

Christoph Hartnig[1], Philipp Krüger[1], Robert Kuhn[1], Ingo Manke[2]

■ 1 Zentrum für Sonnenenergie- und Wasserstoff-Forschung, Helmholtzstr. 8, 89081 Ulm, Germany

■ 2 Helmholtz-Zentrum Berlin für Materialien und Energie, Glienicker Str. 100, 14109 Berlin, Germany

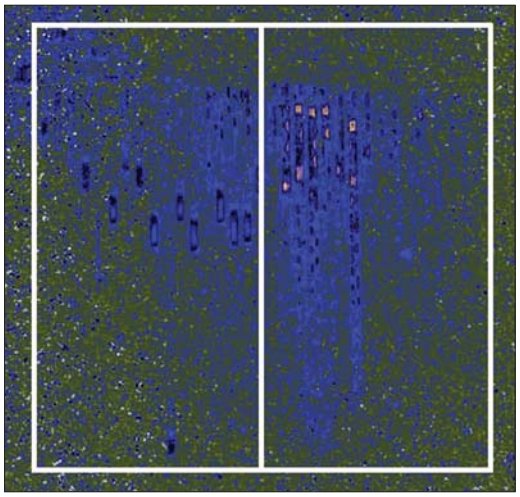

Fig. 1: Neutron radiographic imaging of water transport in an operating fuel cell. The droplet shape has changed caused by different surface properties on the left and right side.

Neutrons are well known for their property to penetrate metallic components almost unattenuated but bear a high sensitivity towards hydrogen containing species; this led worldwide to research activities in fuel cell research, where these two properties are used to optimize performance and durability: liquid water, which forms an obstacle in the transport pathways for the reactant gases, oxygen and hydrogen, has to be detected inside the operating fuel cell, shielded by a metallic housing and other components made of steel or graphite composite materials. Within the last couple of years, synchrotron based methods emerged to a suitable complement in this field to extend the observation scale towards the micrometer level.

Neutron radiography allows for a visualization of the complete electrochemically active area, where the reaction of hydrogen and oxygen takes place and water results as a product. The typically accessible area is in the range of 100-200 cm^2 which agrees well with state-of-the-art fuel cells geometries. The flow field structure, the component of the fuel cell that is responsible for a uniform distribution of the reactant gases, can be optimized that way. Another range of applications focuses on the in situ characterization of the gas diffusion media: the porous media ensures the transport of the reactants to the catalyst particles and of product water from the catalyst to the gas channel where it is removed from the cell. Issues such as impregnation or structural properties influence the liquid water transport and have a significant impact on the performance. In Figure 1 an example of two materials with varying impregnation composition is given: the left material leads to larger droplets and an improved release of the droplets from the surface compared to the material on the right part.

Due to resolution limitations of around 50 µm, only the formation of larger water droplets can be investigated by means of neutron based methods.

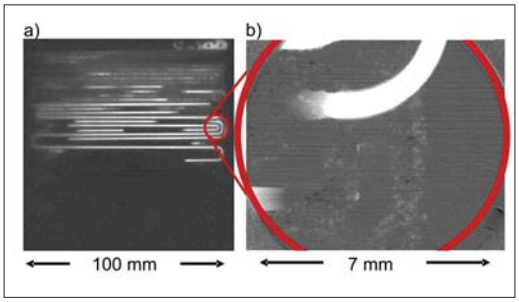

Fig. 2: Complementary character of neutron and synchrotron based methods.

Complementary results can be obtained by synchrotron radiography: as demonstrated in figure 2, the resolution is increased by almost two orders of magnitude allowing for a detection of the initial evolution of small water clusters which has been successfully reported for the first time by our group.

A pseudo three-dimensional and therefore very detailed insight in a fuel cell under operating conditions results from different viewing directions.

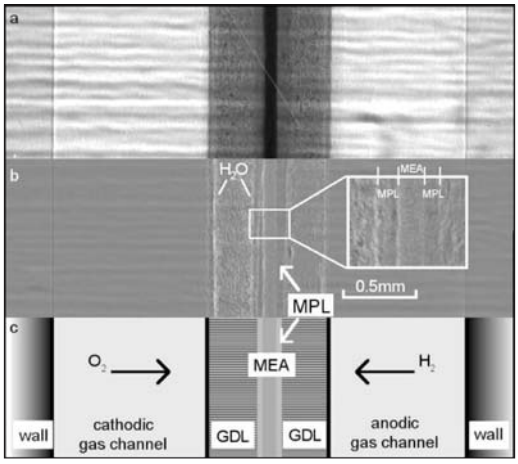

Fig. 3: Cross-sectional viewing direction. a) Uncorrected image, b) After normalization with respect to an 'empty cell', c) Components

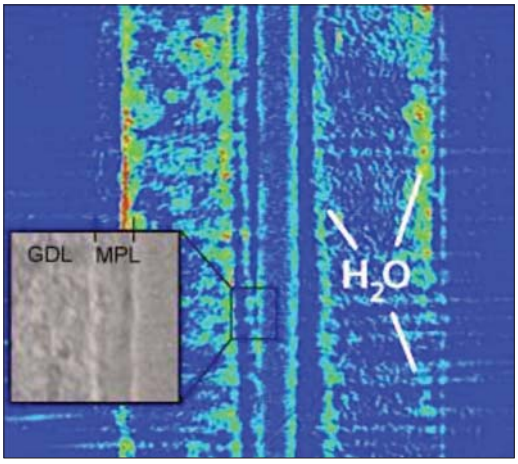

Fig. 4: Transport pathways can be observed from the catalyst layer through the gas diffusion layer (GDL) to the gas channel.

The layers of different components are visible on images in the cross sectional viewing direction, as shown in figure 3. In a further magnification, figure 4, the water distribution and transport processes in the fuel cell assembly can be observed and liquid water can be quantified in the different components. The applied methods were engaged to visualize these effects in a so far unique temporal and spatial resolution. In addition, the through plane viewing direction allows for insights in the specific spots of primary liquid water evolution which are of major interest in an operating fuel cell, the areas under the lands and the channels of the gas distributing flow field. In figure 5, water cluster are detected at different points in the cell. The gas channels are traced in grey and black. At point 1 a water droplet is observable located next to the channel wall. The origin of this droplet is situated at point 2 in the area under the rib, which is free of water in this image. At point 3 liquid water clusters under the rib are detected without droplet generation.

The combination of both viewing directions has been chosen in order to get a pseudo-3D insight in processes on a microscopic scale. An overlay of both aspects allows for an estimation of the total area involved in the liquid water formation and serves as essential input to build and verify multiphase models; development aspects with regard to optimal shape and properties of the employed components can be also addressed.

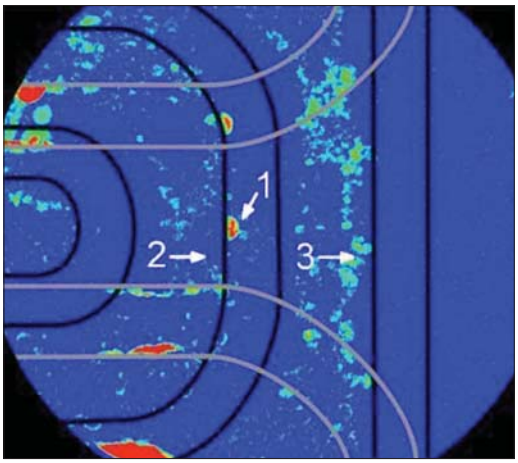

Fig. 5: Liquid water formation rendered visible in the through plane viewing direction: 1) in a gas channel, 2) under the rib next to the channel, and 3) under the rib without direct contact to the gas flow in the channels.

Corresponding authors:
Ingo Manke
manke@helmholtz-berlin.de

Pore network organisation in hierarchical mesoporous silica studied using a combination of gas physisorption with SANS

Simone Mascotto[1], Dirk Wallacher[2], Astrid Brandt[2], Thomas Hauss[2], Bernd M. Smarsly[1]

■ 1 Institute of Physical Chemistry, Universität Giessen, Heinrich-Buff-Ring 58, 35392 Giessen, Germany

■ 2 Helmholtz-Zentrum Berlin, Glienicker Straße 100, 14109 Berlin, Germany

In the past years significant progress has been made in the characterisation of ordered mesoporous materials (pore size between 2 and 50 nm). Standard analytical methods, like small-angle scattering (SAS) and physisorption can be successfully applied to the study of their structural and morphological features (e.g. specific surface area, pore volume and pore size). Although these techniques are widely applied, additional independent experimental methods can be useful especially in the understanding of the sorption mechanism. Recently, the combination of a physisorption experiment with small-angle neutron scattering (in-situ sorption-SANS) was introduced at Helmholtz-Zentrum Berlin (HZB) to provide more details about the porosity and connectivity, which cannot

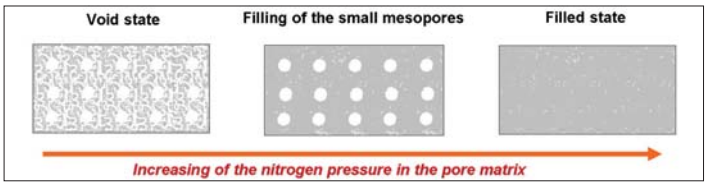

Fig. 1: Scheme of the nitrogen filling in mesoporous silica from "the point of view" of a neutron

be obtained by the single methods themselves. Recently, the use of this combination technique has given relevant results on sorption theory and represents an elegant way to describe the physisorption process in mesoporous materials. [1,2].

The system object of our study is a "hierarchical" mesoporous silica (KLE-IL) which presents a trimodal pore size distribution with distinct maxima at around 1.3 nm, 2-3 nm (cylindrical/worm-like mesopores) and 14 nm (spherical mesopores). We define a "hierarchical" pore system as a pore architecture with the small pores being located in the walls of the larger ones. A considerable amount of microporosity is present in such materials, in addition to the ordered mesoporosity arising from the templating action of the KLE block-copolymer (producing 14 nm spherical mesopores) and of the surfactant-like C_{16}mimCl ionic liquid (generating 2-3 nm cylindrical mesopores) [3].

The SANS experiment involves in-situ nitrogen adsorption at 77 K. The experiment is based on the principle of "contrast matching", with the scattering lengths of the amorphous KLE- silica matrix ($3.43*10^{10}$ cm^{-2}) and condensed nitrogen ($3.22*10^{10}$ cm^{-2}) being almost identical, and thus negligible scattering contrast is present in the filled state [2-4].

In these investigations the relative vapour pressure $p/p°$ of the pore condensate could be controlled during the scattering experiment ($p°$ is the saturation vapour pressure of the bulk condensate at the given temperature). The gas adsorption sample environment (CGA-PT) allows the direct in-situ measurement of a complete pV isotherm. Some of these results are shown in Figure 1, which represent crucial adsorption states of the sorption process (i.e., micropore filling and small mesopores, nitrogen condensation in the larger mesopores). In this context, the essential advantage of the contrast matching conditions is shown, in that filled pores do not contribute to the SANS pattern of the mesopore structure. Therefore, this method is highly sensitive to the pore structure and pore connectivity and perfectly suited to proving the hierarchical order of the KLE-IL porous silica.

The SANS curves (Figure 2), collected at different pressure steps, show various interesting features regarding the porosity and the filling process. First, the pressure-dependent experiments proved that

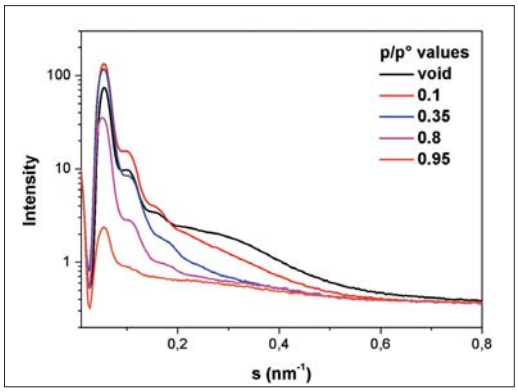

Fig. 2: SANS curves during nitrogen condensation in KLE-IL silica

the SANS data themselves could be attributed to a superposition of three different types of pores. At $p/p° = 0$, the shape of the curve $s<0.25$ nm^{-1} was attributable to the 14 nm KLE mesopores and (based on the relative pressures at which these scattering contributions disappeared) the broad maxima at $s = 0.55$ nm^{-1} and $s = 0.3$ nm^{-1} were assigned to the micropores and small IL mesopores, respectively. Interestingly, at $p/p° > 0.35$, further oscillations corresponding to the form factor of the large spherical KLE mesopores, became visible. At $p/p° = 0.95$ the scattering patterns almost vanish implying that all the pores were filled with nitrogen. Second, and more importantly, the relative overall intensity of the SANS curves showed interesting changes as a function of $p/p°$. Starting from $p/p° = 0$, the SANS curve (below $s = 0.15$ nm^{-1}) underwent a significant, continuous overall increase up to $p/p° = 0.3$-0.35, which coincides with the filling of the micropores and small mesopores. This can be explained by the enhancement of the contrast between the empty KLE mesopores and the silica matrix, producing higher intensity of the Bragg peak at $s = 0.08$ nm^{-1}.

Despite interesting outcomes by the gas condensation in the mesopores, the in-situ SANS technique can also be successfully applied in the understanding of the pore emptying mechanism of porous solids. Until now, two main theories have been used to explain this phenomeon: cavitation and pore blocking. However, cavitation (spontaneous nucleation of a bubble) is only predicted and has not yet been experimentally proven.

The pore blocking effect (see Figure 3) is expected to occur if the pore only has access to the external surface through a narrower neck, as in the ink-bottle pore. The wide body of the ink-bottle pore remains filled during desorption, until the narrow neck empties first at a lower vapour pressure. Thus, in a network of ink-bottle pores, evaporation of the capillary condensate is obstructed by the pore necks. The vapour pressure, at which a pore body empties, depends upon the size of the necks, the connectivity of the network, and the state of the neighbouring pores. By contrast, recent studies have suggested that, if the neck diameter is smaller than a certain critical size (~ 5 nm) at a given experimental temperature, desorption from the pore body occurs via cavitation. In this case the pore body can empty by diffusion, while the pore neck remains filled [5].

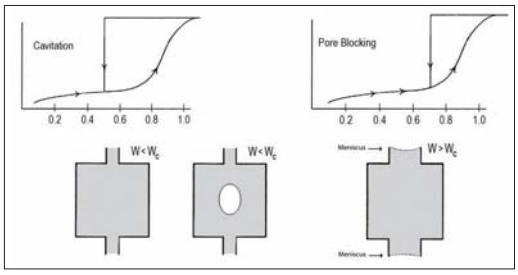

Fig. 3: Scheme of the pore emptying mechanism of cavitation and pore blocking

The use of the in-situ SANS technique offered the unique chance to check the emptying mechanism. The nitrogen desorption at 77K of KLE-IL silica was followed by SANS and is presented in Figure 4. As can be seen, the progressive increase in the intensity of the Bragg maximum at

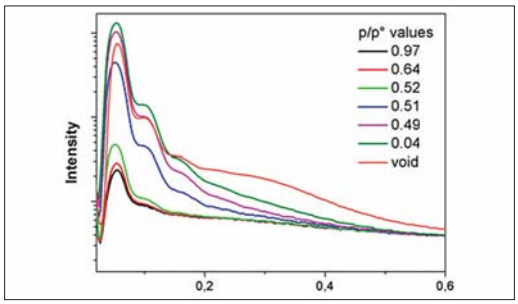

Fig. 4: SANS patterns during the nitrogen desorption branch in KLE-IL silica

$s = 0.08$ nm^{-1} peak for $p/p° = 0.5$, reveals the emptying of the KLE cavities with the IL mesopores still being filled. At smaller relative pressure values ($p/p° < 0.49$) the enhancement of the scattering intensity at $s = 0.3$ nm^{-1} evidences the subsequent draining of the IL mesopores and micropores. This finding is a direct proof of the cavitation pore emptying mechanism.

These first studies give an indication of how this new and elegant approach in the analysis of mesoporous material may provide the answers to many unanswered questions. Furthermore, the in-depth mathematical quantitative investigation of the SANS curves (which was not shown here for the sake of clarity) offer the chance to study the sorption mechanism and its particularities for mesoporous solids in greater detail.

[1] O. Sel, A. Brandt, D. Wallacher, M. Thommes, B. Smarsly Langmuir 2007, 23, 4724-4727
[2] B. Smarsly, C. Göltner, M. Antonietti, W. Ruland, E. Hoinkis J. Phys. Chem. B 2001, 105, 831-840
[3] O. Sel, D. B. Kuang, M. Thommes, B. Smarsly Langmuir 2006, 22, 2311-2322.
[4] E. Hoinkis Part. Part. Syst. Charact. 21 2004 80 – 100
[5] M. Thommes, B. Smarsly, M. Groenewolt, P.I. Ravikovitch, A.V. Neimark Langmuir 2006, 22, 756-764

Corresponding author:
Bernd M. Smarsly
bernd.smarsly@phys.chemie.uni-giessen.de

What neutron autoradiography tells us about Old Masters: The genesis of Jan Steen's *"Wie die Alten sungen, so zwitschern die Jungen"*

Dr. Katja Kleinert[1], Maria Reimelt[2]
■ 1 Helmholtz-Zentrum Berlin für Materialien und Energie, Bereich Strukturforschung, Glienicker Str. 100, 14109 Berlin ■ 2 Gemäldegalerie Berlin, Restaurierungswerkstatt, Stauffenbergstraße 40, 10785 Berlin

Fig. 1: Jan Steen, *"Wie die Alten sungen, so zwitschern die Jungen"*, 1665/66, canvas, 84.8×100.4 cm, Gemäldegalerie Berlin

The Gemäldegalerie Berlin, Stiftung Preußischer Kulturbesitz (Berlin Picture Gallery) and Hahn-Meitner-Institut cooperate closely on investigating paintings by Old Masters by means of neutron autoradiography. This is a very effective, non-destructive, if rather unusual method applied to the examination and analysis of materials and techniques used in painting. It allows the visualisation of structures and layers beneath the surface and, in addition, enables the detailed identification of the elements contained in the pigments. The instrument B8 at Berlin Neutron Scattering Centre (BENSC) is dedicated to these investigations. In this report, the efficiency and success of this method are demonstrated on a painting by the Dutch artist, Jan Steen.

Jan Steen may be considered as one of the most prolific artists of the 17th century. Like many other

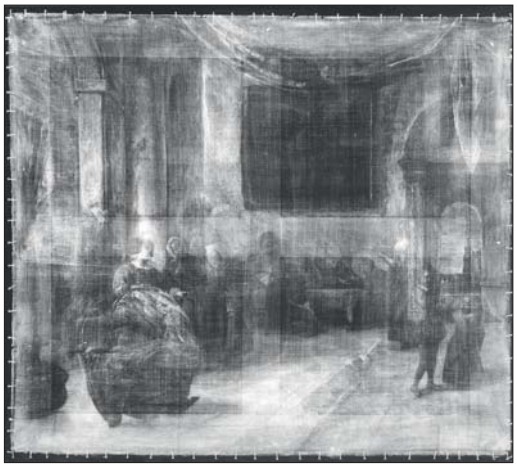

Fig. 2: X-ray image of *"Wie die Alten sungen, so zwitschern die Jungen"*. The X-ray image already shows that large areas of the painting, like the drapery on the upper part or the archway on the right, have been changed during the painting process.

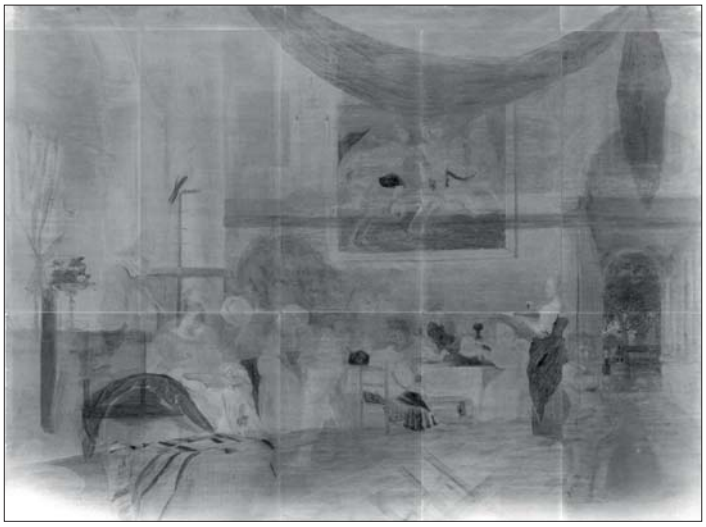

Fig. 3: First neutron autoradiography of *"Wie die Alten sungen, so zwitschern die Jungen"*, depicting clearly the drapery and the landscape in the archway.

painters of that time, he produced several variations on the same theme during his career, following a dedicated scheme of iconographic motives and a defined canon of pictorial elements. The painting *"Wie die Alten sungen, so zwitschern die Jungen"*, roughly translated as "the young cock crows like the old one" or "like mother, like daughter" (Figure 1), which belongs to the Gemäldegalerie Berlin, depicts a topic which Jan Steen addressed in 13 different pictures. However, the Berlin painting is an exception in this series, as it differs in form and content from the other works. Hence the question arises: Why did the artist go to such trouble to deviate from his accustomed paint schemes?

The answer is revealed by X-ray images (Figure 2) and neutron autoradiographies of the painting (Figures 3 and 4). These methods provide insights into paint layers that are hidden today and uncover information about the painter's work process. They show that Jan Steen not only made drastic changes to the composition of the room with regard to the figure groups, but originally had a completely different subject in mind. Most probably, it was a so-called "merry company" in a spacious, stately room. Numerous elements of this original, much more sophisticated ambiance were eliminated by the artist in the version now visible. Essential elements – like the representative arrangement of the room – were retained, but adapted and blended in the composition of the new painting. In this way, Jan Steen integrated the topic *"Wie die Alten sungen, so zwitschern die Jungen"* into a context which was originally designed for a different painting. Apart from revising the composition of the picture, Jan Steen also made essential changes to the iconography of the painting. It can be assumed that these intelligent iconographic alterations were due to the unsuccessful painting process in the first painting: Jan Steen was forced to find the most effective way of using the existing composition if he wanted to save at least a small part of the work already carried out.

Until now, it had not been possible to place the Berlin painting in the chronological order of Jan Steen's oeuvre, especially as he seldom dated his paintings. On the evidence of several characteristic motifs, visible only in the autoradiographies (sometimes just details), and further art historical references, it is now possible to narrow down the date of origin with a high degree of accuracy.

Fig. 4: Second neutron autoradiography of *"Wie die Alten sungen, so zwitschern die Jungen"* with contour drawings of the reconstructed original version.

Corresponding author:
Andrea Denker
denker@helmholtz-berlin.de

Synthesis and cycling behaviour of lithium borohydride

A. Remhof[1], O. Friedrichs[1], Ph. Mauron[1], F. Buchter[1], A. Züttel[1], A. Buchsteiner[2], D. Wallacher[2]

■ 1 Empa - Swiss Federal Laboratories for Materials Testing and Research, Division Hydrogen and Energy, Überlandstrasse 129, 8600 Dübendorf, Switzerland ■ 2 Helmholtz-Zentrum Berlin für Materialien und Energie GmbH, BENSC, Glienicker Strasse 100, 14109 Berlin, Germany

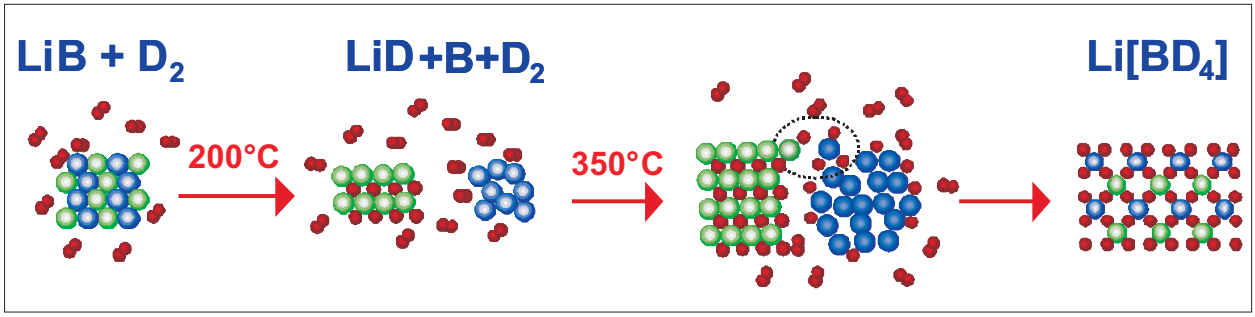

Fig. 1: Schematic view of the $LiBD_4$ synthesis from LiB and D_2.

A future hydrogen economy relies on dense, safe, efficient and reversible hydrogen storage. This can either be achieved by the use of compressed gas, by liquefaction or by solid-state storage. Among these alternatives, metal hydrides and complex hydrides reach the highest volumetric densities, even exceeding that of liquid hydrogen without the need of cryogenic temperatures or high pressures [1,2].

The fundamental properties of a technical applicable hydrogen storage material are (i) a high storage capacity, (ii) fast sorption kinetics and (iii) a convenient working temperature. Due to their combined large volumetric and gravimetric storage capacity, complex borohydrides such as lithium borohydride ($LiBH_4$) are the focus of many research activities world-wide. A major hindrance to their technical applications is their high stabilities, leading to high desorption temperatures. Additionally, the rather slow kinetics of the sorption processes remains a challenge. In view of technical applications, the conditions for the synthesis (i.e. the production) and for the hydrogen cycling (i.e. the hydrogen extraction and refuelling), have to be further improved. Here we present new insights in the synthesis and in the cycling behaviour of $LiBH_4$ gained by in-situ neutron diffraction.

$LiBH_4$ melts at 280°C and decomposes in the liquid phase to LiH, B and H_2 according to the reaction $LiBH_4 \rightarrow LiH + B + 3/2H_2$. The thermodynamic parameters of the desorption have been determined from pressure–composition isotherms according to the van't Hoff law to be $\Delta H = 74$ kJ $(mol\ H_2)^{-1}$ and $\Delta S = 115$ J K^{-1} $(mol\ H_2)^{-1}$, respectively [3]. The reverse reaction, i.e. the synthesis of $LiBH_4$ from it's desorption products requires elevated temperatures (T=600°C) and pressures (p=155bar H_2) [3]. For every day use these values are far too high. We succeeded in reducing the required pressures and temperatures by using pre-annealed Li/B mixtures or AlB_2 and LiH as starting materials. The reactions were monitored in collaboration with the DEGAS laboratory, by combined in-situ neutron diffraction using the focussing diffractometer E6 and gas absorption measurements. ^{11}B was chosen to avoid the strong neutron absorption by ^{10}B that is present in natural boron and D_2 was chosen instead of H_2 to maximise the coherent scattering cross section. We observed the direct, solvent free synthesis of $LiBH_4$ from the elements at 700°C with an applied hydrogen pressure of 150bar. Pre-annealing of Li and B prior to the hydrogen exposure (p=150bar H_2) facilitated the formation [4]. The initial binary compound could be identified as LiB. In a first reaction step the D replaces the B, LiB decomposes and LiD forms. The subsequent synthesis of $LiBD_4$ starts at 350°C, facilitated by the higher reactivity of the B, which is liberated in the decomposition of the binary compound LiB. The resulting reaction scheme is shown in Figure 1 [5]. A further improvement could be reached by using AlB_2 and LiH as starting materials. The synthesis would follow the reaction $AlB_2 + 2LiH + H_2 \rightarrow 2LiBH_4 + Al$. Again, the reactivity of the B liber-

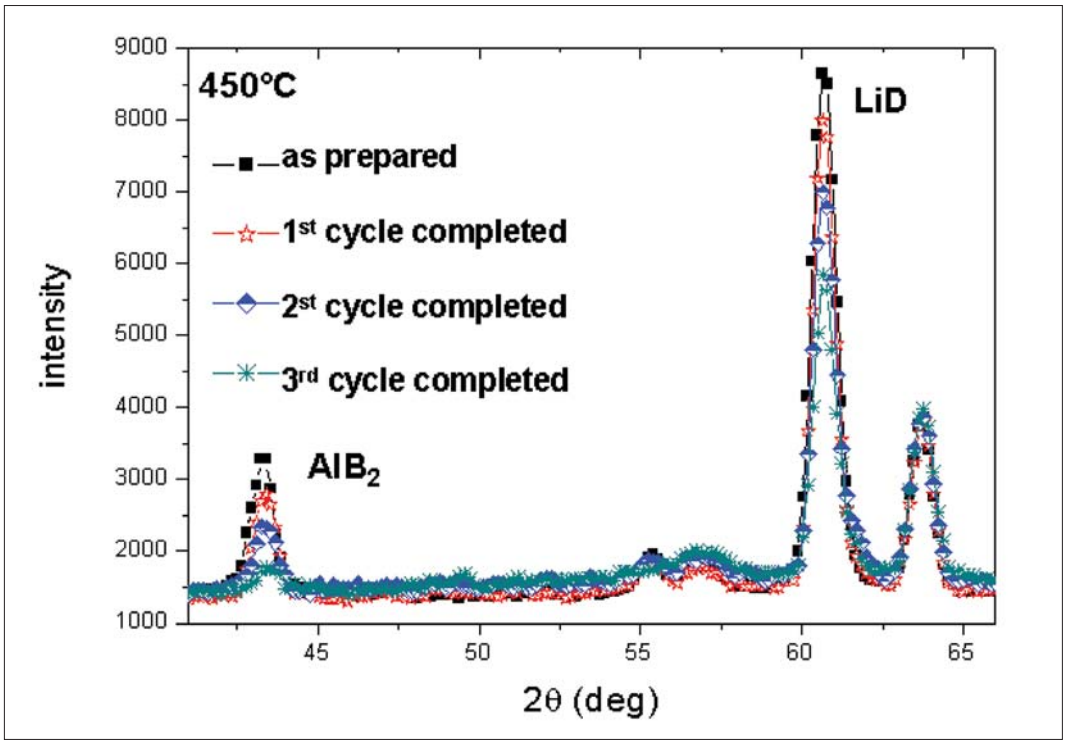

Fig. 2: Cycling of $LiBD_4$ and Al according to $AlB_2 + 2LiH + H_2 \leftrightarrow 2LiBH_4 + Al$, monitored by in-situ neutron diffraction.

ated, this time from AlB_2, facilitates the reaction, which starts at 450°C and at a pressure $\leq$ 25 bar, which is much lower than the pressures reported for the direct synthesis. The presence of Al also improves the cycling behaviour with respect to kinetics and the required pressure and temperature as compared to the pure system. However, the hydrogen capacity decreases from cycle to cycle due to an incomplete re-formation of AlB_2 as shown in Figure 2. We attribute this to a phase separation of Al and B during the decomposition of the $LiBH_4$.
Neutron diffraction helps to reveal the crystalline structure and the reaction path during the hydrogen sorption/desorption cycle of complex metal hydrides. It is hoped that further understanding of the hydrogen dynamics within these systems will be gained in the future by the use of inelastic and quasielastic neutron spectroscopy.

Financial support from the European Commission's 6th Framework Programme (NESSHY Contract No.: 518271), the Swiss National Science Foundation (SNF-Project 200021-119972/1) and the Swiss Federal Office of Energy is gratefully acknowledged. We would also like to thank Norbert Stüßer and Andreas Hoser for their technical and scientific support.

[1] L. Schlapbach and A. Züttel, *Nature*, 414 535 (2001). 414, 535.
[2] G. W. Crabtree, M. S. Dresselhaus and M. V. Buchanan, *Phys.Today*, 39 57 (2004).
[3] Ph. Mauron, F. Buchter, O. Friedrichs, A. Remhof, M. Bielmann, C. N. Zwicky, A. Züttel, *Phys. Chem*. B 112 906 - 910 (2008).
[4] O. Friedrichs, F. Buchter, A. Borgschulte, A. Remhof, C.N. Zwicky, Ph. Mauron, M. Bielmann, A. Züttel, *Acta Mater.* 56 (5), 949-954 (2008).
[5] A. Remhof, O. Friedrichs, F. Buchter, Ph. Mauron, A. Züttel and D. Wallacher, *Phys. Chem. Chem. Phys.* 10, 5859–5862 (2008).

Corresponding author:
A. Remhof
arndt.remhof@empa.ch

Uptake of 1.4 nm versus 18 nm Gold particles by secondary target organs is size dependent in control and pregnant rats after intratracheal or intravenous application

M. Semmler-Behnke[1], S. Fertsch[1], G. Schmid[2], A. Wenk[1], W.G. Kreyling [1]

■ 1 Helmholtz-Zentrum München - Deutsche Forschungszentrum für Gesundheit und Umwelt, Institut für Inhaltationsbiologie, Neuherberg, München, Deutschland ■ 2 Universität Duisburg-Essen, Institut für Anorganische Chemie, Essen, Deutschland

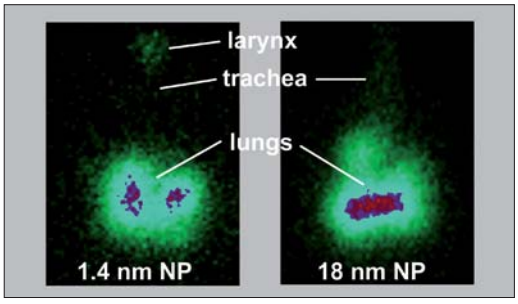

Fig. 1: SPECT gamma camera (Prism 2000, Philips) image of 198Au activity distribution (applying pinhole collimation geometry) in the lungs of animals 1 h after intratracheal instillation of 1.4 nm and 18 nm NPs.

With the advent of nanotechnology, the interaction of nanoparticles (NPs) and nano-structured surfaces with biological systems (including living cells) has become one of the most intriguing areas of basic and applied research at the interface of biology. As NPs are of the same size scale as typical cellular components and proteins, such particles are suspected of evading the natural defences of the human body and may lead to permanent cell damage[1]. This includes NP transfer across biological membranes, NP interactions with proteins and cellular constituents as well as the impact of NPs on important biological functions. In order to assess the effects of NPs, potential target organs and cells need to be known[2]. Target organs may not be restricted to the organ of intake but may include secondary target organs and their cellular constituents, depending on the accessibility of NPs to these sites. Since the interest in gold (Au) NPs continues to grow in nanobiotechnology we selected these for our biokinetic studies[3-5]. We aimed to investigate the effect of the size of monodispersed NPs, keeping the NP material and its ionic ligand coating constant. We compared 1.4 nm sized gold NPs[6-8] with 18 nm gold NPs[9], both stabilised by negatively charged ionic ligands in aqueous solution and radio-labelled with 198Au. Healthy adult Wistar-Kyoto (WKY) rats received radio-labelled gold either by an intratracheal (IT) route or intravenously (IV) in 50 µl of physiological saline in the tail vein. After NP administration, images were taken under a single photon emission computed tomograph gamma camera (SPECT, Prism 2000, Philips), equipped with a pinhole collimator. Rats were killed 24 hours after administration and all organs and tissue samples as well as the remaining carcass, urine and faeces were analysed quantitatively by gamma-spectrometry. The biokinetics in rats after NP administration were compared in two important organs of intake, the lungs and the blood.

These biokinetics in-vivo studies were conducted in healthy, adult female WKY rats (~250g body weight) and performed under German federal guidelines for the use and care of laboratory animals and were also approved by the responsible regional authorities (Regierung von Oberbayern, Approval No. 211-2531-94/04) and by the GSF Institutional Animal Care and Use Committee.

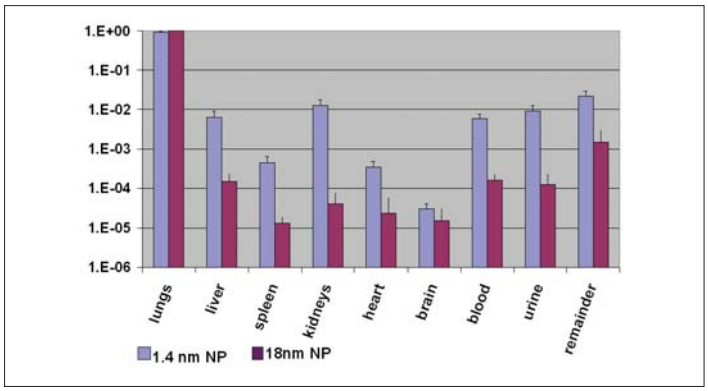

Fig. 2: Translocated NP fractions in secondary target organs 24 h after particle instillation into the lungs (data are corrected for fast clearance).

Twenty-four hours after IT administration, there was considerable retention of NPs in the lung, at both particle sizes. After correction for fast clearance

(the amount of particles which were deposited in the upper airways and cleared via the mucociliary escalator within 24 h) more than 90 % of the administered particles remained on the lung surface (see Figures 1 and 2).

We found a highly significant inverse size dependency with more than a 20-fold higher accumulation of 1.4 nm NPs in secondary target organs (0.039 fraction versus 0.0018 for 18 nm NP ($p<0.001$)). With correction of the particle fraction for fast clearance we found 7% of 1.4 nm NPs translocated into the circulation and to secondary organs, with a 25-fold less translocation for 18 nm colloids. Similarly, the 0.006 fraction of 1.4 nm NPs circulating in blood was 30-fold higher than the 0.0002 fraction for 18 nm NPs. In almost all secondary target organs, translocated fractions of 1.4 nm NPs are mostly up to 2 orders of magnitude larger than for 18 nm NPs (see Figure 2).

Twenty four hours after intravenous injection, the fraction of circulating 1.4 nm NPs in blood (0.037) was 130-fold higher than that of 18 nm NPs (0.00027). This shows that more than 0.96 and 0.99 of the fractions respectively had been taken up by secondary target organs. However, only 0.49 of the 1.4 nm NP fraction was retained in the liver versus 0.94 for 18 nm NPs. Hence, a much larger fraction of the 1.4 nm NPs was distributed in the other organs and tissues compared to 18 nm NPs (see Figures 3 and 4). In the remaining carcass (including muscles and skeleton), we found a 0.16 fraction versus 0.020 for 1.4 nm and 18 nm

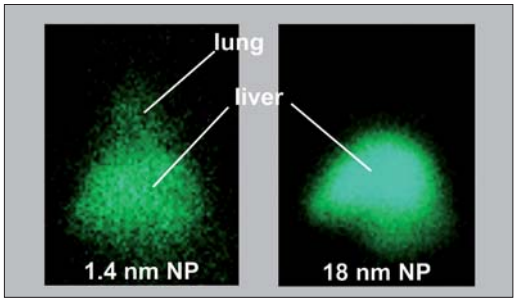

Fig. 3: SPECT gamma camera (Prism 2000, Philips) image of ^{198}Au activity distribution (applying pinhole collimation geometry) 1 hour after intravenous injection of 1.4 nm and 18 nm NPs.

NPs respectively. In addition, a remarkable fraction (0.057) of the 1.4 nm NPs was excreted in the urine, 1000-fold higher than for the 18 nm NPs. Interestingly, a considerable fraction of both 1.4 nm and 18 nm NPs were found in the gastrointestinal tract and faeces, 0.051 and 0.014 respectively. We hypothesise that the excreted fraction was predominantly associated with NPs coming from the liver via the bile and entering the small intestine, thus indicating a strong inverse size dependence of this

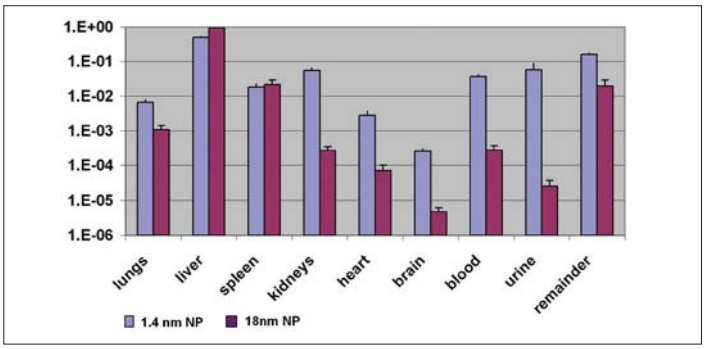

Fig. 4: Translocated NP fractions into secondary target organs 24 h after intravenous injection of the NPs into the tail vein.

clearance mechanism. In the secondary target organs (kidneys, heart and brain) we found about 100-fold more of the 1.4 nm NP fraction compared to the 18 nm NP fraction (see Figure 4).

Twenty-four hours after IV-injection of either sized gold NPs in pregnant rats we found a strong and size-dependent uptake of these NPs by the placenta (about 3% of 1.4 nm NPs and about 0.02% of 18 nm NPs) and thereby also in the foetus (0.06% and 0.005% respectively).

Conclusion: By using NPs of differing sizes but with the same NP matrix, these experiments show that the size of the gold NPs clearly affects translocation kinetics across the alveolar air-blood barrier and vascular endothelium. Potential adverse health effects in secondary target organs require further investigation.

[1] Oberdörster, G.; Oberdörster, E.; Oberdörster, J. *Environ Health Perspect* 2005, 113, (7), 823–839.
[2] Maynard, A. *Nano Today* 2006, 1, (2), 22.
[3] Chithrani, B. D.; Ghazani, A. A.; Chan, W. C. *Nano Lett* 2006, 6, (4), 662-8.
[4] Tkachenko, A. G.; Xie, H.; Coleman, D.; Glomm, W.; Ryan, J.; Anderson, M. F.; Franzen, S.; Feldheim, D. L. J Am Chem Soc 2003, 125, (16), 4700-1.
[5] Tkachenko, A. G.; Xie, H.; Liu, Y.; Coleman, D.; Ryan, J.; Glomm, W. R.; Shipton, M. K.; Franzen, S.; Feldheim, D. L. Bioconjug Chem 2004, 15, (3), 482-90.
[6] Schmid, G. *Inorg. Syntheses* 1990, 7, 214.
[7] G. Schmid, N. K., L. Korste, U. Kreibig, D. Schönauer. *Polyhedron* 1988, 7, 605.
[8] G. Schmid, R. B., R. Pfeil, F. Bandermann, S. Meyer, G. H. M. Calis, J. W. A. van der Velden,. *Chem. Ber.* 1981, 114, 3634.
[9] J. Turkevitch, P. C. S., J. Hillier. *Discuss. Faraday Soc.* 1951, 11, 55.

Corresponding author:
M. Semmler-Behnke
Manuela.Behnke@gsf.de

Magnetism at Single Isolated Iron Atoms Implanted in Graphite

R. Sielemann[1], Y. Kobayashi[2], Y. Yoshida[3], H.P. Gunnlaugsson[4], G. Weyer[4]

■ 1 Helmholtz-Zentrum Berlin für Materialien und Energie ■ 2 Institute of Physical and Chemical Research (RIKEN), Japan ■ 3 Shizuoka Institute of Science and Technology, Japan ■ 4 Department of Physics and Astronomy, University of Aarhus, Denmark

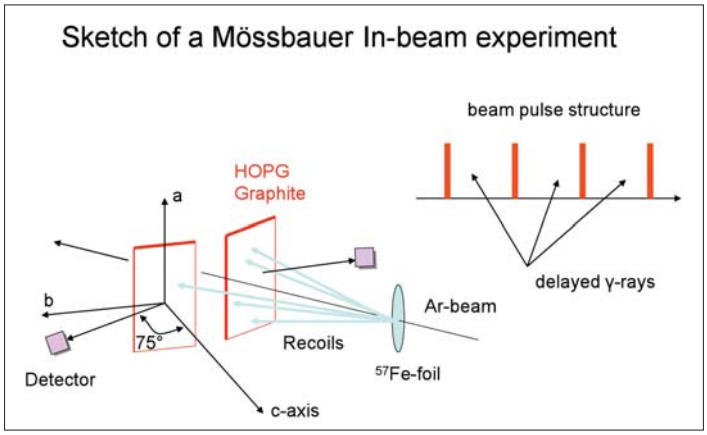

Fig. 1: Sketch of the 'In-Beam-Mössbauer-Spectroscopy' technique. A high energy Ar beam entering from the right excites and implants ^{57}Fe atoms into HOPG samples situated to the left and right of the beam. The principle of the pulsed beam is also shown.

Magnetism is caused by the spontaneous ordering of magnetic moments caused by some kind of exchange interaction. Typically, atoms with unfilled 3d or 4f shells are at the heart of magnetic materials. However, in the last two decades, organic materials have been found which, under certain conditions, might become magnetic by cooperation of electrons without the presence of the classical magnetic atoms. One particularly interesting material is carbon, in its various allotropic forms, for which indications of magnetic order have been reported in a number of recent publications [1]. This is surprising since carbon tends to form covalent bonds with spins usually paired. Amongst other explanations, defects and unusual structural modifications have been suspected of leading to magnetic structures [1].

We have performed experiments employing Mössbauer spectroscopy to study the geometric and electronic structure and possible atomic diffusion of implanted ^{57}Fe atoms in various carbon structures: diamond, fullerenes and graphite. Since Fe atoms are practically insoluble in these carbon structures a special technique for performing the Mössbauer effect was employed: In-Beam Mössbauer-Spectroscopy [2]. With this technique the ^{57}Fe atom is implanted at high energies (several MeV) and, at the same time, the Mössbauer active state is excited by Coulomb excitation without employing a radioactive precursor. In this way the whole experiment is performed on the 100 nanosecond timescale of the Mössbauer state and no clustering or out-diffusion of the Fe can occur; the concentration of ^{57}Fe atoms is extremely small at about 10^{-15} cm^{-3}. The salient feature of such implantation experiments is a high density of defects of about 1 at. % around the Mössbauer probe. Figure 1 shows a sketch of the technique.

The focus of this article is on experiments with graphite in different modifications. Highly-Oriented-Pyrolytic-Graphite (HOPG) material shows a Mössbauer spectrum with a number of lines grouped around zero velocity, which is typical for several implantation induced lattice sites. Surprisingly, part of the spectrum shows a six-line spectral component that is characteristic of a magnetic interaction at the position of the Fe probe atom for temperatures below 40 K (implantation and measuring temperature). The hyperfine field measured is 32.6 Tesla at 14 K, decreasing to 29.8 Tesla at around 40 K and, additionally, the spectrum shows a quadrupole splitting of 1.2 mm/s. Thus, it is clear that this field is not the field of iron metal as no clustering or segregation occurred. The HOPG material with the c-axis oriented perpendicular to the graphite planes allows the direction of the magnetic hyperfine field to be extracted parallel to the c-axis. A spectrum is shown in Figure 2.

The experiments were repeated in HOPG samples from different suppliers with comparable results. The lattice sites acquired in the implantation process cannot directly be inferred from the Mössbauer parameters; however, the isomer shift (electron density) of the magnetic component suggests that the atom is situated interstitially between two graphene sheets. On the other hand, experiments performed with polycrystalline material do not reveal any effects of magnetism, as shown in Figure 3.

It is of course surprising that a single Fe atom in graphite should be in a distinctly magnetic state. To check for possible magnetic impurities present in the samples, analytical experiments were performed by the ERDA (Elastic-Recoil-Detection-Analysis) technique before and after the implantation [3]. It turned out that the atomic concentration

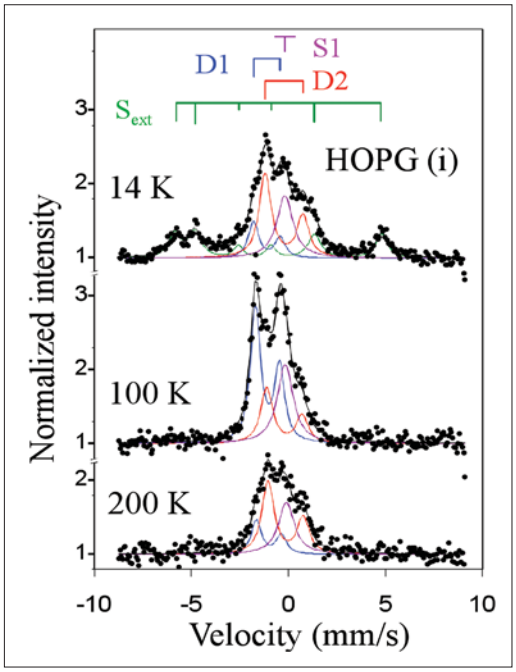

Fig. 2: Mössbauer spectra of ^{57}Fe atoms after implantation in HOPG graphite at the temperatures indicated. The spectra at 100 K and 200 K are fitted with 3 components S1, D1 and D2. Below 40 K, D1 starts converting into the magnetic state S_{ext}.

of all magnetic impurities (e.g. Fe) was smaller than 10^{-5} (before) and around 10^{-4} (after implantation), which is too small to directly produce magnetic effects. Hydrogen impurities amount to 10^{-3} (after implantation). However, the salient feature of the experiments is the large amount of defects, of about 1 at. % from the implantation cascades around the final ^{57}Fe lattice position. A defect density in this range was recently suggested to be sufficient to induce magnetic ordering in several oxides and also in graphite [4]. These calculations show that intrinsic defects (vacancies, interstitials) and certain impurity atoms (like hydrogen) carry magnetic moments and that a realistic exchange interaction may be found leading to magnetic ordering. Experimental evidence for magnetic order in graphite following proton irradiation was recently put forward by Esquinazi et al. [5].

In addition to or in combination with topological defects, the damage cascades of the implantation experiments will also introduce electronic disorder. Such disorder might lead to a mixture of sp^2- and sp^3-hybridized atoms cross-linking graphene layers and, under certain conditions, may constitute a spin system capable of forming an exchange-coupled ordered state. The coupling of ^{57}Fe to the topological and/or spin defects then appears as a possible mechanism to establish the observed magnetism. The fact that polycrystalline graphite does not show evidence for a magnetic state is not easily understood – it might be connected to the production process of the materials leading to different electronic properties. In our additional experiments, indications of magnetism have not been observed in either diamond or in the fullerenes.

The possibility that the spectrum is not a fully ordered state, but a paramagnetic state that is stably oriented in space by an exceptionally weak coupling to the lattice, can very likely be excluded from the measured temperature dependence of the hyperfine field strongly pointing to an interpretation in terms of magnetic ordering. However, since we observed the implanted state in a time window of 100 ns after the implantation process and the created defects are subject to thermal motion depending on the ambient temperature, this could in principle be a situation in which a metastable structure is observed. A relevant publication appeared recently by Sielemann et al.. [6].

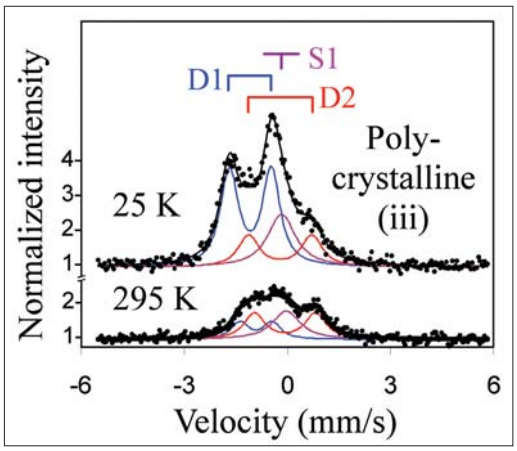

Fig. 3: Mössbauer spectra of ^{57}Fe after implantation in polycrystalline graphite.

[1] T.L. Makarova, Semiconductors 38, 615 (2004).
[2] R. Sielemann and Y. Yoshida, Hyperfine Interact. 68, 119 (1991).
[3] W. Bohne et al., Nucl. Instrum. Methods Phys. Res., Sect. B 136-138, 633 (1998).
[4] P.O. Lehtinen et al., Phys. Rev. Lett. 93, 187202 (2004).
[5] P. Esquinazi et al., Phys. Rev. Lett. 91, 227201 (2003).
[6] R. Sielemann et al., Phys. Rev. Lett. 101, 137206 (2008).

Corresponding author:
R. Sielemann
sielemann@helmholtz-berlin.de

Focusing solid state lens for neutrons

Roland Bartmann[1], Nicolas Behr[1], J. Füzi[2] and Thomas Krist[1]
■ 1 Helmholtz-Zentrum Berlin für Materialien und Energie (HZB), Glienicker Straße 100, 14107 Berlin
■ 2 Budapest Neutron Centre (BNC)

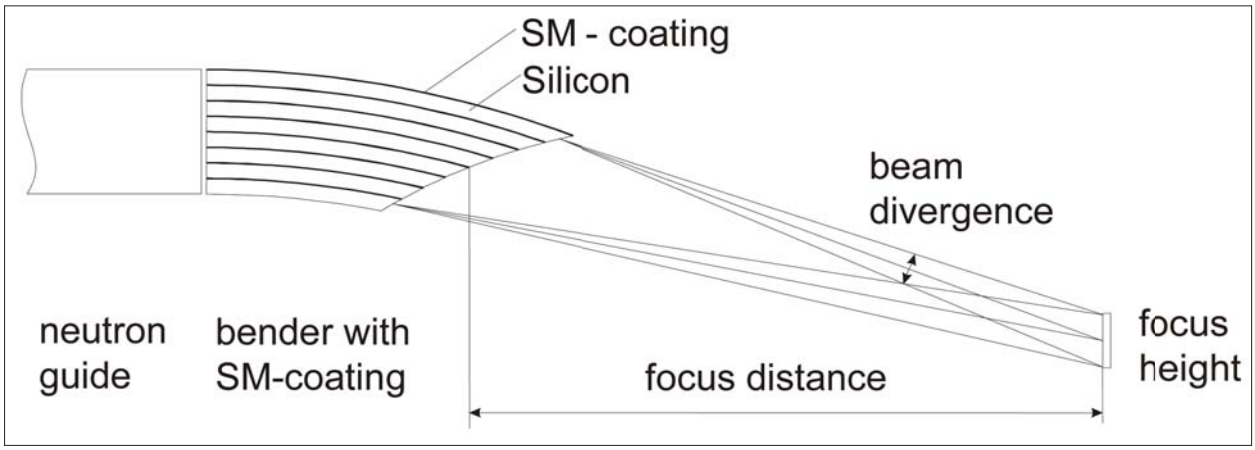

Fig. 1: Asymmetrical focusing lens composed of 100 pieces of 140×20×0.15 mm³ bent silicon wafer with a coating of Ni-Ti supermirrors with m=2. Focus distance 36mm, gain factor 3.4.

In neutron experiments there is always a demand for higher neutron flux at the sample. During the last few years, there has been intensive research in the field of focusing neutrons using refractive lenses, focusing guides, solid state devices, magnetic fields etc.

Given our long experience in building solid state devices we decided to develop a solid state focusing lens. The concept is based on an old idea of Mildner's [1], which was never implemented. It uses a set of curved silicon wafers of different lengths which are coated with reflecting supermirrors. The wafers work as thin guides in which the neutrons follow the curvature of the wafer by means of zigzag or garland reflections. The neutrons are deflected by different total angles depending on the length of the wafers. Since the longer wafers are further away from the beam axis the neutrons travelling in them are more strongly deflected. The curvature and length of the wafers are chosen so that all neutrons meet at a focus a few cm behind the lens. This system accepts the full divergence of a neutron guide if the wafers have the same coating as the guide. Of course, according to Liouville's theorem of

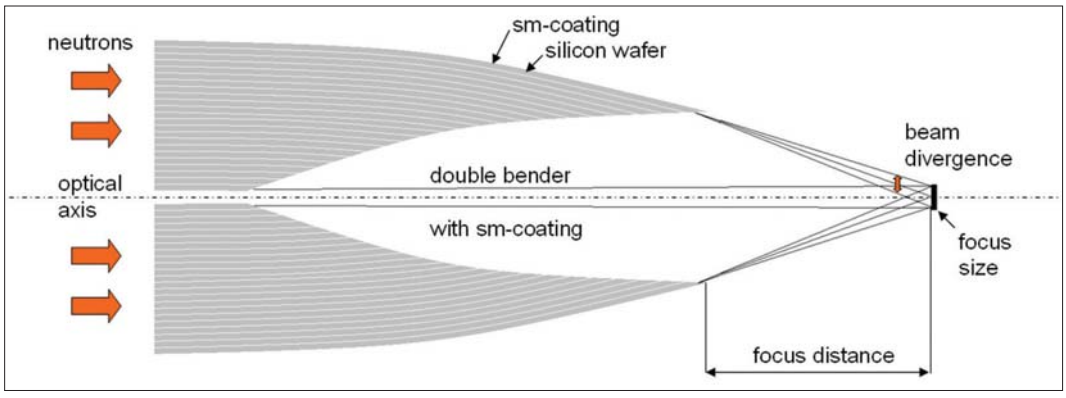

Fig. 2: Symmetrical focusing lens composed of 2×95 pieces of 140×20×0.15 mm³ bent silicon wafer with a coating of Ni-Ti supermirrors with m=2. Focus distance 31mm, gain factor 5.6.

constant phase space density, the increase in intensity in the focus is accompanied by an increase of divergence.

A similar system which also uses thin silicon wafers was built by Johnson and Daymond [2]. However, in this system, neutrons emerging from a point source are refocused to a point focus. However, our system deflects the beam from a guide onto a focal point. As a first step we created such a device consisting of 100 wafers. They were coated by the Budapest group with Ni-Ti supermirrors with m=2, where m gives the ratio of the critical angle of the supermirror to that of nickel. The wafers were bent into a circular shape (Figure 1). This lens was measured with a neutron beam at a wavelength of 4.7Å on the mirror test device V14 at Helmholtz-Zentrum Berlin (HZB). It showed a maximum intensity gain in the focus of 3.4 compared to the direct beam intensity at this position without the lens. The focus was a one dimensional line focus with FWHM of 2.4 mm [3].

The second step was to improve the lens design by using two wafer stacks in a symmetrical arrangement. Each stack consisted of 95 silicon wafers with the dimensions of $140\times20\times0.15$ mm^3 (Figure 2). The lens was measured at V14 and also at the Neutron Tomography Station V7 at HZB, which has a two dimensional photo sensitive detector with submillimetre spatial resolution. The neutron wavelengths were 4.7Å at V14 and 5Å at V7. At V14 a gain of 4.6 [4] and at V7 a gain of 5.6 [5] were measured in the focal maximum. The focus occurred 35mm behind the end of the lens (Figures 3 and 4). This gain implies that more than 40% of all neutrons entering the 31×20 mm^2 entrance window of the lens are focused into the 2.4×20 mm^2 focal line. The remaining neutrons are lost due to attenuation in the silicon and the limited reflectivity of the supermirrors. Measurements at 44 mm and 85 mm behind the focus show a nearly continuous broadening without sharp peaks.

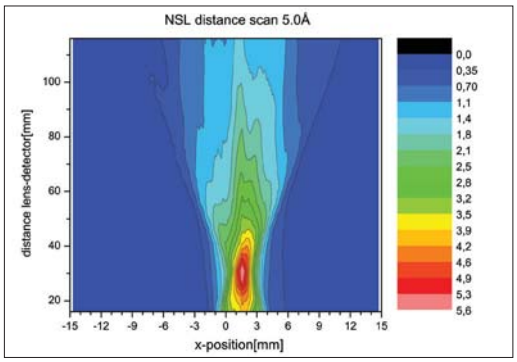

Fig. 4: Contour plot of the intensity gain distribution around the focal spot of the double-sided lens.

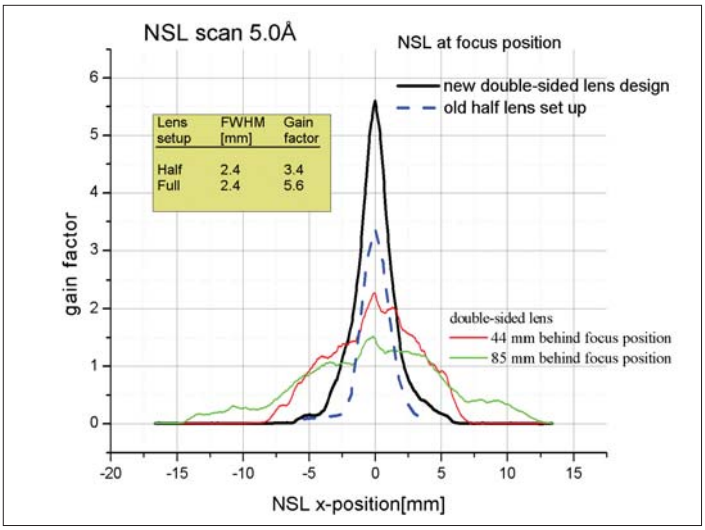

Fig. 3: Gain factor for the symmetric (full lines) and asymmetric (hatched line) lens. The red and green graph give the gain factor at 44 mm and 85 mm behind the focus.

Currently, experiments are underway to show the practical use of the lens in a reflectometer where being able to increase intensity by a factor of 5.6 would be a great advantage.

[1] D.F.R. Mildner: The neutron microguide as a probe for materials analysis, NIM A299 (1990) 416-419.
[2] M.W.Johnson, M.R. Daymond: The neutron silicon lens: a new lens design for thermal neutrons, Physica B283 (2000) 308-313.
[3] Th. Krist, N. Behr, J.-E. Hoffmann: Focusing lens and polarising supermirror, BENSC Experimental Reports 2005.
[4] R. Bartmann, A. Stellmacher, Th. Krist: Improved focusing lens and Nickel/Titanium monochromator, BENSC Experimental Reports 2007.
[5] R. Bartmann, A. Hilger, N. Kardjilov, Th. Krist: Double-sided focusing solid state lens, BENSC Experimental Reports 2007.

Corresponding author:
Thomas Krist
krist@helmholtz-berlin.de

Thermodynamics of the spin Luttinger-liquid in a model ladder material – an example for complementary measurements at LaMMB

K. Kiefer[1] , Ch. Rüegg[2], B. Thielemann[3], D. F. McMorrow[2], D. Biner[4], K. W. Krämer[4]

■ 1 Helmholtz-Zentrum Berlin für Materialien und Energie GmbH, BENSC

■ 2 London Centre for Nanotechnology and Department of Physics and Astronomy, University College London, London WC1E 6BT, United Kingdom

■ 3 Laboratory for Neutron Scattering, ETH Zurich and Paul Scherrer Institut, CH-5232 Villigen, Switzerland

■ 4 Department of Chemistry and Biochemistry, Universität Bern, CH-3000 Bern 9, Switzerland

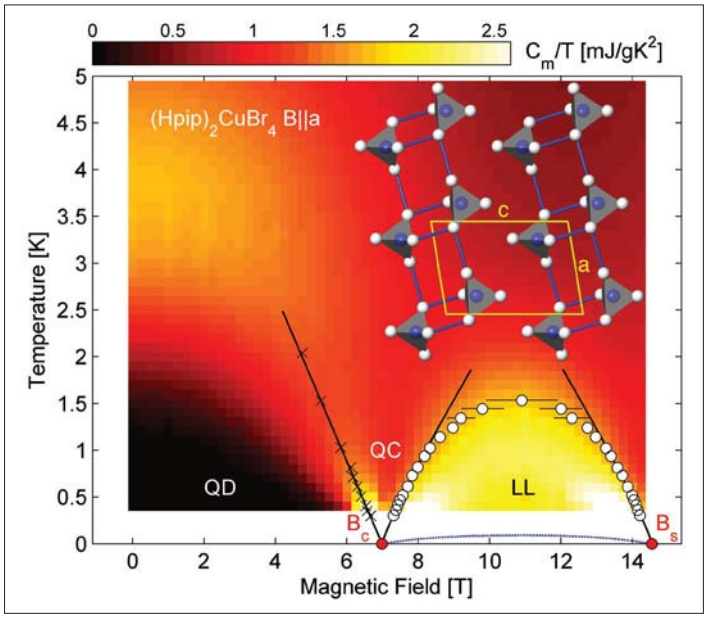

Fig. 1: Field-temperature phase diagram of the spin-ladder compound $(Hpip)CuBr_4$, showing quantum disordered (QD), quantum critical (QC), and spin Luttinger-liquid (LL) phases. The contour plot shows the magnetic specific heat capacity as $C_m(T,B)/T$. Local maxima from the reduction of the triplet gap by the Zeeman effect are indicated by crosses. Circles denote the LL crossover based on measurements of the magnetocaloric effect [Figure 2], black lines are fits to extract the critical fields. The blue line indicates the onset of 3D long-range order below 100 mK [Ref. 3]. Inset: lattice structure of $(Hpip)CuBr_4$ in projection along the b-axis, with Cu atoms blue and Br white.

Quantum spin systems display a remarkable diversity of fascinating physical behaviour such as Bose-Einstein condensation, quantum critical scaling or the Luttinger-liquid regime. One especially interesting model system is the spin ½ two-leg antiferromagnetic ladder, where two quantum phase transitions and the Luttinger-liquid regime can be observed. A quantum phase transition is a phase transition at zero temperature which is driven by an external parameter like, for example, the magnetic field. Unlike a "classical" phase transition where thermal fluctuations play a crucial role, a quantum phase transition is driven by quantum fluctuations. In a spin ½ two-leg antiferromagnetic ladder two quantum phase transitions are to be expected, one from the gapped, dimerised ground state to the Luttiger-liquid regime, and a second from the Luttinger-liquid regime to a field aligned ferromagnetic phase.

However, materials in which to explore such effects are rather rare. Here we present the results of thermodynamic measurements on an exceptional spin ½ two-leg ladder material, the metal-organic compound piperidinium copper bromide $(C_5H_{12}N)_2CuBr_4$, abbreviated as $(Hpip)CuBr_4$ [Ref. 1]. This material is exceptional for two reasons. On the one hand, the complete phase diagram can be explored experimentally with standard laboratory techniques; for this material the critical fields for the two quantum phase transitions are B_c=6.99(5) T and B_s=14.4(1) T. On the other hand, $(Hpip)CuBr_4$ is a nearly perfect representation of a one dimensional spin ½ two-leg ladder with very weak inter-ladder exchange interaction, as determined by inelastic neutron scattering. The exchange interactions are J_{rung}=12.9(2) K and J_{leg}=3.3(3) K with an inter-ladder exchange interaction of J'<100mK [Ref. 2].

In order to explore the phase diagram of (Hpip) CuBr4, heat capacity and magnetocaloric effect measurements were performed on the instrument CM-14.5T of the Laboratory for Magnetic Measurements at BENSC (LaMMB). In Figure 1 the different phases in the phase diagram are identified where a colour plot of the heat capacity divided by the temperature is shown. The most prominent feature is the yellow dome of the Luttinger-liquid regime, where the heat capacity C displays a linear behaviour with temperature T so

that C/T is constant. This behaviour is expected for a Luttinger-liquid. At low magnetic fields and low temperatures the heat capacity decreases exponentially with temperature, revealing the gapped spectrum spectrum of the magnetic excitations.

The white circles in Figure 1 denote the crossover to the Luttinger-liquid regime based on measurements of the magnetocaloric effect. The special technique used at LaMMB for the very accurate determination of the Luttinger-liquid regime boundary is the quantitative quasi-isothermal magnetocaloric effect. With this powerful method it is possible to directly determine the temperature derivative of the magnetisation $\partial M/\partial T|_B$, via the relationship $\partial M/\partial T|_B = -(\delta Q/\delta B)/T$, where δQ is the heat generated in the sample by the magnetocaloric effect at a magnetic field change δB. As the magnetisation M *vs.* temperature T is expected to pass an extremum (maximum or minimum) at the crossover to the Luttinger-liquid regime [Ref. 4], the zero-transition of $\partial M/\partial T|_B$ *vs.*T is indicative of the boundary of the Luttinger-liquid regime. In Figure 2(a) the measured magnetocaloric effect $(\delta Q/\delta B)/T$ is shown for different temperatures. In Figure 2(b) the crossover to the Luttinger-liquid regime is marked by the zero-transition of the magnetocaloric effect (white circles). By the quantitative measurement of the magnetocaloric effect it was possible to detect the Luttinger-liquid regime in a very effective and precise way.

The measured heat capacity data have been compared with numerical calculations of the heat capacity of an ideal spin ½ two-leg antiferromagnetic ladder [Ref. 2]. The measured and calculated heat capacities agree almost perfectly. This agreement reveals again that $(Hpip)CuBr_4$ represents an exceptional model compound for a spin ½ two-leg antiferromagnetic ladder. Hence the material offers unprecedented opportunities to investigate the intrinsic physics of low dimensional quantum systems.

The identification of $(Hpip)CuBr_4$ as an ideal model substance shows the power of combining neutron scattering experiments (partially performed on the BENSC instrument V2) with complementary laboratory-based measurement techniques. This combination of complementary methods was the key for the successful completion of this project.

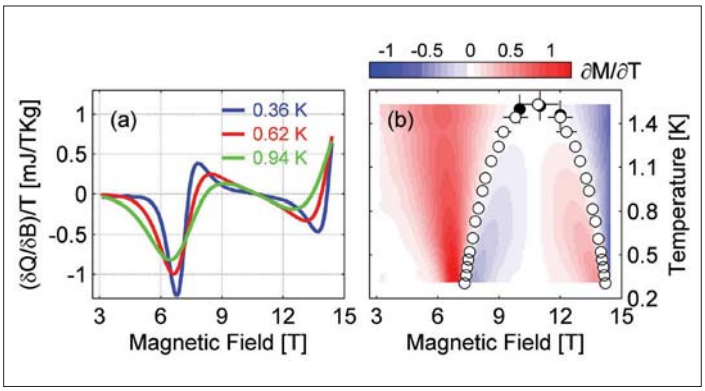

Fig. 2: Magnetocaloric effect in $(Hpip)CuBr_4$. (a) Heat flow δQ to and from the sample as a function of magnetic field divided by temperature, $(\delta Q/\delta B)/T$. (b) Contour plot of $\partial M/\partial T|_B$ as a function of field and temperature. White circles denote the crossover derived from $\partial M/\partial T=0$, while black circles are maxima in the specific heat capacity, obtained at fixed field.

[1] B. C. Watson, V. N. Kotov, M.W. Meisel, D.W. Hall, G. E. Granroth, W. T. Montfrooij, S. E. Nagler, D.A Jensen, R. Backov, M.A. Petruska, G. E. Fanucci, and D. R. Talham, Phys. Rev. Lett. 86, 5168 (2001)

[2] Ch. Rüegg, K. Kiefer, B. Thielemann, D. F. McMorrow, V. Zapf, B. Normand, N. B. Zvonarev, P. Bouillot, C. Kollath, T. Giamarchi, S. Capponi, D. Poilblanc, D. Biner, and K. W. Krämer, Phys. Rev. Letters, Vol. 101, 247202 (2008)

[3] B. Thielemann, Ch. Rüegg, K. Kiefer, B. H. M. Rønnow, B. Normand, P. Bouillot, C. Kollath, E. Orignac, R. Citro, T. Giamarchi, A. M. Läuchli, D. Biner, K. Krämer, F. Wolff–Fabris, V. Zapf, M. Jaime, J. Stahn, N. B. Christensen, B. Grenier, D. F. McMorrow, and J. Mesot, Phys. Rev. B Vol. 79, 020408(R) (2009).

[4] X. Wang and L. Yu, Phys. Rev. Lett. 84, 5399 (2000)

Corresponding author:
K. Kiefer
klaus.kiefer@helmholtz-berlin.de

Dark-field tomography

M. Strobl[1,2], A. Hilger[2], N. Kardjilov[2], I. Manke[2], C. Grünzweig[3], C. David[3], F. Pfeiffer[3]
■ 1 Universität Heidelberg, Germany, ■ 2 SF1/SF3, Helmholtz-Zentrum Berlin für Materialien und Energie, Berlin, Germany, ■ 3 Paul Scherrer Institut, Villingen, Switzerland

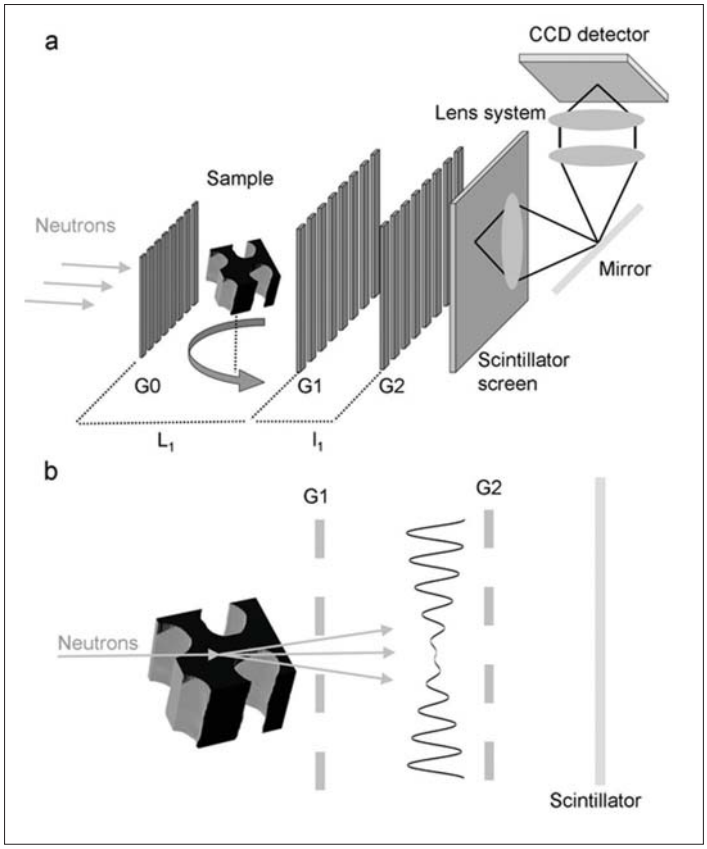

Fig. 1: Grating interferometer (a) Set-up with three gratings, sample and detector system. (b) The visibility of the interference degrades due to ultra-small angle scattering in the sample.

For the last decade, since neutron imaging has been able to profit from digital image recording, it has not only experienced an outstanding gain in importance and applications but also in methodical and technical developments. Besides significant increases in spatial and temporal resolution, new methods are able to address more than the attenuation coefficient conventionally used in order to achieve image contrast and volumetric information about the inner structure of a sample. This means that refractive index distribution, microcrystalline phase and texture, mesoscopic structures causing small-angle scattering, as well as magnetic fields and structures now provide image contrast and can be identified with three-dimensional resolution. The corresponding methods used are phase contrast imaging, energy-resolved imaging at Bragg edges, dark-field (i.e. small-angle scattering) contrast and polarised neutron imaging.

However, some of these methods suffer from severe limitations, such as low flux densities, which hinder their practical application or, in many cases, concerning tomographic application. For phase contrast imaging a grating-based shearing interferometer has been developed recently at Paul Scherrer Institut (PSI). It can be employed to perform differential phase contrast tomographies on reasonable time scales in order to achieve three dimensional reconstructions of the refractive index distribution of a sample [1].

The grating-based shearing interferometer shown in Figure 1 consists of a source grating G0, a phase grating G1 and an analyser absorption grating G2. The absorption source grating with a period p_0 provides a partially coherent beam at the phase grating G1, inducing a phase shift of π with a period of p_1. The analyser grating with a period $p_2 = p_1/2$ at the 1st fractional Talbot distance enables the detection of the interference pattern despite a detector resolution that is at least an order of magnitude too low to resolve the period of the intensity oscillations. A phase stepping approach is applied to resolve the fringe pattern by

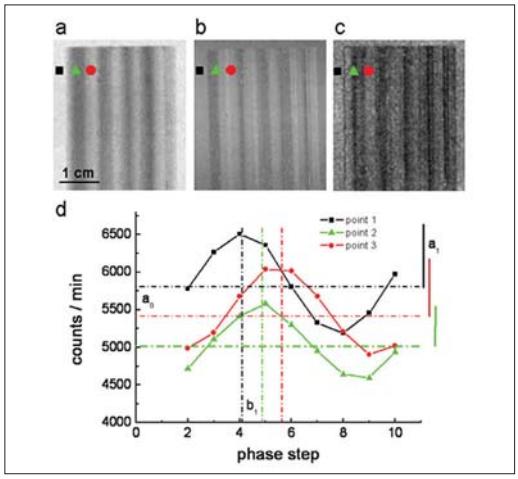

Fig. 2: Radiographic images of an Al sample by (a) attenuation contrast a_0, (b) the differential phase contrast b_1 and (c) the dark-field image a_1. (d) Measured instrumental response function $I = a_0 + a_1 * \cos(b_1)$ for three different image points.

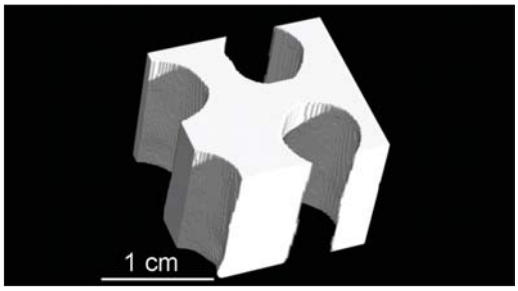

Fig.3: Detail of three dimensional reconstruction of Al sample matrix as derived for each of the three contrast parameters.

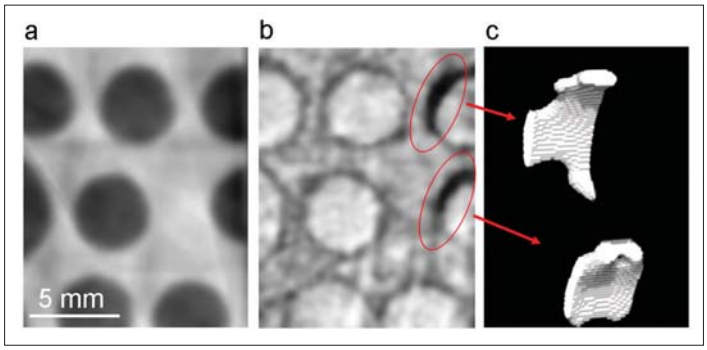

Fig.4: Detail of reconstructed sample cross section in (a) differential phase contrast and (b) dark-field contrast. (c) Extracted three dimensional tomographic reconstruction of sediments found in the dark field contrast images.

recording several images for different scan positions of, for example, the analyser grating. In this way spatial and angular resolution are decoupled and consequently differential phase effects, i.e. refraction, can be detected in spite of relaxed coherence conditions. Analysing the phase shifts of the fringes and the mean intensity over one fringe period for a tomographic measurement provides volumetric reconstructions of the real and the imaginary part (attenuation) of the refractive index distribution.

The novel approach used here is to exploit another parameter for tomography by taking advantage of the grating interferometer. In contrast to differential phase effects, scattering at very small angles does not cause a shift in one direction, but a broadening of the angular intensity distribution [2]. Consequently, it causes a spatial broadening of the maxima of the fringe pattern in the grating interferometer. Indeed, this broadening of the maxima at constant periodic positions reduces the visibility of the fringe pattern (Figure 2). Hence the spatially resolved relative visibility, i.e., the variation of the local amplitude of the fringe pattern is a scattering-related imaging parameter analogous to dark-field imaging or ultra-small angle scattering contrast. The efficiency of this technique means the field of applications can be opened up to include three-dimensional tomographic investigations. Tomographic reconstructions become possible by the extraction of the scattering-induced contribution to the visibility degradation [3] and the formulation of a related Radon transformation. Such Radon tranformation is based on a path integral describing the angular contribution of (multiple) scattering from the sample to the beam divergence, as demonstrated by Strobl et al. [2].

For this purpose a grating interferometer was installed at the CONRAD neutron imaging facility and a reference sample was measured. The tomographic data recorded yielded three dimensional spatially resolved reconstructions of the attenuation coefficient, the real part of the refractive index and the novel dark-field scatter parameter. Although, in this case, all of the contrast signals equivalently recovered the structure of the Al sample matrix (Figure 3), one feature was not displayed in any of them. In some channels of the matrix small sediments could be identified in the dark field reconstruction due to strong scattering at small angles (Figure 4). Since then, the method has been applied successfully to identify, for example, structural inhomogeneities in different Al-Si binary metallic alloys.

Generally, ultra small-angle scattering based reconstructions derived from dark-field images are particularly useful for identifying inhomogeneities caused by structures in objects ranging from about a hundred nanometres to a few micrometres. This range naturally complements the size range that can be spatially resolved by imaging methods. In contrast to the existing crystal analyser-based methods this novel approach allows for three-dimensional dark-field computer tomography on practical time scales. Additionally, the results demonstrate how the tomographic dark-field contrast approach can be applied even at low-brilliant sources, such as state-of-the-art neutron sources or laboratory based x-ray sources. Applications of radiographic dark-field contrast with x-rays have already been reported in various fields, such as medical imaging, food inspection, industrial non-destructive testing and security screening, to name but a few.

[1] F. Pfeiffer et al., Phys. Rev. Lett. 96, 215505 (2006)
[2] M. Strobl et al., Appl. Phys. Lett. 85, 3, 488 (2004)
[3] M. Strobl et al., Phys. Rev. Lett. 101, 123902 (2008)

Corresponding author:
Markus Strobl
strobl@helmholtz-berlin.de

Hydrogen storage in ice

Margarita Russina[1], Ewout Kemner[1], Milva Celli[2], Lorenzo Ulivi[2], Ferenc Mezei[3]
■ 1 Helmholtz-Zentrum Berlin für Materialien und Energie, Berlin, Germany ■ 2 Istituto dei Sistemi Complessi, Sesto Fiorentino Italy ■ 3 SZFKI, Budapest, Hungary

Clathrate hydrates are inclusion compounds, formed by a network of hydrogen-bonded water molecules that are stabilised by the presence of foreign molecules. The hydrophobic interactions between the host framework and guest molecules push the ice to change its structure and form cages of different form and dimensions in order to accommodate the guests. The topology of the ice cages depends on the sizes and shapes of the guest molecules, the typical dimensions of the cages range between 4 - 15Å. The confinement and small size of the cages strongly influence the behaviour of the guest molecules and result in properties that are different from those of the bulk, thus making the clathrate hydrates model system useful in the study of the effects of confinement.

The interest in clathrate hydrates was motivated by their potential as cheap and environmentally friendly energy storage carriers. The synthesis of the hydrogen filled ice clathrates was reported in 2002 by W. Mao [1]. By application of 2000 bar hydrogen pressure she was able to form fully hydrogenated clathrates which are stable up to 160 K under atmospheric pressure and can hold hydrogen at up to 3.77% of the total mass. It has been found that loading pressure can be decreased (to about 300 bar) and the temperature stability can be improved (up to 270 K) by the introduction of large organic molecules into part of the cages of the H_2-clathrates [2].

To discover the reason for these differences we undertook a detailed study of the guest-host interactions using a combined neutron scattering and molecular simulation approach. Guest-host interactions are best reflected in the microscopic dynamics, thus the benefits and complementary nature of neutron scattering and molecular dynamics simulations are obvious: both techniques provide information on atomic trajectories allowing for direct comparison of the theoretical and experimental results. Both methods work with full efficiency on the scale of a few nanometres in length (which is relevant for hydrogen storage structures) and can follow atomic motions on a broad time scale from 10^{-14} to 10^{-10} s.

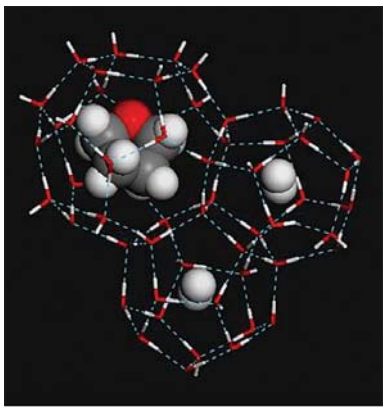

Fig. 1: Structure of ice-based clathrates with small and large cages. Colour coding: red indicates oxygen atoms; grey, hydrogen and dark grey, carbon atoms. The large cage shown in the picture is occupied by a tetrahydrofuran molecule, whilst small cages are occupied by one H_2 molecule each. Note that in H_2-H_2O clathrates, large cages are occupied by two H_2 molecules.

The experimental part of the work has been undertaken using the TOF spectrometer NEAT at the Berlin Neutron Scattering Centre. We investigated the behaviour of molecular hydrogen in the bulk and also confined into cages of ice-based clathrates of differing dimensions. For this purpose we used the composite THF - H_2O - H_2 and H_2O - H_2 systems (THF; tetrahydrofuran). The structure of the H_2 filled ice-clathrates consist from 16 small cavities in the shape of pentagonal dodecahedron (5^{12}) and 8 large cavities in the shape of hexakaidecahedron ($5^{12}6^4$). In the ternary clathrate the THF molecules take up places in the larger cages and the molecular hydrogen only occupies smaller cages (those with an accessible diameter of 5.02Å), with one molecule per cage. In the fully hydrogenated H_2O - H_2 system, hydrogen can occupy both the small and the large cages. These larger cages are of a 6.67Å accessible diameter and accommodate two H_2 molecules per cage (Figure 1).

The scattering function of hydrogen molecules is described by a discrete spectrum of rotational and vibrational levels [3]. The energies of rotational levels are given by $E_{rot}=J(J+1)B$, where $J=1,2,3,\ldots$ and the rotational component is B=7.35 meV. The vibrational levels are given by $E_{vib}=(\nu+ ½)\hbar\omega_{vib}$ with the vibrational constant ω_{vib}=516 meV. The measurements were taken at temperatures in the 2-100 K range.

In the energy range explored on NEAT, the dynamic response of the bulk hydrogen, shows one single peak corresponding to the first rotational transition at 14.7meV. The response changes once the hydrogen is confined to the cages. The first rotational transition splits into three components indicating the anistropic cage environment, the rather weak, Van-der-Walls type interactions between H2 and the ice framework. The splitting in the large cages is greater than that in the small cages indicating the higher anisotropy of the large cages.

However, the surprising feature is that in addition to the first rotational transition, we observed a new additional dynamic feature in 8-12 meV energy

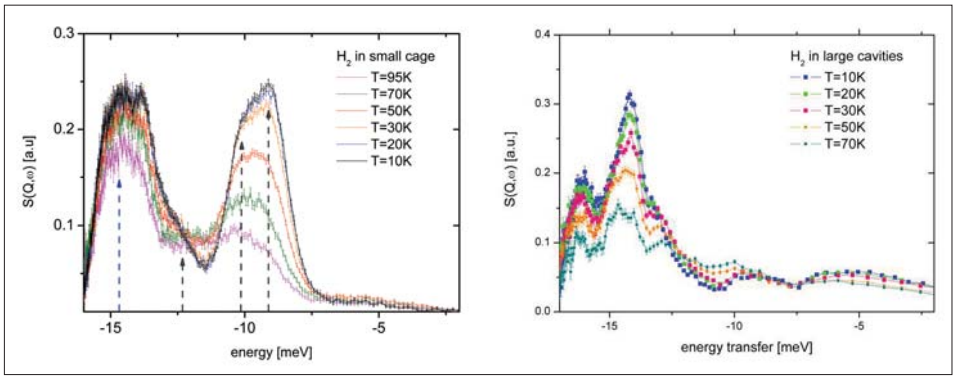

Fig. 2: Dynamic structure factor of hydrogen in small (a) and large (b) cages measured by TOF spectrometer NEAT. Dashed lines indicate the position of first rotational transition in the bulk H2 (black line) and additional modes observed only in the small cage (grey line).

range consisting of several components (Figure 2a). The positions of the peaks are temperature dependent but in different ways: whilst some components soften with increasing temperature, the others exhibit strong anharmonic behaviour and move to the higher frequencies. It is remarkable that such a dynamic response is absent when the hydrogen is placed into the large cages (Figure 2b). Considering that the guest – host cage wall interactions in both cages are of the same nature, it must be the effect of the confinement dimensions that gives rise to this additional dynamic feature.

To verify whether the translational motion of hydrogen molecules inside the cages contributes to the observed excess of density of states (DOS), we performed a series of molecular dynamic simulations. For these simulations we used the Materials Studio and VASP programme suites. The Materials Studio Discover programme was used to perform classical molecular dynamics simulations on hydrogen inside clathrate hydrate stabilised with tetrahydrofuran, using Compass force-field and Ewald summation for both Van der Waals and Coulomb interactions. We simulated the behaviour of 8 unit cells for times of up to 1 ns at various temperatures, using a time-step of 1 fs. VASP was used for ab-initio quantum-mechanical molecular dynamics, where only one primitive cell of the clathrate on the Dirac cluster was simulated at various temperatures and with different hydrogen loadings, for 4 ps using a time-step of 1 fs. Using the nMoldyn programme suite, the dynamic structure factor $S(Q,\omega)$ has been calculated from Materials Studio and VASP trajectories and compared directly with our experimental results.

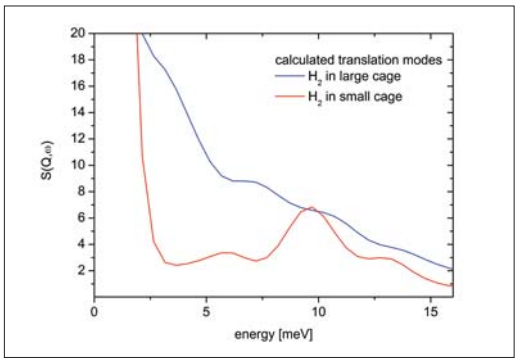

Fig. 3: Dynamic structure factor calculated by WASP software package for translation motion in hydrogen confined in clathrate cages.

The results of molecular dynamics studies are shown in Figure 3. The calculated $S(Q,\omega)$ shows that in the small cage a translation motion (rattling) in the 8-12 meV energy range occurs. The rattling modes shift to low frequencies and become less pronounced when the dimensions of the cage are increased. These are the exact tendencies that we observed in our experiments. It should be noted that the available molecular dynamics tools cannot demonstrate the internal dynamics of the hydrogen molecule, including the rotational motion.

However, the translational motion alone cannot explain the difference between the intensities observed in the small and large cages. Considering the amount of hydrogen in the cages and the numbers of cages in the structure, the intensity of the rattling modes should be about the same in both cages. The excess of DOS observed for hydrogen in the small cages must have an additional dynamic origin. At these temperatures and beyond the translational motion, only the molecular rotation is excited and can contribute to the $S(Q,\omega)$. The energies of rotational and translation dynamics are fairly similar and the coupling between these two modes can lead to a new, hybrid type motion. On the one hand, this can explain the observed excess DOS. On the other hand, the onset of the hybrid motion reflects strong coupling between modes and thus is expected to decrease the kinetic energy of the confined molecular hydrogen. This in turn increases its effective “attachment” to the framework (cage walls) and thus increases the temperature-pressure stability of the entire H_2 clathrate system.

[1] W.Mao, Science 297 (2002) p. 2247
[2] H. Lee et al., Nature 434, 743 (2005)
[3] J.U.Young and J.A. Koppel, Phys. Rev.135A,603 (1964)

Corresponding author:
Margarita Russina
margarita.russina@helmholtz-berlin.de

Does a chiral spin liquid skyrmion phase exist?

C. Pappas[1], E. Lelièvre-Berna[2], P. Falus[2], P. Fouquet[2], B. Farago[2], P. Bentley[1,2], E. Moskvin[1,3] and S. Grigoriev[3]
■ 1 Helmholtz-Zentrum Berlin für Materialien und Energie, Berlin, Germany
■ 2 Institut Laue-Langevin, 6 rue Jules Horowitz, 38042 Grenoble, France
■ 3 PNPI, 188300 Gatchina, Leningrad District, Russia

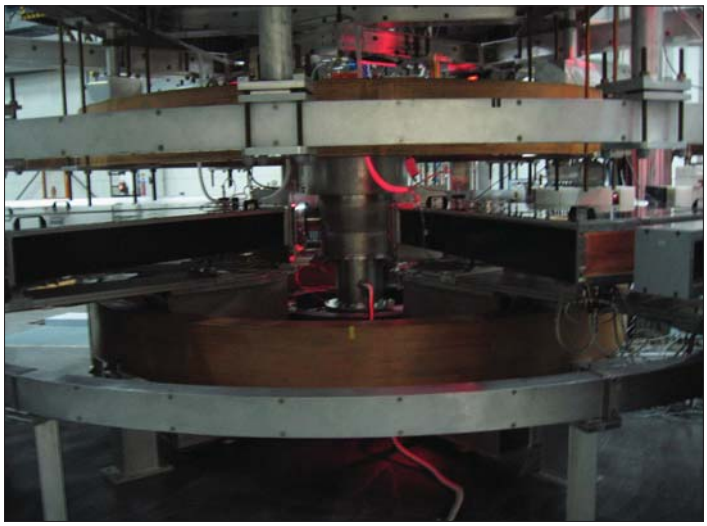

Fig. 1: Photograph of the first realisation of a polarimetric NSE set-up, a combination of Cryopad (at the centre) with the Neutron Spin Echo spectrometer SPAN.

Chirality is ubiquitous in nature and on the microscopic level is of fundamental importance in our everyday life. It is also an essential ingredient for the appearance of countable soliton-like quasi-particles in continuous fields, which bridge the gap between waves and particles in the wave-particle duality concept. These were introduced in the early 1960s by Skyrme [1] and have, until now, been identified in semiconductors under high magnetic fields or in the blue phases of liquid crystals. Chiral interactions may also lead to a spontaneous formation of skyrmions, even in perfect ferromagnetic crystals without any structural defects or external magnetic fields [2]. The condition for the emergence of this novel ground state of condensed matter is a hierarchy of energy scales in the Hamiltonian, which is realised with the reference itinerant-electron ferromagnet MnSi. In MnSi the strongest exchange interaction aligns the spins ferromagnetically and the weaker chiral Dzyaloshinskii-Moriya $(\vec{M} \times (\vec{\nabla} \times \vec{M}))$ term twists the spins into a helix, due to the lack of inversion symmetry of the B20 ($P\,2_13$) lattice structure. Additionally, the weakest Anisotropic Exchange (AE) or crystal field term pins the helix propagation vector $\vec{\tau}$ long the <111> crystallographic directions. The helical order appears below the weak first order transition at $T_C \sim 29$ K with a single-domain, left-handed helix of period ~175 Å ($|\vec{\tau}| \sim 0.036$ Å^{-1}) and all magnetic moments perpendicular to the helix propagation vector.

The rigorous analysis of chirality and chiral fluctuations at the helical transition has required the development of the new technique: polarimetric Neutron Spin Echo spectroscopy, which combines the high energy resolution of Neutron Spin Echo (NSE) with the polarisation analysis capabilities of Cryopad. NSE uses the Larmor precession of polarised neutrons in a magnetic field to directly access the energy transfer at the sample and reaches the highest energy resolution in neutron spectroscopy (< 1 neV). The neutron beam polarisation may be seen as a classical vector in the laboratory but only the component along a quantisation axis (magnetic field) can be measured. A rotation by $\pi/2$, as may occur due to the chiral term in MnSi, will not be distinguished from a depolarisation unless the quantisation axis is not defined at the sample. These Spherical Neutron Polarimetry (SNP) or simply polarimetric measurements are enabled by Cryopad, which shields the magnetic field down to ~0.1 μT and controls the incoming and scattered beam polarisation vectors at the borders of the zero field area, with an accuracy greater than 0.5 degrees.

The Polarimetric NSE method was developed at SPAN (Hahn-Meitner-Institut) (Figure 1) and then implemented at IN15 (Institut Laue-Langevin). The first order helical transition of MnSi is seen by the jump of neutron intensity at the <111> helical reflection (Figure 2a) and corresponds to the sharp peak of the specific heat found by Stishov et al. [5]. These specific heat results are reproduced in Figure 2c. The SNP measurements were performed with an incident beam polarisation as high as 97 % K (Figure 2b) and confirm the stabilisation of a single-domain, left-handed helix at low temperatures. However, this is unaffected by the first order transition and remains unchanged up to $T_{C'} \sim T_C$+1.2 K, the temperature of a broad specific heat maximum. Figure 2 illustrates the existence of two transitions in MnSi.

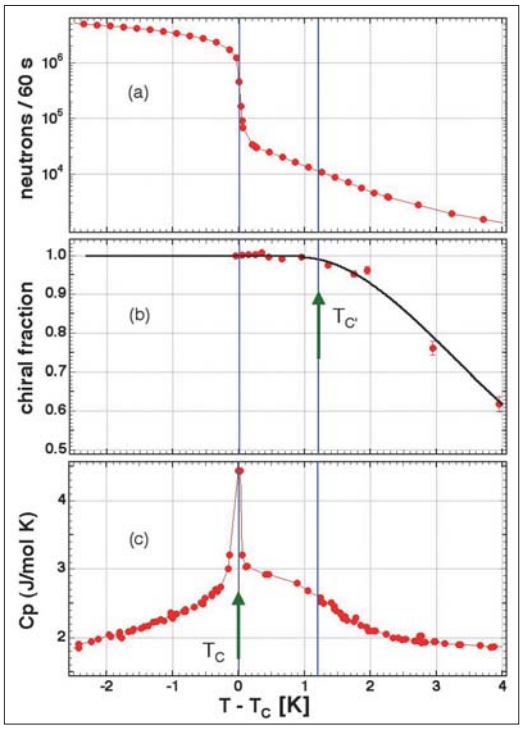

Fig. 2: Temperature dependence of (a) the intensity of the helical peak and (b) the chiral ratio of the dominant left-handed domain. In (b) the red circles are calculated from the extinction of the chiral intensity when the polarisation vector is parallel to the helix propagation vector and the blue squares are deduced from the $\pi/2$ rotation of the polarisation vector (incident vector perpendicular to the helix propagation vector). The specific heat results of Stishov et al. [5] are given in (c). For the sake of comparison the data are plotted against $T\text{-}T_C$, where T_C is determined by the jump in neutron intensity and the peak of the specific heat respectively.

The first order transition to a long range order is seen on the helical peak intensity and the peak due to the specific heat is seen at T_C. The spin liquid state above the helical phase is completely single-handed without any sign of disorder. It is an amorphous skyrmion phase, which exists between T_C and $T_{C'}$ and has strong similarities with nematic liquid crystals.

The dynamic or static nature of this new phase was unravelled by Neutron Spin Echo spectroscopy. The spectra in Figure 3 show exponential relaxations superimposed on an elastic contribution due to the Bragg peak, which were 'fitted' using the function $I(q,t) = a\ \exp(-t/\tau_o) + (1-a)$. The characteristic time τ_o does not change with temperature but the elastic fraction $(1-a)$ evolves from ~20% to 100% within 0.2 K and is very similar to the rapid increase in the intensity seen in Figure 1a and masking the decay of $I(Q,t)$ at T_C.

The amorphous skyrmion phase is completely dynamic and the fluctuations coexist with the helical long range order at T_C. An extensive analysis of the relaxation seen by NSE excludes any interaction between fluctuations and the first order helical transition. Also, high resolution Larmor diffraction experiments do not show any structural deformation at the helical transition [6]. Therefore, the first order transition must be attributed to the different textures between the skyrmion and the helical phases. It is remarkable that chirality, specific heat and the NSE spectra give consistent results. This evidences the existence of this completely chiral single domain but dynamically disordered novel state of matter, which appears in a very narrow temperature range of ~1.2 K above the helical phase of MnSi.

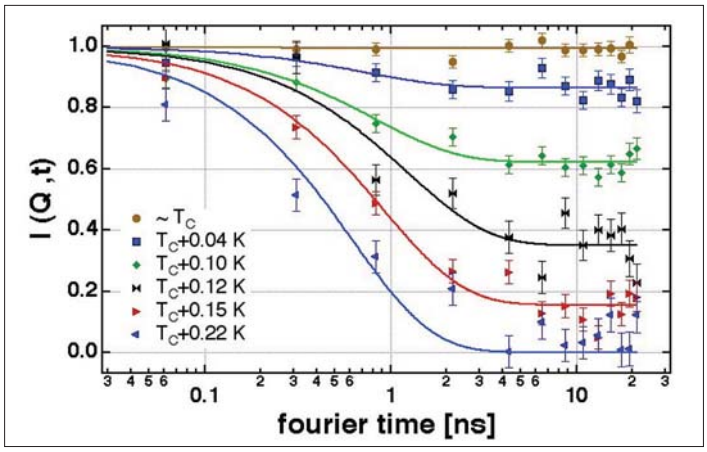

Fig. 3: Polarimetric NSE spectra measured on IN15 with a wavelength of 9 Å for the incoming polarisation vector $\vec{P}'$ perpendicular to the helix propagation vector $\vec{\tau}$ and to the scattering vector $\vec{Q}$. In this case the helix rotates the polarisation by $\pi/2$ and the scattered polarisation vector $\vec{P}$ is parallel to $\vec{\tau}$ and $\vec{Q}$. Such a measurement is only possible in polarimetric NSE configuration.

[1] T.H. Skyrme, Proc. R. Soc. Lond. Ser. A, 260 (1961) 127
[2] U. K. Rößler, A.N. Bogdanov and C. Pfleiderer, Nature 442 (2006) 797
[3] C. Pfleiderer, D. Reznik, L. Pintschovius, H. von Lohneysen, M. Garst, and A. Rosch, Nature 427 (2004) 227
[4] S. V. Grigoriev et al, Phys. Rev. B 72 (2005) 134420
[5] S. M. Stishov et al., Phys. Rev. B 76 (2007) 052405 and S. M. Stishov et al., J. Phys.: Condens. Matter 20 (2008) 235222
[6] C. Pfleiderer, P. Böni, T. Keller, U. K. Rößler, and A. Rosch, Science 316, 1871 (2007).

Corresponding author:
C. Pappas
pappas@helmholtz-berlin.de

Fractional magnetisation plateaus in the Shastry Sutherland magnet TmB_4

K. Siemensmeyer[1], E. Wulf1, H.-J. Mikeska[2], K. Flachbart[3], S. Gabani[3], S. Matas[3], P. Priputen[3], E. Efidokimova[4], N. Shitsevalova[4]

■ 1 Helmholtz-Zentrum Berlin, Glienicker Str. 100, D 14109 Berlin ■ 2 Institut für theoretische Physik, Universität Hannover, D 30167 Hannover ■ 3 Institute of Experimental Physics, Slovak Academy of Science, SK 04001 Kosice, Slovakia ■ 4 Institute for Problems of Material Science, Ukraine Academy of Science, UA 03680 Kiev, Ukraine

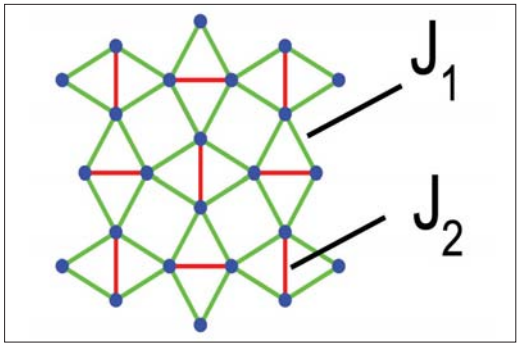

Fig. 1: The position of rare earth ions in the tetragonal plane. The diagonal bonds (red) and the square bonds (green) are almost identical in length, leading to an almost identical exchange path J_1 and J_2.

For decades, the magnetism on geometrically frustrated lattices has fascinated scientists, and numerous, initially exotic and now familiar phenomena have been found. For example, the magnetic order on the triangular and Kagóme lattice in two dimensions (2D), and more recently, the well known pyrochlore structure in 3D, where frustration leads to ferromagnetism and to the emergence of topological magnetic monopoles. Less familiar is a 2D lattice first suggested by Shastry and Sutherland (SS) [1]. It is a square lattice where interactions along the sides of the square and through every second square diagonal are assumed (Figure 1). Interestingly, SS could show that for antiferromagnetic (af) interactions on the sides and dominant af interaction on the diagonals, an af spin dimer is formed that condenses into a dimer spin liquid state.

Reports on this lattice are scarce. To date, the compound $SrCu(BO_3)_2$ has produced most of the knowledge on the properties of such a lattice. Most surprising is the observation of fractional magnetisation plateaus in $SrCu(BO_3)_2$, which was not predicted by the theory [2,3]. The specific explanations for this observation are still subject to debate, presumably because the critical fields for

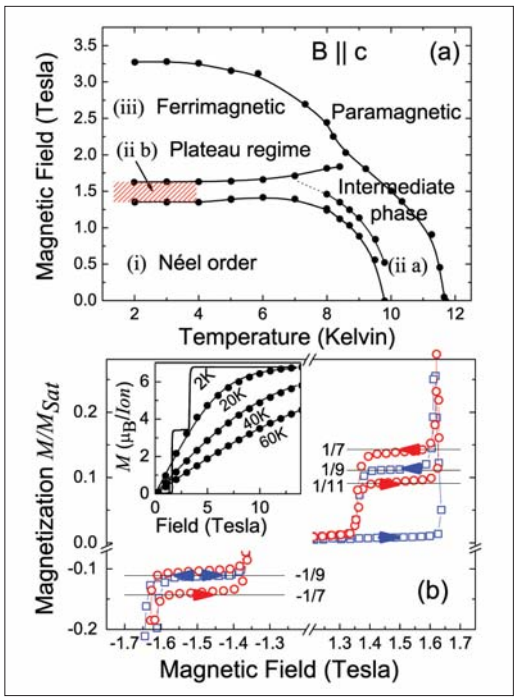

Fig. 2: (a) Phase diagram of TmB_4 as derived from magnetisation data for B || (001) (full symbols). (b) Magnetisation at T = 2K (open squares) and T = 3K (open circles). The arrows indicate the direction of the field change. The inset in (b) gives an overview of high field; the lines are measured data and full circles are calculated using a high temperature approximation.

$SrCu(BO_3)_2$ are beyond those available for scattering experiments and are focused on an analogy with the fractional quantum Hall effect of a 2D fermion gas [4].

Recently, we have investigated another class of SS magnets formed by a series of rare earth tetraborides – REB_4 [5]. The geometry of the REB_4 lattice can be mapped to a SS lattice. In general, the magnetisation data show that these materials are highly anisotropic magnetic metals. Out of a series of compounds investigated by us (RE=Tb, Er, Ho, Tm), it transpired that TmB_4 shows fractional

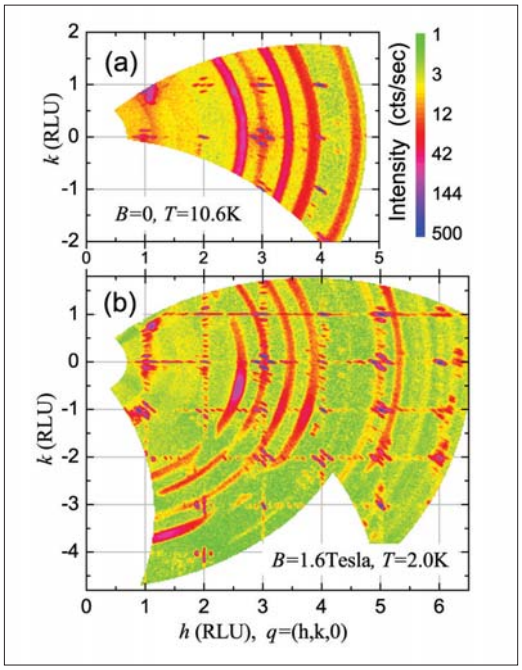

Fig. 3: (a) and (b) show the neutron diffraction pattern in the tetragonal plane for the intermediate and the plateau phase respectively. The figures share the intensity colour code given in (a). The reflections can be indexed based on fractions of 1/7, 2/7… and 1/9, 2/9… . The powder lines are generated by the aluminium of the cryogenic equipment used for the neutron diffraction experiments.

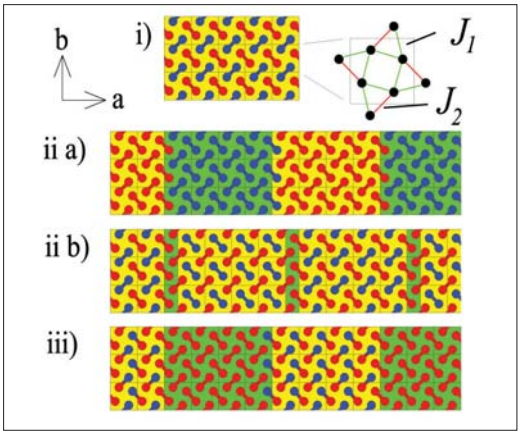

Fig. 4: The magnetic structure of TmB_4 for a magnetic domain along the a⁻ direction in the tetragonal plane. Red or blue circles denote up or down Ising moments. The labels (i) to (iii) refer to the phase identification in Figure 2(a). In (i) the position of the Tm_{3+} ions within the tetragonal plane is expanded for one unit cell, with the SS-bonds marked in red.

magnetisation plateaus as a function of the external field at values of M/M_{sat}= *1/7, 1/8, 1/9, 1/11…* . It shows af order and is dominated by a strong Ising anisotropy. The phase diagram (Figure 2) reveals four different regimes. A low temperature zero field phase is separated from the paramagnetic phase by another af ordered phase. In high field the order is ferrimagnetic with M/M_{sat} = ½. The zero field phase and the ferrimagnetic phase are separated by a regime where fractional magnetisation values are observed at low temperature.

The critical temperatures and magnetic fields of TmB_4 are experimentally easy to access, in contrast to the $SrCu(BO_3)_2$. This provided the first opportunity to study the magnetic structures on an SS - lattice using neutron diffraction (Figure 3). In the zero field low temperature phase, the moments of the dimer pairs are ferromagnetically (fm) aligned, though the coupling between dimers is af (c.f. Figure 4). The high temperature, zero field phase shows regions with fm dimer coupling, and the direction of the fm alignment alternates on a length scale of 8 unit cells. The fractional states form similar structures where stripes of fm phase slips – like domain walls – are added. They lead to the observed fractional magnetisation. Finally, the ferrimagnetic phase consists of stripes of fm and af dimer order with a periodicity of 8 unit cells. Interestingly, in the "af" stripe, the magnetic moments of a dimer pair are af.

Our data could possibly be explained by the RKKY interaction that is believed to be the dominant interaction in metallic REB_4 compounds. This, however, is not satisfactory because more specific interaction ratios are required to explain the structures in the various phases, in particular in the fractional regime. For the similar compound $SrCu(BO_3)_2$, a Hofstadter treatment [6] analogous to the fractional quantum Hall effect has been proposed [4] and this provides a much more natural approach to explain the magnetism in TmB_4. Consequently, we speculate that TmB_4 is a magnetic analogue to a spinless 2D fermion gas in a strong field. In that material class TmB_4 would be the first example that is fully accessible to experimental studies.

[1] B. S. Shastry and B. Sutherland, Physica 108B, 1069 (1981).
[2] H. Kageyama et al., Phys. Rev. Lett. 82, 3168 (1999).
[3] K. Kodama et al., Science 298, 395 (2002).
[4] S. E. Sebastian et al., e-print Phys. Rev. Lett. 101, 177201 (2008)
[5] K. Siemensmeyer et al., Phys. Rev. Lett. (2008).
[6] D. R. Hofstadter, Phys. Rev. B 14, 2239 (1976).

Corresponding author:
Konrad Siemensmeyer
siemensmeyer@helmholtz-berlin.de

From the bronze to the iron age of superconductivity

D.N. Argyriou*, S.A.J. Kimber*, Karel Prokes and Fabiano Yokaichiya*
■ Helmholtz-Zentrum Berlin für Materialen und Energie, *Novel Materials Group, Department SF-2.

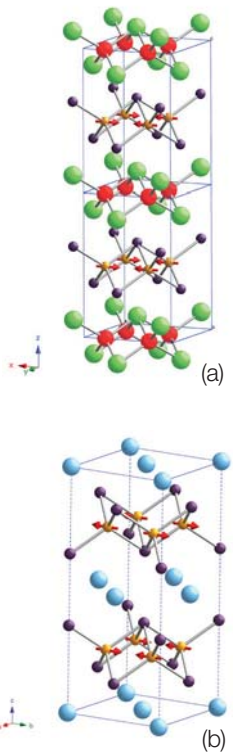

1986 was a seminal year in physics. Karl Müller and Johannes Bednorz in their lab in Zurich discovered that a particular copper oxide showed superconductivity at T_C=35 K, a temperature that was almost 12 K higher than any other known superconductor at the time[1] . This discovery indicated that superconducting T_Cs can be pushed from a few Kelvin to an unprecedented 140 K. Although there is still much debate on the exact mechanism that drives superconductivity in copper oxides, what is increasingly clear is that the magnetic moment of the copper ions provides a major component of the glue between electrons that forms Cooper pairs and produces superconductivity. So, if copper with its magnetic interactions is good for superconductivity, then why not other magnetic transition metals, too, such as Fe, Co, Ni or Mn? Recently, there was a discovery in hydrated $NaCoO_2$ compounds that yielded superconductivity with a relatively low T_c of 5 K[2]. However, interest in this material was brushed aside at the beginning of 2008 by the discovery that compounds that have iron arsenide layers show superconductivity as high as 55 K[3] (see Fig. 1). The field has developed very rapidly since then, with the discovery of a host of layered materials that have FeAs, FeSe and NiP layers that show superconductivity, and all in the space of a few months!

Fig. 1: Crystal structures of the FeAs superconductors. In this type of superconducting materials the FeAs layer is made of edge shared $FeAs_4$ tetrahedra, that are separated either by a REO (rare earth) layer as in the case of the so-called "1111" family (a) or a divalent cation as in the case of the "122" family (b).

Why so much interest in a 55 K superconductor? Firstly, superconductivity in these iron arsenide compounds is more isotropic (in-plane versus out-of-plane) than the copper oxides which are notorious for their high anisotropy and the technological problems it presents. Therefore, the high T_C and lower anisotropy of the iron arsenides open up huge potential for technological applications. Secondly, magnetism may also be important for achieving superconductivity as the iron arsenides form another class of materials that allow the investigation of magnetically-mediated Cooper pairing. It turns out that on the one hand, there are great similarities to the behaviour of copper oxides, while on the other, there are dramatic differences. Like the copper oxides, the (undoped) parent compounds are also antiferromagnets, and chemical doping with hole charges suppresses long range magnetic order and yields superconductivity. Unlike the undoped magnetic copper oxides that are Mott insulators, the iron arsenides are metals in their undoped magnetic state. Another marked difference that has changed the way we think about superconductivity in these materials, is that applying pressure on the magnetic parent compound itself yields superconductivity at almost the same value of T_C as we obtain by chemical doping. This effect has never been observed in the copper oxides. The effect of pressure is most pronounced in the 122 family of compounds AFe_2As_2 (see Fig. 1), where T_C for A=Ca is 12 K at 5 kbar and up to 38K at 50 kbar for A=Ba.

At HZB we have investigated the development of magnetism in iron arsenide parent compounds and the effects of pressure on the crystal and magnetic structure in close collaboration with the Leibniz-Institut für Festkörper- und Werkstoffforschung, Dresden, and the Ames Lab. in the USA. We first looked at PrFeAsO. The structure of this compound consists of layers of PrO and FeAs as shown in Fig.1. Using neutron powder diffraction we showed that both the Fe and the Pr spins order long range and beyond this, a magnetic coupling between these two atoms leads to an unusual negative thermal expansion along the *c*-axis on cooling[4]. The magnetic structure we established for Fe is also shown in Fig.1 and confirms much of the initial calculation of magnetic order[5].

Our work with pressure has focused on the 122 family of compounds aided by small single crystals. Here we found that as we apply pressure on $CaFe_2As_2$ and the material becomes a superconductor above 3 kbar[6], at the same time the crystalline lattice collapses in volume by 5%, while all evidence of ordered magnetism disappears from the neutron diffraction data[7]. This exciting result suggests that the changes to the lattice are intimately linked to the changes in magnetic and electronic degrees of freedom. At ambient pressure we established that the high temperature tetragonal phase (T) discontinuously changes to an orthorhombic phase (O) exactly at the magnetic transition[8]. The ordering of Fe-spins in 122 is the same as in the 1111 type of compounds (see Fig. 1). Us-

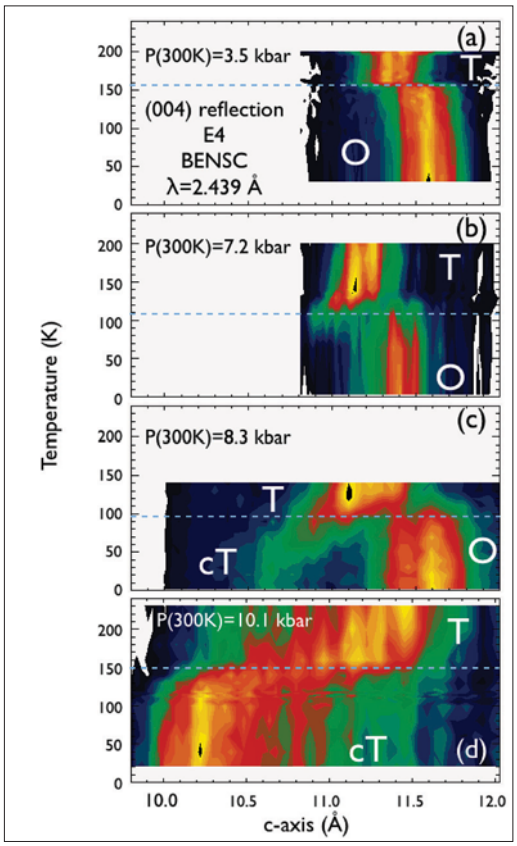

Fig. 2: Temperature dependent neutron diffraction measurements at various initial pressures, collected on the E4 diffractometer from a 10 mg $CaFe_2As_2$ single crystal inside a clamped pressure cell. Here we show measurements of the (004) reflection. The data are represented as two dimensional colour plots with intensity shown as colour.

ing the double axis diffractometer E4 at BENSC we were able to follow the structural and magnetic transitions as a function of pressure and temperature as our $CaFe_2As_2$ single crystal was driven into the superconducting state. In Fig. 2, we show the (004) reflection as a function of temperature measured in a clamped pressure cell on E4. Here, on cooling, the pressure changes by ~2 kbar from 300 to 2K from the initial pressure set ex situ (P(300K)). At low pressures we observe the same T-O transition as we find at ambient pressure indicated by a small discontinuous expansion of the c-axis (Fig. 2(a-b)). However, at high pressure we can observe the new collapsed tetragonal (cT) phase that hosts superconductivity. Here the *c*-axis shrinks abruptly by 1Å, a change of almost 10% in the c-axis (Fig. 2(d)). But with intermediate pressure we find evidence of co-existence between the O and cT phases (Fig. 2(c)) that may help explain observations of co-existence between magnetism and superconductivity. Using the same measurements and others with our collaborators we also probed the magnetic order and found that it abruptly disappears as we enter the cT phase. Our results show that the effect of chemical doping on long range magnetism resembles that of pressure.

Our results firmly establish the iron arsenides as a different class of superconductors from copper oxides, despite their similarities. In this new iron age of superconductivity we have more than one way of tuning the lattice to produce superconductivity: chemical doping and pressure. This flexibility allows us to probe the changes in the electronic and crystal structure cleanly with pressure and without the local distortions that unavoidably develop when using chemical doping. Even if it turns out that magnetic fluctuations aid Cooper pairing to produce superconductivity, the way these fluctuations are tuned to optimum values in the iron arsenides is quite different from that in copper oxides. It is still the dawn of this new iron age in superconductivity and there is much more to learn. What is certain is that the results obtained so far are unexpected and exciting and promise to keep us busy for years to come.

[1] J. G. Bednorz and K. A. Müller Z. Physik, B 64, 189 (1986).
[2] K. Takada, et al. Nature 422, 53 (2003).
[3] Y. Kamihara, T. Watanabe, M. Hirano, and H. Hosono. J Am Chem Soc 130, 3296 (2008); Ren Zhi-An, LU Wei, Yang Jie, Yi Wei, Shen Xiao-Li, Li Zheng-Cai, Che Guang-Can, Dong Xiao-Li, Sun Li-Ling, Zhou Fang, Zhao Zhong-Xian. Chinese Phys Lett 25, 2215 (2008).
[4] S.A.J. Kimber, D. N. Argyriou, F. Yokaichiya, K. Habicht, S. Gerischer, T. Hansen, T. Chatterji, R. Klingeler, C. Hess, G. Behr, A. Kondrat, and B. Büchner. Phys. Rev. B 78, 140503 (2008).
[5] T. Yildirim, Phys Rev Lett 101, 057010 (2008).
[6] M. Torikachvili, Sergey L. Bud'ko, Ni Ni, and Paul C. Canfield. Phys Rev Lett 101, 057006 (2008).
[7] A. Kreyssig, M. A. Green, Y. Lee, G. D. Samolyuk, P. Zajdel, J. W. Lynn, S. L. Bud'ko, M. S. Torikachvili, N. Ni, S. Nandi, J. Leão, S. J. Poulton, D. N. Argyriou, B. N. Harmon, P. C. Canfield, R. J. McQueeney and A. I. Goldman. Phys Rev B (in press). arXiv:0807.3032.
[8] A. I. Goldman, D. N. Argyriou, B. Ouladdiaf, T. Chatterji, A. Kreyssig, S. Nandi, N. Ni, S. L. Bud'ko, P. C. Canfield and R. J. McQueeney. Phys. Rev. B 78, 100506 (2008).

Corresponding author:
Dimitri Argyriou
argyriou@helmholtz-berlin.de

Antiferromagnetic order in thin films with atomic layer resolution

E. Schierle[1,2], A. Gottberg[2], W. Söllinger[3], W. Heiss[3], G. Springholz[3], G. Kaindl[2] and E. Weschke[1,2]

■ 1 Helmholtz-Zentrum Berlin für Materialien und Energie, Berlin, Germany ■ 2 Institute of Experimental Physics, Freie Universität Berlin, Berlin, Germany ■ 3 Institute of Semiconductor Physics, Johannes Kepler Universität, Linz, Austria

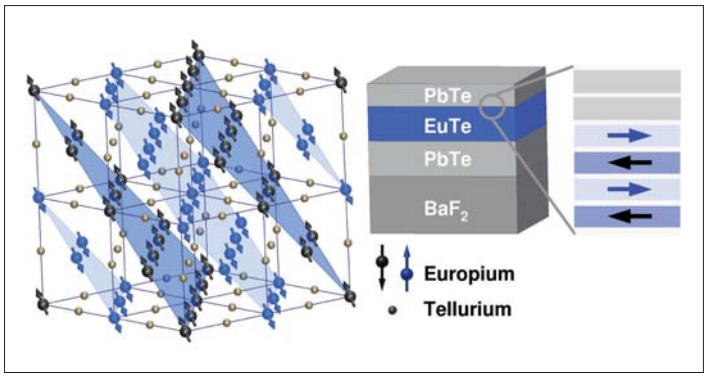

Fig. 1: Magnetic structure of EuTe with antiferromagnetic stacking of ferromagnetic (111) planes along the diagonal of the cubic crystal structure. Thin film samples are grown on PbTe buffer layers on BaF_2 substrates with the [111] direction perpendicular to the film surface.

In the vicinity of surfaces and interfaces, magnetic order and its thermal evolution may deviate from bulk behaviour [1]. A well-known example employed in current magnetic thin film devices is the exchange bias effect, where the hysteresis loop of a ferromagnet is shifted in the presence of the interface to an antiferromagnet. The understanding of such phenomena requires a detailed knowledge of the local magnetic structure, particularly as a function of the distance from the interface. While scanning probe techniques can readily provide lateral magnetic images on an atomic scale, a depth-dependent characterisation of magnetic structures with the same resolution remains a challenging task. Nuclear techniques are well suited to studying local magnetic properties but require the insertion of probe isotopes into the material. Magnetic scattering techniques are also applicable; however, they usually suffer from the weakness of the signal that is obtained from the few atomic layers of a thin film.

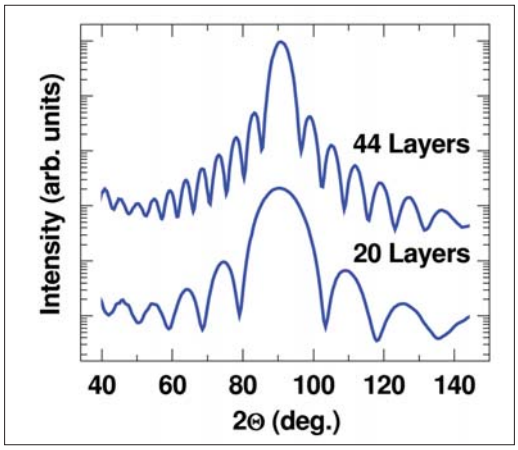

Fig. 2: The (½ ½ ½) magnetic Bragg peak obtained from EuTe films by resonant magnetic soft x-ray diffraction. The smaller number of scattering layers of the thinner film is observed in the diffraction patterns as a broadening of the main peak and shifts of the side maxima.

With the advent of third-generation synchrotron radiation sources, a magnetic x-ray scattering technique has become available. By tuning the photon energy to a core-electron excitation, resonance can increase the magnetic x-ray scattering length substantially. The effect is huge at the $M_{4,5}$ edges of the lanthanide elements, and the magnetic x-ray scattering by a single lanthanide ion can be as large as conventional charge scattering from 200 electrons [2]. The $M_{4,5}$ edges cover the soft x-ray range between 900 eV and 1500 eV. These photon energies are provided by the UE46 beamline of Helmholtz-Zentrum Berlin at BESSY II [3], an instrument that is ideally suited for this type of studies.

In the present investigation, the atomic-layer resolved magnetisation profile of an antiferromagnetic thin film was obtained for the first time [4]. This was achieved with a thin film of the magnetic semiconductor europium telluride (EuTe), which allowed exploitation of the high sensitivity at the M5 resonance. EuTe is a prototype Heisenberg system that was studied extensively as bulk material. It crystallises in the cubic rock salt structure (Figure 1). The (111) planes are ferromagnetically ordered, with antiferromagnetic stacking along the [111] direction. Along this direction, the magnetic unit cell is twice as large as the chemical unit cell, and a (½ ½ ½) magnetic Bragg peak is

observed. Single EuTe (111) films, sandwiched between lead telluride (PbTe), were prepared with very high crystalline quality by molecular beam epitaxy [5]. With the photon energy tuned to the Eu-M_5 resonance (1127.5 eV), the magnetic (½ ½ ½) reflection could be recorded with unprecedented quality: peak count rates were larger than 10^8 photons/sec with signal-to-background ratios of more than 1000. This allowed a detailed study of peak shapes and intensities as a function of temperature even close to the ordering temperature of 12.8 K.

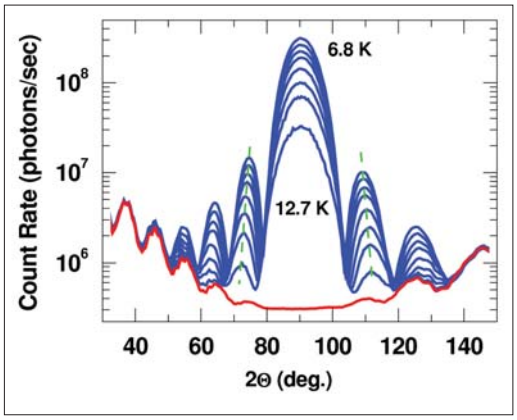

Fig. 3: Magnetic diffraction patterns obtained from the 20-layer film at various temperatures. Note the shift of the side maxima due to a decreasing mean number of magnetic layers with increasing temperature.

The sensitivity of the magnetic diffraction patterns is illustrated in Figure 2. With a finite number of scattering planes, the diffraction pattern of a 44-layer thick film exhibits pronounced side maxima, known as Laue oscillations. For 20 layers, the pattern is strongly broadened with side maxima shifted away from the main peak. An analogous result is well known from basic wave optics: the width of the diffraction signal of a slit is inversely proportional to its width (corresponding to the film thickness in our case). The same phenomenon, albeit in a more subtle manner is observed for the 20 layer film upon increasing the temperature (Figure 3): the shift of the side maxima indicates a reduction of the mean number of magnetically ordered layers as the ordering temperature is approached. By using a large number of data sets for various temperatures, this can be worked out in more detail by a rigorous simultaneous analysis. As a result, the magnetisation of each individual layer of the film is obtained as a function of temperature (Figure 4). At the lowest temperature, a rather sharp profile is observed, essentially all layers are fully magnetised. With

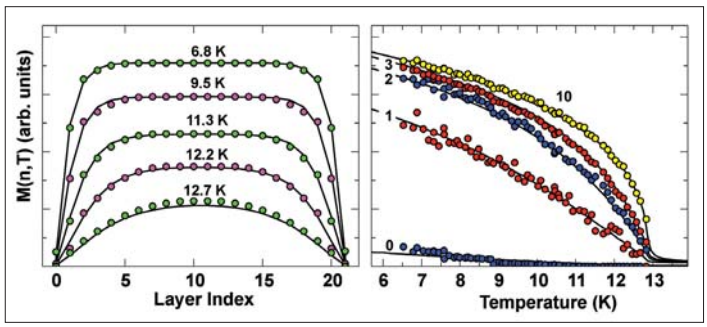

Fig. 4: Layer-resolved magnetisation in a EuTe film of 20 atomic layers as obtained from resonant magnetic soft x-ray diffraction. Left: Magnetisation profiles for various temperatures. In the layers close to the interfaces, the magnetisation is strongly reduced. Right: Temperature dependences of selected layers. The inner layer (10) behaves in a bulk like manner, while strong deviations are observed for the outer layers (0-3) as theoretically predicted [1]. The solid lines represent the result of Monte-Carlo calculations [4].

increasing temperature, the profiles become increasingly rounded, which is due to the reduced exchange energy at the EuTe/PbTe interfaces that leads to a faster decrease in the magnetisation in this region. Consequently, the temperature dependence of the magnetisation exhibits a clear variation across the film. The behaviour of the inner layer is comparable to that of bulk EuTe, while strong deviations are observed for layers in the vicinity of the interface.

These results not only corroborate theoretical predictions experimentally [1], but also pave the way for diffraction studies of magnetic ordering at surfaces and interfaces with very high depth resolution. Furthermore, the method is applicable to more subtle ordering phenomena, such as charge and orbital ordering that can be seen in transition metal oxides by resonant x-ray diffraction [6].

[1] K. Binder and P. C. Hohenberg, Phys. Rev. B 9, 2194 (1974).
[2] H. Ott et al., Phys. Rev. B 74, 094412 (2006).
[3] U. Englisch et al., Nucl. Instr. and Meth. Phys. Res. A 467- 468, Part 1, 541 (2001).
[4] E. Schierle et al., Phys. Rev. Lett. (almost accepted).
[5] N. Frank, G. Springholz, and G. Bauer, Phys. Rev. Lett. 73, 2236 (1994).
[6] P. Abbamonte et al., Nature 431, 1078 (2004).

Corresponding author:
E. Schierle
enrico.schierle@helmholtz-berlin.de

Spin-polarized neutron imaging

Nikolay Kardjilov, Ingo Manke, Markus Strobl, André Hilger, Martin Dawson, John Banhart
■ **Helmholtz-Zentrum Berlin für Materialien und Energie, Berlin, Germany**

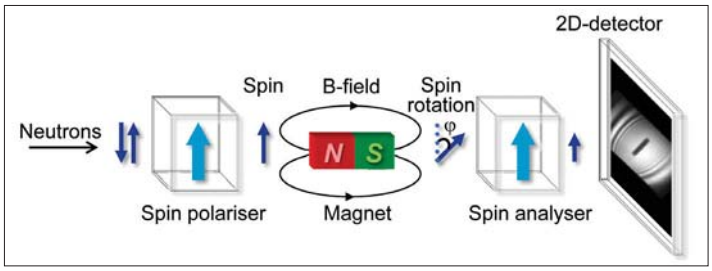

Fig. 1: Schematic diagram of the set-up used for imaging magnetic materials on CONRAD. The neutron beam is polarized, allowed to precess around a magnetic field, analyzed, and then detected. Note how the intensity (dark blue arrow) behind the analyzer is smaller than the intensity behind the polarizer. [1]

Introduction

Conventional approaches for imaging magnetic fields are limited to investigating the surface of a sample and the free space around it; the observation of the spatial distribution of magnetic fields within a bulk sample is not possible. In order to overcome this problem, a new imaging technique has recently been proposed [1,2]. This new method uses neutrons, subatomic particles whose zero net electrical charge allows them to penetrate thick layers of matter, but whose intrinsic magnetic moment makes them highly sensitive to magnetic fields. Utilizing the magnetic interaction of a spin-polarized neutron beam, it is possible to visualize magnetic fields both in free space and in the bulk of solid, massive, opaque samples, revealing the field line distribution both in two and three dimensions [3,4,5].

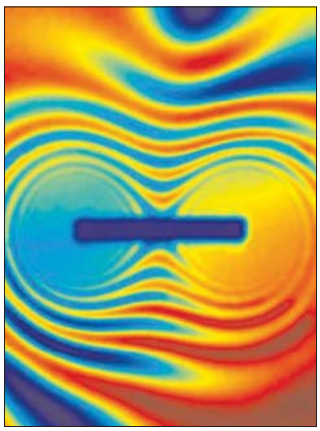

Fig. 2: A radiograph showing the field lines surrounding a bar magnet. The magnetic field decreases in strength with distance from the magnet, resulting in a series of maxima and minima, where the beam polarization is sequentially parallel or anti-parallel, respectively, to the analyzer. Very close to the magnets (where the field is strongest) the field lines are too close together to be resolved spatially [3,4].

Polarized neutron radiography

The neutron is sensitive to magnetic fields due to its magnetic moment, which is anti-parallel to its spin. In the presence of a magnetic field the magnetic moment will undergo a Larmor precession around the field. Polarized neutron radiography is based on the spatially-resolved measurement of the final (cumulated) precession angles of a polarized neutron beam (one in which all spins point in one direction) that traverses the magnetic field of the sample. For monochromatic neutrons (neutrons with a uniform velocity) the precession angle can be related to the average strength of the magnetic field through which the neutrons passed. A polarization analyzer located behind the sample converts this angle to an intensity which is measured by a 2D position sensitive detector. The recorded two-dimensional projection image is then determined by the original intensity modified by a product of the normal absorption contrast and the contrast given by the spin analysis due to the rotation of the polarization vector in the magnetic field [1].

Experiments

Magnetic imaging experiments with polarized neutrons have recently been undertaken on the COld Neutron RADiography and tomography facility (CONRAD) at HZB. The setup used a spin□filter to polarize a neutron beam, which was then allowed to pass through a magnetic sample before being analyzed with a second spin□filter and detected by a position sensitive detector (Figure 1). The key to the image thus formed is that the analyzer only transmits the component of the beam polarization that is parallel to its own polarization axis. As a result, the intensity measured behind the analyzer is the initial beam intensity modulated both by conventional absorption (the magnitude of which can be found from a standard radiograph) and by some sinusoidal function that is directly related to the angle by which the polarization has precessed. The maximum (minimum) intensity will be measured when the beam polarization and the analyzer are aligned perfectly parallel (anti□parallel). This has been demonstrated with a variety of magnetic systems. Figure 2 reveals the familiar pattern of field lines surrounding a simple dipole magnet. The rainbow color scale (from blue = minimum to red = maximum) used in the images is related to the intensity variations induced by the sample and by the presence of a magnetic field [3,4]. The decay of the magnetic field strength with distance is indicated by the annular structure of minima (blue) and maxima (red) representing the periodical 2ϖ rotation of the neutron spin. For the quantification of the magnetic field an iterative calculation algorithm based on Biot-Savart law was developed [1]. The comparison between calculated and measured images for a dipole magnet levitating over a

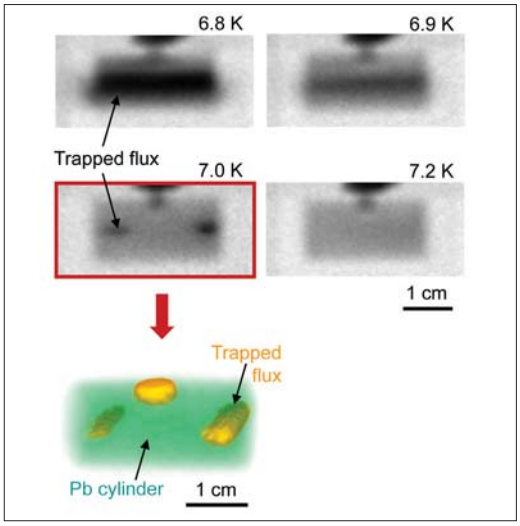

Fig. 4: A three-dimensional reconstruction of trapped flux (yellow regions left and right) inside a polycrystalline cylinder of lead. When cooled to below its critical temperature in the presence of a weak magnetic field, some flux is present inside due to defects and grain boundaries, and this remains trapped even after the field is switched off [1].

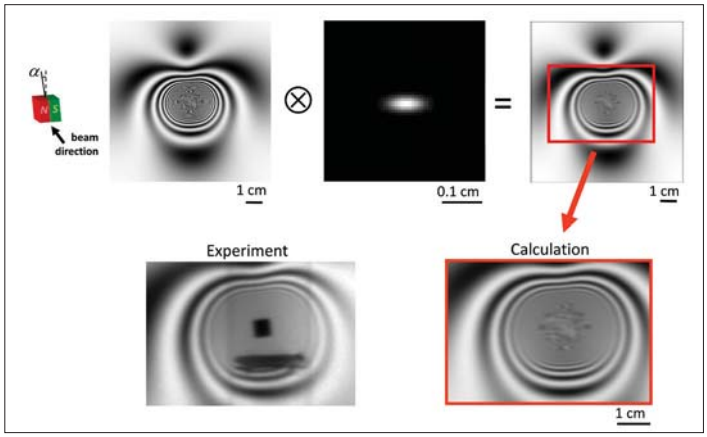

Fig. 3: Comparison of measured and simulated spin polarised neutron radiographies of a dipole levitation over a superconductor: Radiographic image of the levitating dipole (tilted at α=3°) retrieved by a calculation procedure using Biot Savart's law (top) [1]. The corresponding map of the neutron spin rotation in the field was converted into a gray scale image that was convoluted with the resolution function of the instrument. In the central part of the image around the location of the dipole the magnetic field is very strong (up to 1.6 T), causing image artefacts due to the limited sampling of the simulation. Comparison of calculation and experiment (bottom).

superconductor ($YBa_2Cu_3O_7$) is shown in Figure 3. This imaging with spin polarized neutrons can also be extended into three-dimensions using a standard tomographic technique in some instances, as indicated in Figure 4, which shows the distribution of a magnetic field trapped inside a lead cylinder that becomes superconductive when cooled below the critical temperature, $T_c = 7.2$ K [1,2].

Outlook

Spin-polarized neutron imaging is a non-destructive method that provides a number of advantages compared to 2D magnetic imaging techniques using garnet films or scanning techniques (for magnetic fields outside of the sample). The method is applicable to very different environmental set-ups (e.g. for low or high temperature investigations) and samples can be investigated from almost any viewing angle. In this way 3D information about the field distribution can be revealed (even if no mathematical tomographic reconstruction is applied). Measurements are fast because approximately one million pixels are acquired per image within a time-range of several seconds to several minutes. No other method can compete with these advantages even in free space and, as demonstrated, time- and space-resolved measurements become possible.

The presence and controlled application of magnetic fields are essential in many areas of science and technology as well as in fundamental physics. For example, investigations of flux distribution and flux pinning in large superconducting samples [1, 2], the skin effect in conductors [5] or magnetic domain distributions in bulk ferromagnets could be visualized and studied in detail. Finally, the radiographic technique can be extended to tomography in order to investigate and visualize magnetic fields three-dimensionally.

[1] N. Kardjilov, I. Manke, M. Strobl, A. Hilger, W. Treimer, Th. Krist, M. Meißner, J. Banhart, *"Three-dimensional imaging of magnetic fields with polarized neutrons"*, Nature Physics 4, pg. 399-403 (2008)
[2] Nature Physics, press release, www.nature.com/nphys/press_releases/nphys0308.html
[3] I. Manke N. Kardjilov, A. Hilger, J. Banhart, *"Einblicke in Magnetfelder"*, Physik in unserer Zeit 4, July 2008.
[4] N. Kardjilov I. Manke, A. Hilger, M. Dawson, J. Banhart, *"Spin-polarized Neutron Imaging"*, Advanced Materials & Processes, July 2008.
[5] I. Manke, N. Kardjilov, M. Strobl, A. Hilger, J. Banhart, *"Investigation of the skin effect in the bulk of electrical conductors with spin-polarized neutron radiography"*, Journal of Applied Physics 104, 1 (2008).

Corresponding author:
Nikolay Kardjilov
kardjilov@helmholtz-berlin.de

Coating of meso-porous metallic membranes with oriented channel-like fine pores by pulsed laser deposition

N. Wanderka, N. Kardjilov
■ Helmholtz-Zentrum Berlin für Materialien und Energie, Berlin, Germany

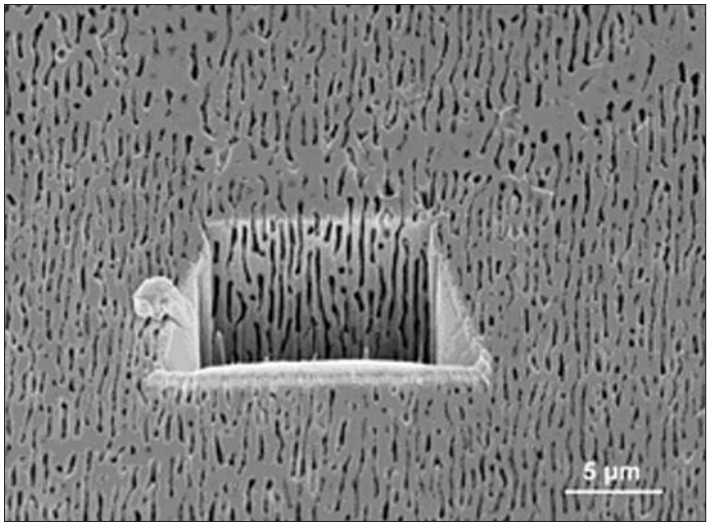

Fig. 1: A slit-type groove, ~10 µm long and of similar width on the membrane surface cut by FIB. Coating on the pore walls was investigated on the cross sections of the porous membrane.

The preparation of thin porous membranes with oriented pore structures has received considerable attention. This is because such structures provide advantages in many applications; for example, separation, catalysis, biosensors, fuel cells/batteries, chemical/microelectronic/photonic devices and therapeutic or diagnostic systems for biotechnology. Such meso-porous metallic membranes can be fabricated (amongst other techniques) by the removal of electrochemical material from simple two-phase metallic alloys. A single-crystal nickel (Ni)-based superalloy (i.e. CMSX4), was used for fabrication of the meso-porous membrane in this study. The alloy was heat-treated to contain a coherent dispersion of Ni_3Al type γ' - precipitates in a γ phase Ni-solid solution matrix. By exploiting the natural tendency of self-assembly of the coherent γ'- precipitates that exists in such alloy systems (due to the anisotropic lattice misfit distribution), the precipitates align and agglomerate into a continuous interconnected network (commonly known as rafting c.f. Fig. 1), when the superalloy is subjected to a thermomechanical treatment. Such a microstructure is suitable for producing the porous membrane.

Coating on a meso-porous substrate is a great challenge and a uniform coating on all pore walls is difficult to produce, especially when the pores are very fine. The pulsed laser deposition (PLD) method was used in this study to coat the porous membrane with two different materials, diamond-like carbon (DLC) and titanium (Ti). DLC and Ti were chosen due to their high compatibility to human tissue and blood cells. It is envisaged that the biocompatibility of the Ni_3Al membrane material may also be improved by the deposition of thin surface layers of DLC or Ti. Such coated membranes may find applications in tissue engineering or in body implants. The aim of the present work was to present the results of the initial experiments with PLD deposition.

Characterisation of coated membranes was carried out in dual-beam system using Carl Zeiss 1540ESB CrossBeam® workstation, which combines an ultra-high resolution GEMINI® field emission column with the high performance focused ion beam (FIB) column. Cross sections of the porous membrane were investigated after cutting a slit-type groove ~10–15 µm long and of similar width on the membrane surface with the ion beam (Fig. 1). In Figure 2, the cross section of the porous membrane coated with DLC is shown. The image actually shows that the membrane surface and the cut cross section are joined at an edge (marked in Figure 2). Whilst the coating on the membrane surface is smooth and hardly distinguishable, the coating on the pore walls is clearly discernible. From this image it is clear that the plasma plume has penetrated all the pores and coated the pore walls. The carbon coating is in the form of a thin continuous film of about 50 nm in thickness. Even for small porous regions (marked with an arrow in Figure 2) there is deposition of carbon. The 3D representation of the porous membrane structure based on the stacking of 178 FIB slice images, after subsequent processing with an algorithm, is shown in Figure 3. The pores have a channel-like formation. A digital

rendering of the 3D volume allows for visualisation of the pore structure by the setting of different levels of opaqueness for the dense material and the hollow spaces. From the inversely rendered image where only the pores are visible, one can see that they are interconnected (Fig. 3(b)).

The PLD process presents a good technique for coating inside pores in the meso-porous membranes up to a thickness of 125 (from one side) and 250 μm (from both sides). The use of FIB for preparing the cross section in the dual-beam system is a useful way to characterise the coatings on the pore walls.

Acknowledgments
FIB/SEM Microscope was purchased with funding from European Union, City State of Berlin and Helmholtz-Zentrum Berlin für Materialien und Energie. This work was performed in cooperation with TU Braunschweig (Dr. D. Mukherji, Prof. J. Rösler) and Laser Center Leoben (J. Lackner), Austria.

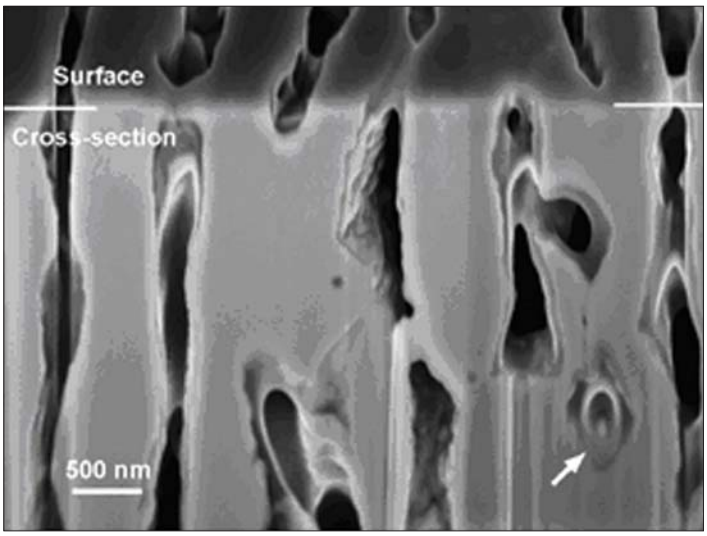

Fig. 2: Cross section of the coated porous membranes. A thin film of carbon coating is clearly discernible on the pore walls. Although the film is continuous, it is not adhering at all places on the pore walls and rather closes and chokes the pores in some channels.

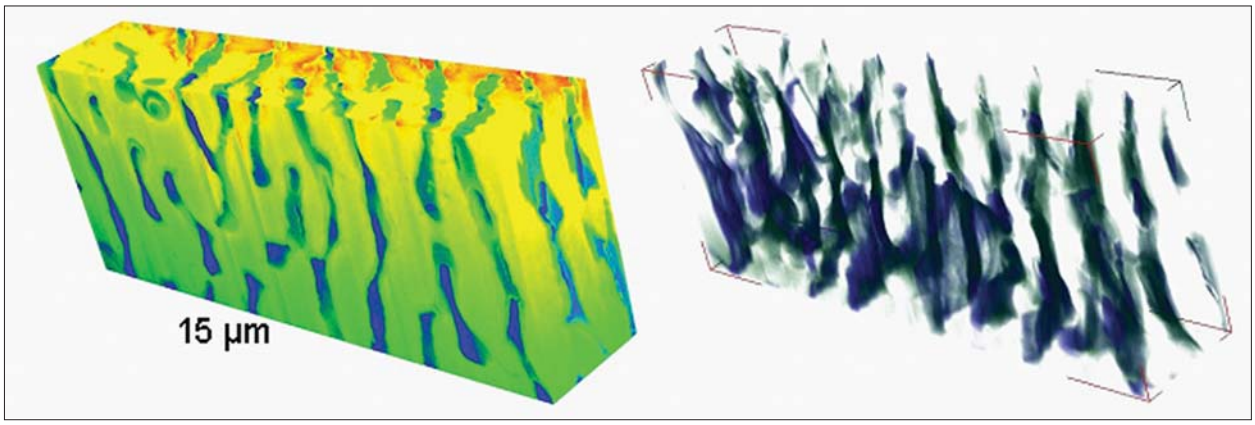

Fig. 3: 3D representation of the porous membrane structure. The volume reconstructed by FIB tomography is approximately 15 μm wide, 7 μm high and 2.5 μm in depth and shows interconnected pores. (a) Reconstructed volume, (b) the inversely rendered image, where only the pores are visible. The pores have a channel-like formation and are interconnected.

Corresponding author:
N. Wanderka
wanderka@helmholtz-berlin.de

Fast radioscopy on liquid metal foams

F. Garcia-Moreno[1,2], A. Rack[3], J. Banhart[1,2]

■ 1 Helmholtz-Zentrum Berlin für Materialien und Energie, Berlin, Germany ■ 2 TU-Berlin: Technische Universität Berlin ■ 3 ESRF: European Synchrotron Radiation Facility, Grenoble, France

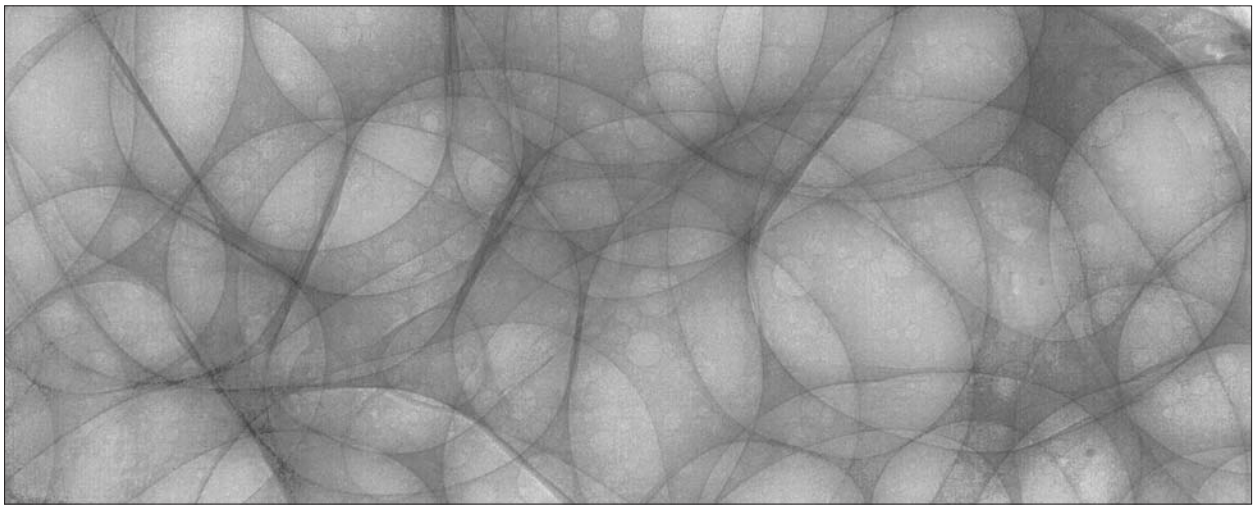

Fig. 1: X-ray radiograph of an evolving metallic foam taken with an exposure time of 600 μs

Radiography with penetrating rays can help to visualize the structure of opaque materials (Fig. 1). To study time dependent phenomena we need a series of radiographies, known as radioscopy. X-ray tubes can be used to study these phenomena, e.g., to visualize oxide films during solidification of aluminium alloys, growth of hydrogen pores in aluminium castings, or convective flow in liquid metals. However, the flux of conventional x-ray sources limits both the accessible frame rates to a few frames per second and spatial resolutions to some 10 μm. Thus in order to study processes in higher spatial and temporal resolution synchrotron radiation is applied.

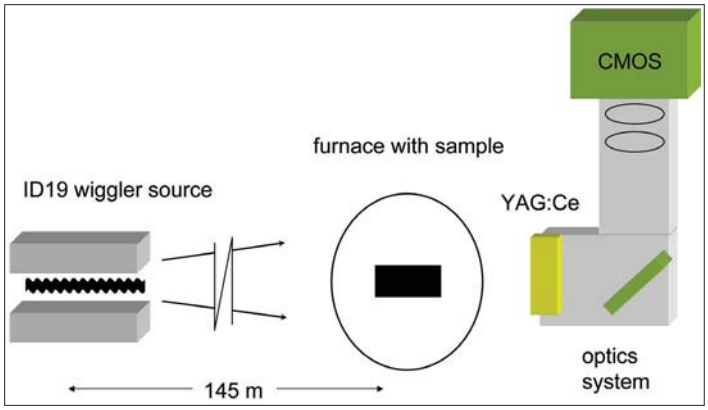

Fig. 2: Sketch of the fast imaging setup used on the ESRF's ID19 beamline

X-ray radioscopy, and especially synchrotron radioscopy, has gained considerable importance for the in-situ examination of evolving metallic foams within the last decade [1]. A common phenomenon in metal foams is coalescence. Thermal or mechanical instabilities lead to the rupture of a film separating two adjacent bubbles and their subsequent merger. It is important to understand the dynamics of these rupture events because they reflect the properties of the constitutive liquid. It has been estimated that these ruptures take place on a time scale of a few milliseconds or even faster. To image them, a very high frame rate is required.

We conducted an investigation of liquid metallic foams by means of high-speed radioscopy and captured 5000 images/s to reveal the details of pore coalescence during growth of Al-6%Si-4%Cu (wt. %) alloy foam [2]. Imaging experiments were carried out using the ID19 beamline at the European Synchrotron Radiation Facility, ESRF. A quasi-white spectrum of ID19's wiggler (gap 40 mm) was used in order to achieve the flux of $\approx 10^{15}$ photons/mm^{2}s required for our fast imaging application. The beam was filtered by 1.5 mm

of aluminium (including the two pressure vessel walls). We chose a PCO (10-bit dynamic range, 60 dB, 12 µm pixel size) as the fast camera. In order to reach the required 5000 frames/ s (200 ms exposure time), we restricted the region of interest to 1280×128 pixels. Fig. 2 shows a sketch of the setup.

The metal foam furnace setup utilised for the experiments consists of a ceramic heating plate placed inside an Al-cylinder (wall thickness: 0.5mm). This cylinder is closed tightly at both ends allowing vacuum and overpressures of up to 10 bar, with connections for heating current, thermocouple and gas in- and outlet. The system is described by the authors in detail in the literature [3].

The furnace was loaded for the experiments with a foamable Al-6%Si-4%Cu + 0.5 wt.% TiH_2 precursor measuring 10 x 5 x 4 mm^3, closed and placed in the beam path. Then it was filled with Ar up to 5 bar and the sample heated up at 25-30 K/s to T = 600°C. After melting, the gas contained in the blowing agent nucleates in the sample leading to a small expansion of ~ 5 – 10%. The pressure in the furnace is then decreased to normal by releasing the gas, a process called Pressure Induced Foaming (PIF) [4] which takes about 5 seconds. During this time, the camera records the foam evolution. The quick expansion produced by the pressure release accelerates the kinetics of foaming, leading to an increased occurrence of cell wall ruptures. The reason for using this method is to increase the number of ruptures during foaming to several hundred (by comparison with around 0-5 ruptures/s in standard foaming) in order to gather enough statistics during the limited measurement time of a few seconds.

In Fig. 3 we can observe the rupture procedure of a cell wall in an Al-6%Si-4%Cu foam in detail. The pore diameters of the foam are in the range of ca. 1-5 mm. The time interval between 2 consecutive images is 200 µs, leading to the total rupture and formation of a new cell wall in t_r = 600±100 µs. The diameter of the bubbles in question is in the range of 3 mm.

Of course, radioscopy does not reveal the true position of all the material and, therefore, we cannot specify how the rupture event was initiated and where exactly the metal in the ruptured features has been redistributed. But by a simple calculation we can affirm that during rupture, viscosity plays a minor role compared to liquid film inertia [2]. In this case, the liquid movement is largely dominated by inertia. This shows that the time taken for individual films to break suggests that the effective viscosity is that of the pure liquid within one order of magnitude.
In the literature, it has been proposed that a foam-stabilizing mechanism may be achieved via dramatically enhanced viscosity which is caused by the formation of a filigree network of oxides forming a gel. It has been found that an apparent viscosity of 400 mPas is the reason for the observed stability of foam columns. With such a high value for viscosity, viscous damping would lead to measurably higher values for t_r. A network of oxide fragments, clearly discernible in microscopic images of solidified foams, might give rise to high viscosity in an undistorted state and block liquid flow out of the films. After rupture, however, this network seems to have broken up. The viscosity of the liquid in the film appears to depend strongly on the history of the melt and the forces acting on it.

In conclusion, using white synchrotron x-ray radiation, a suitable fluorescent screen, and a fast CMOS camera, x-ray image sequences comprising up to 5000 frames/s can be acquired. The temporal evolution of the rupture of an individual metal film within a metallic foam was observed. The observed rupture time of about 600±100 µs is in agreement with a simple model that assumes inertia-limited film rupture and expresses the fact that the liquid in rupturing films is very fluid and behaves like a conventional melt.

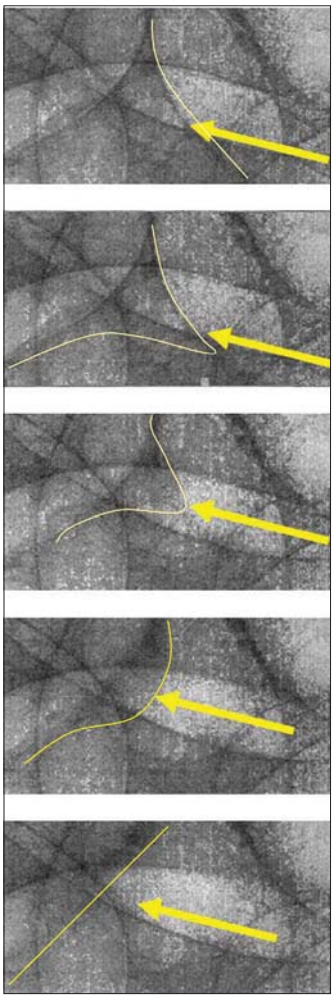

Fig. 3: Radiographs of a metal foam featuring a rupturing film. Images are 200 µs apart. The yellow line denotes the position of the rupturing film.

[1] H. Stanzick, M. Wichmann, J. Weise, L. Helfen, T. Baumbach, J. Banhart, AEM 4 (10), 814 (2002)
[2] F. García-Moreno, A. Rack, L. Helfen, T. Baumbach, S. Zabler, N. Babcsán, J. Banhart, T. Martin, C. Ponchut, M. Di Michiel, APL 92 (13), 134104 (2008)
[3] F. García-Moreno, N. Babcsan, J. Banhart, Col. & Surf. A, 263/1-3, 290 (2005)
[4] F. Garcia-Moreno, J. Banhart, Foaming of blowing agent-free aluminium powder compacts, Colloids and Surfaces A, Vol. 309/1-3, 264 - 269 (2007)

Corresponding author:
F. Garcia-Moreno
garcia-moreno@helmholtz-berlin.de

Relationships between structure and dynamics in hydrogen bonds of biopolymers

Heloisa N. Bordallo[1], Paulo de Tarso C. Freire[2], Elena V. Boldyreva[3], Dimitrios N. Argyriou[1], Antonios Kyriakopoulos[1]

■ 1 Helmholtz-Zentrum Berlin für Materialien und Energie, Berlin, Germany

■ 2 Departamento de Física, Universidade Federal do Ceará, Fortaleza, Brazil

■ 3 Novosibirsk State University, Institute of Solid State Chemistry and Mechanochemistry RAS, Russia

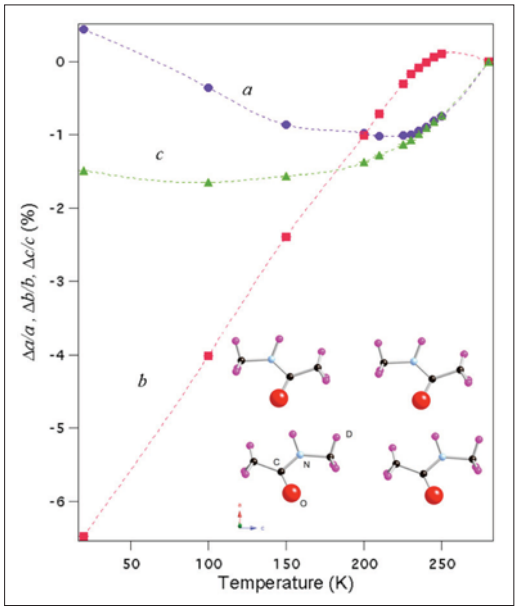

Fig. 1: NMA is built with 1D H-bond chains between amide groups of neighbouring molecules, which may be viewed as a model system for proteins. The temperature variation of the lattice constants shows an interesting behaviour, in which the *a*-axis shows a negative thermal expansion, whilst in comparison the *c*-axis shows a weaker temperature dependence.

Hydrogen (H) occurs in all materials in organic chemistry and the life sciences, and neutrons are commonly used to characterise both molecular motions and conformational changes in these systems. The large incoherent neutron cross-section of H (σ_H) provides both dynamic information from inelastic neutron scattering (INS) experiments and high-quality structural information from neutron powder diffraction (NPD) measurements. This enables the characterisation of conformational modifications that define subtle changes in the structures of bipolymers.

One part of our research focused on model systems for the peptide linkage in polypeptides and proteins. Simplistically, HBs can be explained by the electrostatic attraction between the partial charges on the atoms involved. By combining NPD with INS measurements, we have been able to associate the onset of a negative thermal expansion with a dynamical transition. One example of this is shown in Figure 1, where there is a non-linear increase of the atomic fluctuations around 230 K in N-methylacetamide (NMA). On cooling the O-H distance decreases, and causes intermolecular repulsive forces to increase; and it can be speculated that this triggers the lattice to relax, with the possibility of actual proton transfer at around 230 K[1] . Whilst further investigations are underway, this work shows the potential of NPD to determine structural deformations in small-molecular organic crystals.

Further studies were undertaken to understand the packing and conformation of amino acids. The structure-forming units in crystalline amino acids are similar to those in the biopolymers - head-to-tail chains of amino acids mimicking polypeptide chains; 2D layers mimicking β-sheets. The large σ_H means that a significant and significant background is often observed in diffraction patterns. To circumvent this problem either selective or full deuteration is used. Our initial studies focused on the smallest chiral amino acid, L-alanine ($C_3H_7NO_2$). We performed a careful analysis of its structural parameters using NPD in order to elucidate the role of the HBs. To date, studies on the physical properties of L-alanine have been undertaken, indicating a dynamic Jahn-Teller effect due to charge-lattice coupling[2]. Using selective deuteration, we focused on the dynamics of the different parts of the molecule (see Figure 2). Our findings are striking: deuteration of L-alanine causes significant structural changes as a function of temperature. As the substitution of deuterons (D) for protons (H+) in HB materials gives rise to an increase in HB lengths[3], our results suggest distinctly different relative stabilities between hydrogenated and deuterated L-alanine[4].

Recently[5], we quantified the subtle volume changes due to minor modifications in the packing density that resulted from the decrease in intermolecular distances in the HB networks on crystalline glycine, ($C_2H_5NO_2$). Glycine is an example of a very small organic molecule that

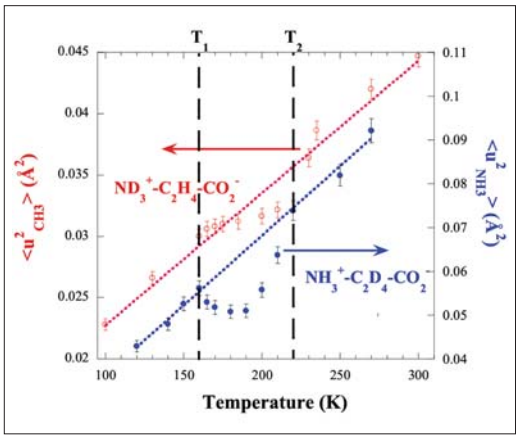

Fig. 2: Evolution of the deduced mean square dependence obtained from measurements using the time-of-flight spectrometer NEAT, as a function of the temperature for $ND_3{+}C_2H_4CO_2$- (left scale) and $NH_3{+}C_2D_4CO_2$- (right scale). The data suggests a structural rearrangement near 160 and 220 K.

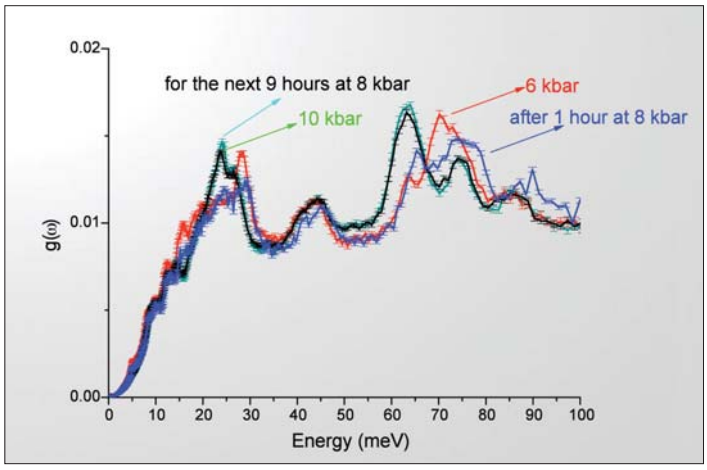

Fig. 3: Density of states for γ-glycine at 300 K as a function of pressure. The comparison of g(ω) measured at atm pressure and after release of the applied 10 kbar pressure indicates that the phase transformation is irreversible.

has several polymorphs, the stability of each depending on subtle changes in the crystallisation conditions and on the strength of the intermolecular HBs that link the head-to-tail chains of the zwitter-ions.

Our ambient pressure INS measurements showed that glycine polymorphs differ significantly in the phonon density of states, both in the positions of the bands and their relative intensities, despite there being only minor differences in molecular structure. The differences in stability of the polymorphs can be explained in terms of changes in intermolecular interactions and the high sensitivity of the conformation of individual molecules. We found that the mean-squared displacement dependencies reveal a change in dynamic properties at about 150 K for all three forms related to a reorientation of the NH_3-group. Besides, a clear and distinct response for the three polymorphs to high pressure was observed. The structure of the helical γ-polymorph was shown to be weak, although the molar volume was smaller than both the layered α– and β-forms. Stability of the α-form, as well as the polymorph transformations in β- and in α-glycine could also be demonstrated. Moreover, a pronounced kinetic effect was observed for γ-glycine: after the sample was kept at 8 kbar for one hour, a phase transition from a helical to a layered form occurred (see Figure 3). These experimental findings allowed us to relate the intermolecular HB response to the dynamic behaviour of the molecular fragments, explaining the ability of the structure to relax mechanically and form polymorphs.

This work has shown the potential use of neutron scattering to differentiate and elucidate biologically important molecules, albeit of small size. At present only molecules of less than 20 atoms have been studied, but we plan to extend this approach to molecules of greater size.

[1] H. N. Bordallo et al. J. of Phys. Chem. B 111, 7725 (2007)
[2] M. Barthès et al. EPJ B 37, 375 (2004)
[3] Such a change in the geometry of HBs is known as the Ubbelohde effect, J. Chim. Phys. 46, 429 (1949)
[4] J. M. de Souza et al. J. of Phys. Chem. B (Letters) 111, 5034 (2007)
[5] H. N. Bordallo, et al J. of Phys. Chem. B 112, 8748 (2008)
[6] http://www.julianvossandreae.com/index.html

Corresponding author:
Heloisa N. Bordallo
bordallo@helmholtz-berlin.de

Electrons suffer from the heat in an ion track

G. Schiwietz[1], M. Roth[1], K. Czerski[1,3], F. Staufenbiel[1], and P.L. Grande[2]

■ 1 Helmholtz-Zentrum Berlin für Materialien und Energie, Berlin, Germany ■ 2 Instituto de Física, Universidade Federal do Rio Grande do Sul, 91501 - 970, Porto Alegre, RS, Brazil ■ 3 Institute of Physics, University of Szczecin, ul. Wielkopolska 15, 70-451 Szczecin, Poland

A team of physicists from Germany and Brazil found that the absorption of fast electrons escaping from hot regions inside solids is significantly influenced by electronic heat - similar to what happens to long-distance runners who slow down or may even stop as a result of excessive heat.

In previous experiments at HMI, it had been shown that individual fast heavy ions may heat up the electrons in their close proximity (the so-called ion track) up to 80 000 K [1]. Such high temperatures were confirmed by independent experiments at the GANIL accelerator [2]. The physical picture that is consistent with most previous investigations is shown in Figure 1 [3]. Target ionisation destroys the bonds and yields hot electrons. Both facts give rise to atomic motions and subsequent materials modifications. Using atomic force microscopy, for example, it is possible to distinguish different depths of origin in the production of nano-structures (crater holes and crater rims) at the surface [4], but the role of hot electrons cannot be directly extracted from such structural measurements.

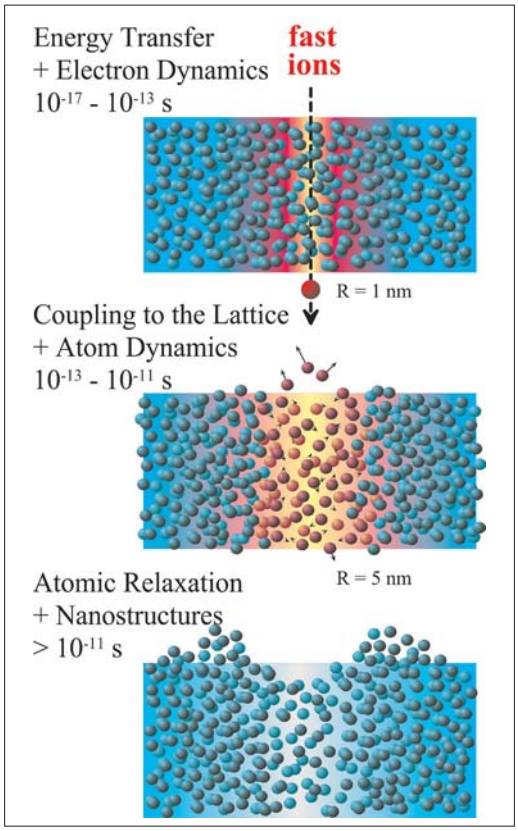

Fig. 1: Time evolution of an ion track [3]. The initial ionisation of atoms induces atomic motions which freeze out and may lead to permanent changes. In the bulk, this may lead to structural or chemical modifications. At the surface, craters or blisters on an atomic scale may also be produced.

So far, electron temperatures at the very centre of ion tracks have been extracted from the shape of Auger spectra [1-3]. The interaction of the escaping electrons with the hot electrons inside the track, however, might also influence the angular distributions. Figure 2 displays the setup for in-situ Auger energy and angular distribution measurements. Experiments have been performed with incident ions and electrons, both at 8% of the speed of light, using aluminum and beryllium samples always at normal incidence.

Figure 3 shows typical Al spectra after background subtraction and decomposition into L-Auger lines, corresponding to one (L^1VV) up to five (L^5VV) L-shell vacancies. Theses L-holes are filled by the interaction of two valence electrons. Already the existence of strong multiple inner-shell components indicates that practically all atomic bonds will break inside a heavy ion track. The L^nVV-lines for incident electrons have been normalised to the ion-peak maxima in the plot. The high-energy edge of the lines for incident ions is slightly broadened, consistent with high electron temperatures [3].

Figure 4 displays the Auger intensity (integrated around the peak maxima in Figure 3) versus ejection angle. Such angular distributions are known to be largely independent of the type of excitation, following roughly a cosine law. In Figure 4 the Auger intensities for two and three L vacancies (L^2VV and L^3VV) have been divided by the main line intensity $I(L^1VV)$ as a reference [5]. Thus, we predicted a constant intensity ratio $R_n = I(L^nVV)/I(L^1VV)$ which was, in fact, seen for R_2 and incident electrons, but clearly not for primary ions. For $I(K^2VV)/I(K^1VV)$ in the case of 592-MeV Au^{46+} + Be, we also determined a decreasing ratio for Auger emission angles close to 180° (for backward emission along the ion track) [5].

These decreasing intensity ratios are consistent

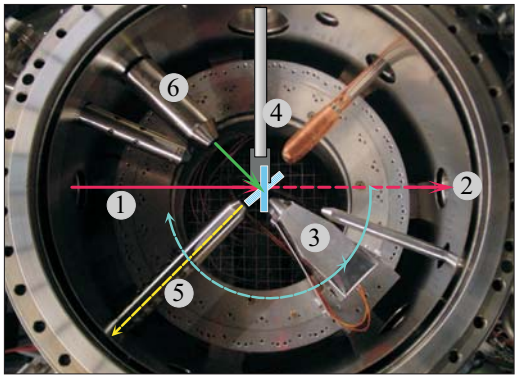

Fig. 2: Doubly magnetically shielded ultra-high vacuum chamber. The ion beam (1) from the ISL-cyclotron enters from the left and hits either the Faraday cup (2) or the target at normal incidence (4). The electron spectrometer (3) can be rotated around the target, after retracting the ion-mass analyzer (5). An electron gun (6) delivers a reference beam on the tilted target (at normal incidence).

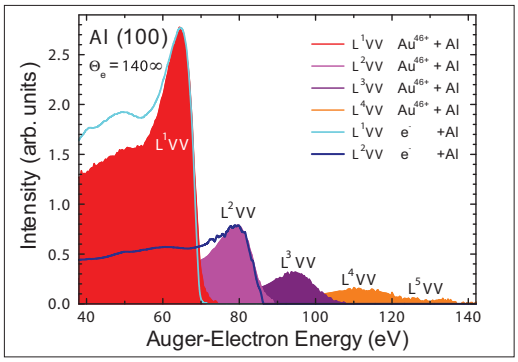

Fig. 3: Decomposed Auger-spectrum (colored areas) determined for 592-MeV Au^{46+} + Al at an electron-emission angle of 140° with respect to the beam direction. The separated peak structures for the L^nVV-Auger transitions represent different degrees of L-shell ionization. The blue and cyan curves show corresponding spectral shapes for incident electrons.

with enhanced electron absorption (enhanced inelastic electron-energy losses) of Auger electrons at high electron temperatures. High degrees of L-shell ionisation correspond to reduced Auger decay times (e.g., $5{\cdot}10^{-15}$ sec for L^3VV instead of $15{\cdot}10^{-15}$ sec for L^1VV), and the corresponding high averaged electron temperatures can exceed twice that for single L-shell vacancies. This broadens the Fermi-Dirac distribution and, consequently, Pauli-blocking effects lose importance when fast electrons move along the track during its high temperature phase.

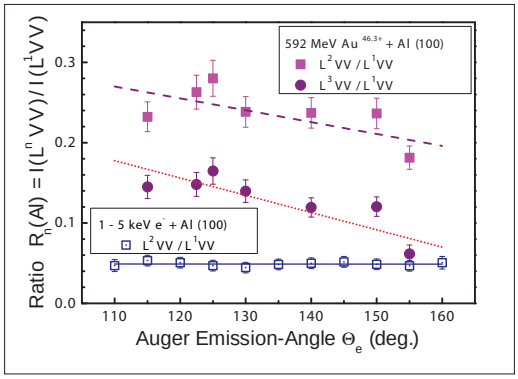

Fig. 3: Angular distribution of the Al-Auger line-intensity ratios for some L^nVV transitions. The straight lines represent error-weighted linear fits and show an unexpected decrease for heavy ions and large angles.

In conclusion, it has been demonstrated that Auger intensity ratios for different degrees of inner-shell ionisation vs. angle are sensitive to the high energy-deposition density. The results indicate that the transport of fast electrons is probing the spatial electronic excitation distribution inside ion tracks.

This work was supported by CNPq, CAPES, Humboldt Foundation and DAAD. We should also like to thank the ISL accelerator crew for delivering the necessary high quality heavy ion beams.

[1] G. Schiwietz, G. Xiao, P.L. Grande, E. Luderer, R. Pazirandeh, U. Stettner; "*Determination of the electron temperature in the thermal spike of amorphous carbon*", Europhys. Lett. 47, 384-390 (1999).
[2] M. Caron, H. Rothard, M. Beuve, B. Gervais, Physica Scripta T92 (2001) 281.
[3] G. Schiwietz, M. Roth, K. Czerski, F. Staufenbiel, and P.L. Grande; "*Femtosecond Dynamics – Snapshots of the Early Ion-Track Evolution*", Nucl. Instr. Meth. B226 (2004) 683–704.
[4] R.M. Papaléo, M.R. Silva, R. Leal, P.L. Grande, M. Roth, B. Schattat, and G. Schiwietz; "*Direct evidence for projectile charge-state dependent crater formation due to fast ions*", Phys.Rev.Lett. 101, 167601 (2008)
[5] G. Schiwietz, M. Roth, K. Czerski, F. Staufenbiel, and P.L. Grande; "*Indications for enhanced Auger-electron absorption in a hot electron gas*", Phys.Rev.Lett. 99, 197602 (2007).

Corresponding author:
G. Schiwietz
schiwietz@helmholtz-berlin.de

Ion-Induced Collective Rotation of Nanocrystals

I. Zizak[1], N. Darowski[2], S. Klaumünzer[2], G. Schumacher[2], J.W. Gerlach[5], W. Assmann[6]

■ 1 Berliner Elektronenspeicherring-Gesellschaft für Synchrotronstrahlung, Berlin, Germany ■ 2 Helmholtz-Zentrum Berlin für Materialien und Energie, Berlin, Germany ■ 3 Leibniz-Institut für Oberflächenmodifizierung e.V., Leipzig, Germany ■ 4 Ludwig-Maximilians-Universität Munich, Germany

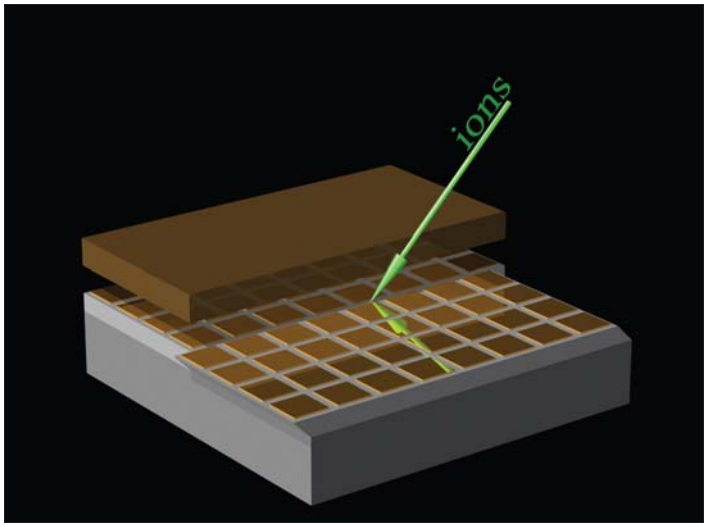

Fig. 1: Schematic view of the irradiation geometry for the detection of shear flow, by the observation of the shift of 20 nm thick gold squares relative to the unirradiated sample part. The shift occurs always in the direction of the projection of the beam onto the specimen surface.

In a solid, a fast heavy ion predominantly creates a trail of electronic excitations, along its straight trajectory. The excitation energy dissipates in the electronic system and is partly transferred to the atoms as a whole, so that on a timescale of 10^{-12} seconds a hot cylindrical ion track is generated, a few nanometers wide and many micrometers long. The lifetime of this thermal spike is between 10^{-11} and 10^{-10} seconds.

Can such tiny entities melt if the electronic excitation is sufficiently strong? A signature of the melting process is the relaxation of the thermo-elastic stresses toward the hydrostatic state. This stress relaxation gives rise to a relaxation strain, which is expected to be 'frozen-in' upon re-solidification. In amorphous materials this frozen-in relaxation strain leads to ion hammering: the dimensions of a free-standing thin specimen grow perpendicular to the ion beam whilst the dimension parallel to the beam shrinks, so that the mass density remains virtually unaltered [1,2]. An experimentally more convenient variant of ion hammering is shear flow in an irradiated layer on a radiation-inert substrate, when the ion beam and specimen normal subtend an angle $\theta \neq 0$ (Fig.1). By applying sufficiently long irradiation times, it is easy to achieve shear strains of $\gamma > 1$. Whilst ion hammering occurs in all amorphous materials, it has never been seen in microcrystalline substances which do not amorphise but remain crystalline during irradiation. The idea was that the dislocation loops, (which would constitute a plastic strain in crystalline matter) would be too small and hence spontaneously collapse and the thermal spike would disappear.

However, in the last three years of ISL accelerator operation, we detected shear flow in nanocrystalline ω-Ti and NiO [3]. Micrometer-thick layers of α-Ti with a pronounced (101) fibre texture have been produced by physical vapour deposition onto (100) silicon substrates. The layers were irradiated with 350 MeV Au ions at 300 K. The originally deposited α-Ti transforms below 1×10^{13} Au/cm^2 into ω-Ti. Figure 2 shows a micrograph of a ω-Ti layer (d = 2.7 μm, original grain size ≈

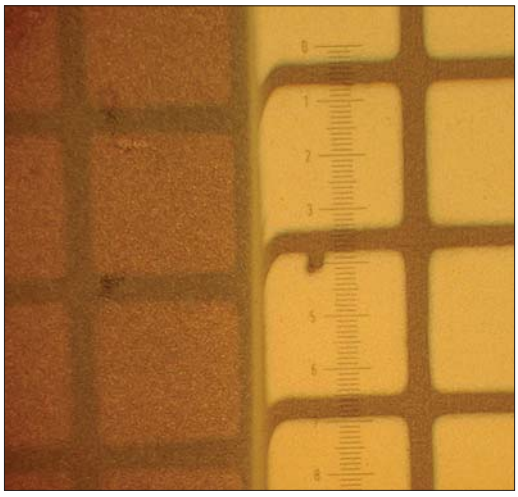

Fig. 2: Optical micrograph of ω-Ti, in which the right half side has been irradiated at 300 K with 350 MeV Au to 1.5×10^{15} Au/cm^2 with the geometry depicted in Fig. 1 ($\theta = 45°$). The arrow indicates the direction of the shift, which is 16.5 μm.

30 nm), where the right half has been uniformly irradiated with a fluence $\Phi t = 1.5\times10^{15}$ Au/cm^2 at $\theta = 45°$. From the surface shift of 16.5 μm, a shear strain of $\gamma = 3$ can be deduced. The situation is somewhat reminiscent to superplastic behaviour, where grain boundary sliding and grain rotation are important constituents. A measurement of the distribution of the crystallite orientations at the KMC-2 beamline at Berliner Elektronenspeicherring-Gesellschaft für Synchrotronstrahlung (BESSY) showed that the shear flow is accompanied by a tremendous collective rotation of the crystallites. In Figure 3 the average rotation angle is plotted versus ion fluence. The rotation angles are much larger than those observed previously during any other kind of material deformation. Changing the sign of θ reverses the direction of both flow and rotation as long as the crystallite size remains unaltered. With ω-Ti we started from nanocrystals whilst for NiO we started from single crystals of (100) or (111) orientation. At fluences ~1×10^{13} Au/cm^2 the single crystals fragmented

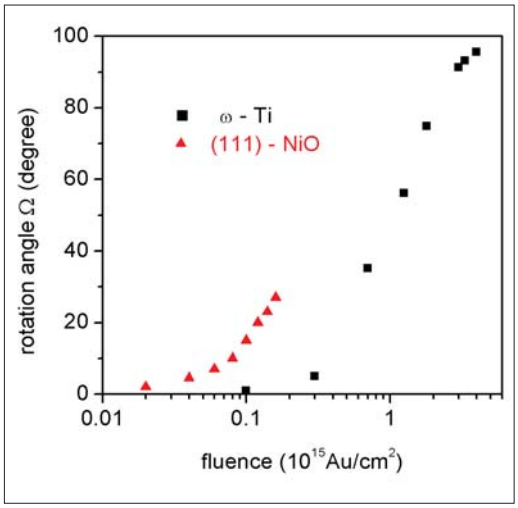

Fig. 3: Rotation angle of nanocrystalline ω-Ti and NiO grains versus ion fluence. The NiO was originally a single crystal with a (111) axis parallel to the surface normal.

into nanocrystals of about 30 nm in diameter. At larger fluences the nanocrystalline NiO exhibited grain rotation similar to ω-T, but the rotation rate (i.e. the rotation per incoming ion) is almost one order of magnitude larger (Fig. 3).

According to the experiments, shear flow and crystallite rotation are strongly coupled: the crystallites behave as if they were floating in an amorphous grain boundary matter and rotate nearly freely in the ion-induced shear velocity field. Amorphous grain boundaries undergoing ion hammering can semi-quantitatively account for this finding [3]. In this scenario grain rotation and shear always remain coupled and stop at large fluences, when grain growth leads to a continuous decrease of the amorphous grain boundary matter. However, the transition from a single crystal to an assembly of nanocrystallites as in NiO cannot be explained by this model.

Another scenario [3] assumes a stream of dislocation loops generated by shear stress relaxation in the ion tracks. Clustering of these dislocation loops in cell walls provides the starting point for the formation of grain boundaries and crystal fragmentation [4]. Subsequently generated dislocations pile up at grain boundary triple points and lead to moving disclination dipoles in the grain boundaries, which couple rotation and shear [5]. Disclination dipoles are specific arrays of dislocations and may play a role in nanocrystalline substances but not in microcrystalline ones [5]. In this scenario stopping of grain rotation without concomitant stopping of shear would occur when the crystallites are oriented such that a direction of easy glide coincides with the shear direction.

[1] S. Klaumünzer and G. Schumacher, Phys. Rev. Lett. 51 (1983) 1987.
[2] H. Trinkaus and A.I. Ryazanov, Phys. Rev. Lett. 74 (1995) 5072.
[3] I. Zizak, N. Darowski, G. Schumacher, J.W. Gerlach, and W. Assmann, Phys. Rev. Lett. 101 (2008) 065503.
[4] P. Hähner, K. Bay, and M. Zaiser, Phys. Rev. Lett. 81 (1998) 2470.
[5] I.A. Ovid'ko, Science 295 (2002) 2386.

Corresponding author:
S. Klaumünzer
klaumuenzer@hmi.de

Spin canting and orbital driven change of exchange pathways in the quasi one-dimensional frustrated chain material CaV_2O_4.

O. Pieper[1,2], B. Lake[1,2], A. Daoud-Aladine[3], M. Reehuis[1,4], K. Prokeš[1], B. Klemke[1], K. Kiefer[1], J. Q. Yan[5], A. Niazi[5], D. C. Johnston[5], A. Honecker[6]

■ 1 Helmholtz-Zentrum für Materialien und Energie, Berlin, Germany ■ 2 Technische Universität Berlin, Germany ■ 3 ISIS Facility, Rutherford Appleton Laboratory, Chilton, Didcot, UK ■ 4 Max Planck Institut für Festkörperphysik, Stuttgart, Germany ■ 5 Ames Laboratory and Department of Physics and Astronomy, Iowa St. University Ames, USA ■ 6 Universität Göttingen, Institut für Theoretische Physik, Göttingen

Low dimensional and frustrated magnetism appears in materials, where magnetic ions are arranged within the crystal lattice in such a way, that long-range order (LRO) caused by interactions between the ions cannot be established. Such quantum magnets attract a great deal of interest, since their ground states and spin dynamics differ significantly from bulk magnets [1]. The quasi-one-dimensional frustrated antiferromagnet CaV_2O_4 is from particular interest, since it possesses an additional orbital degree of freedom. By developing orbital order, this material can relax the frustration, giving rise the preferred exchange pathways.

CaV_2O_4 gains its magnetic properties from the V^{3+}-ions with two Hund-coupled electrons in the 3d-shell, leading to a total spin $S=1$. The material crystallises in the orthorhombic $CaFe_2O_4$-type structure at room temperature. The structure consists of double chains of edge-sharing VO_6 octahedra running along the crystallographic **c** direction. Within each chain the magnetic V^{3+} ions are arranged in a zigzag-like fashion with similar distances between nearest and next nearest neighbours. Since the dominant exchange mechanism is antiferromagnetic (afm) direct exchange, the underlying triangular motif is expected to give rise to geometrical frustration (Fig. 1) [2, 3]. In addition, the octahedral crystal field splits the 3d-levels, making the triply-degenerate t_{2g} orbital states accessible to the two electrons. However this orbital degeneracy is potentially lifted by distortions in the octahedral environment.

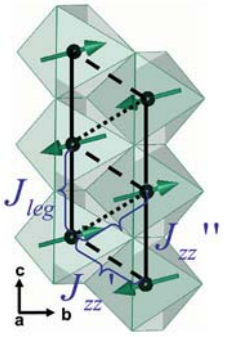

Fig. 1: The magnetic structure of CaV_2O_4. The V^{3+}-ions (black spheres) are located in the centres of the VO_6 octahedra. The arrows indicate the direction of the spin moments and the intrachain exchange constants are labelled. At high temperatures $J_{zz}' = J_{zz}''$.

To understand the complex physics of CaV_2O_4, both neutron diffraction and high temperature static susceptibility measurements were performed on single crystals. The DC magnetic susceptibility was measured at MagLab/LaMMB, Helmholtz-Zentrum Berlin (HZB), using a Quantum Design Physical Properties Measurement System. The temperature dependent susceptibility for a magnetic field applied along all main crystal axes is shown in Figure 2. The data shows the onset of afm LRO below $T_N=71$ K with the **b** axis being the easy axis. Interestingly a substantial finite susceptibility remains along this axis even to the lowest temperatures, possibly due to quantum fluctuations and/or spin canting. Furthermore, the data reveal a broad maximum around 270 K and a Curie-Weiss fit gives a Curie temperature of 418(5) K which is substantially higher than the Néel temperature [4]. Both results are indicators of low-dimensional and/or frustrated behaviour. To gain further information about the exchange interactions and the degree of frustration, exact diagonalisation (ED) calculations of a spin-1, one-dimensional Heisenberg model with nearest (J_{zz}) and next nearest neighbour (J_{leg}) exchange interactions (Fig. 1) were performed and the results were fitted to the high temperature data ($T>200$K) (see inset Figure 2). Surprisingly the best fits were obtained for solutions with either J_{zz} as the dominant coupling (and weak J_{leg}) or vice versa, rather than for approximately equal and frustrated couplings. Therefore, the ED fit suggests a single chain model at high temperatures.

To elucidate this issue and to clarify which mechanism relaxes the spin frustration it is essential to get detailed information about the magnetic structure. Thus, single crystal neutron diffraction experiments were performed using E4 and E5 at HZB and the Single Crystal Diffractometer (SXD) at ISIS. The data revealed that CaV_2O_4 undergoes an orthorhombic to monoclinic structural phase transition at $T_S=137$ K, and that it develops afm LRO below $T_N=71$ K with magnetic Bragg peaks appearing at $(h,k,l) + (0,0.5,0.5)$ positions (Fig. 3). Due to the lowering of crystal symmetry all magnetic reflections are twinned, thus significantly increasing the level of complexity for extracting a detailed magnetic intensity list. Our final refinement reveals a collinear spin structure within each zigzag chain, with antiparallel alignment of successive V^{3+} spins

along the legs and alternating antiparallel-parallel alignment along the zigzags. Spins of neighbouring chains are canted with respect to each other by equal and opposite amounts from the **b** axis (Fig. 1).

Deeper insights into the exchange paths can be gained by relating these findings to possible orbital arrangements, as the antiferromagnetic direct exchange interactions between neighbouring V^{3+} ions arises from overlap of their occupied t_{2g} orbitals. Since there are two electrons and three t_{2g} levels it is important to know the orbital energy level diagram in order to know which orbitals are occupied and can contribute to the exchange paths. This can be achieved by inspection of the octahedral environment. In the high temperature orthorhombic phase, the VO_6 octahedra are compressed in such a way as to lower the energy of the orbital with lobes along the legs, this orbital is therefore occupied by an electron and J_{leg} is strong. The second electron is shared between the remaining two orbitals which have lobes along the zigzag direction; this partial occupancy suggests a substantially weaker J_{zz} interaction (Fig. 3). Based on these findings, it follows that the dominant exchange coupling obtained from fitting the susceptibility data is the one along the legs.

In the low temperature monoclinic phase, the two V^{3+} ions are shifted slightly and there are now two distances along the zigzags leading to two inequivalent interactions J_{zz}' and J_{zz}''. The transition also distorts the VO_6 octahedra in such a way that the orbital degeneracy is completely lifted and the two electrons fully occupy the two lowest lying t_{2g} orbitals while the third orbital is completely empty. Since antiferromagnetic direct exchange arises from overlap of occupied t_{2g} orbitals, the resulting orbital pattern can be simply deduced from the magnetic structure (Fig. 1a). We conclude

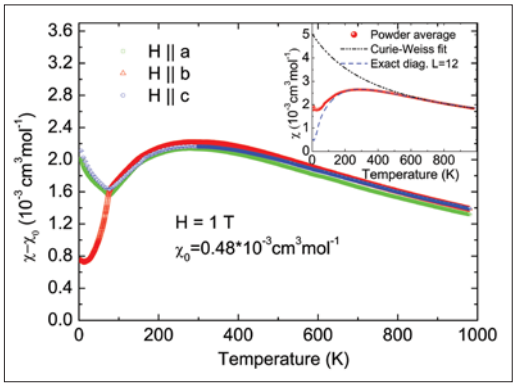

Fig. 2: Single crystal dc magnetic susceptibility of CaV_2O_4 along all crystallographic directions. The inset shows the powder averaged data fitted to Curie-Weiss and exact diagonalisation models.

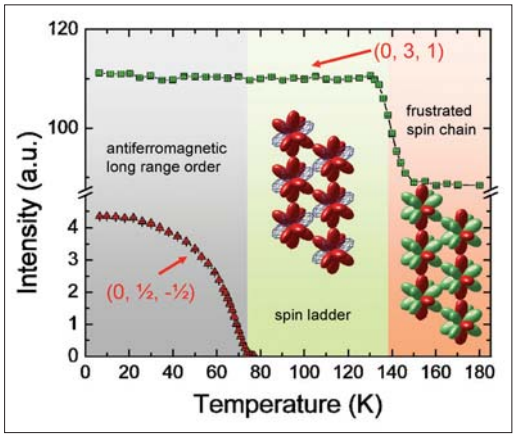

Fig. 3: Integrated intensity of magnetic (0, ½, - ½) and nuclear (0,3,1) Bragg peaks vs. temperature. The different background colours indicate different phases of the material. The insets show the orbital pattern occurring in the dedicated phases. Colour code: red; orbital fully occupied by one electron; green, orbital partially occupied by one electron; blue 'net', empty orbital.

that the J_{zz}'' interaction is weak and that the orbital with lobes along this exchange path is unoccupied, whilst the other two exchange paths are strong and the orbitals along these directions are fully occupied (Fig.3). The low temperature exchange paths are therefore completely unfrustrated and the structure can be interpreted as an S=1 spin ladder [4].

Our work shows the direct connection between orbital configuration and exchange paths and how a structural distortion can simultaneously relieve both orbital degeneracy and magnetic frustration, and can give rise to new magnetic structures.

[1] U. Schollwöck, J. Richter, D. J. J. Farnell, and R. F. Bishop, eds., *Quantum Magnetism, Lecture Notes in Physics*, vol. 645 (Springer, 2004).
[2] H. Kikuchi, M. Chiba and T. Kubo, Can. J. Phys. 79, 1551 (2001)
[3] A. Niazi, S. L. Bud'ko, D. L. Schlagel, T. A. Lograsso, J. Q. Yan, D. C. Johnston, A. Honecker, R. W. McCallum, M. Reehuis, O. Pieper, B. Lake, A. Kreyssig, Phys. Rev B 79, 104432 (2009)
[4] O. Pieper, B. Lake, A. Daoud-Aladine, M. Reehuis, K. Prokeš, B. Klemke, J. Q. Yan, A. Niazi, D. C. Johnston, A. Honecker, cond-mat/0812.1808(2008), accepted for publication in Phys. Rev. B

Corresponding author:
O. Pieper
oliver.pieper@helmholtz-berlin.de

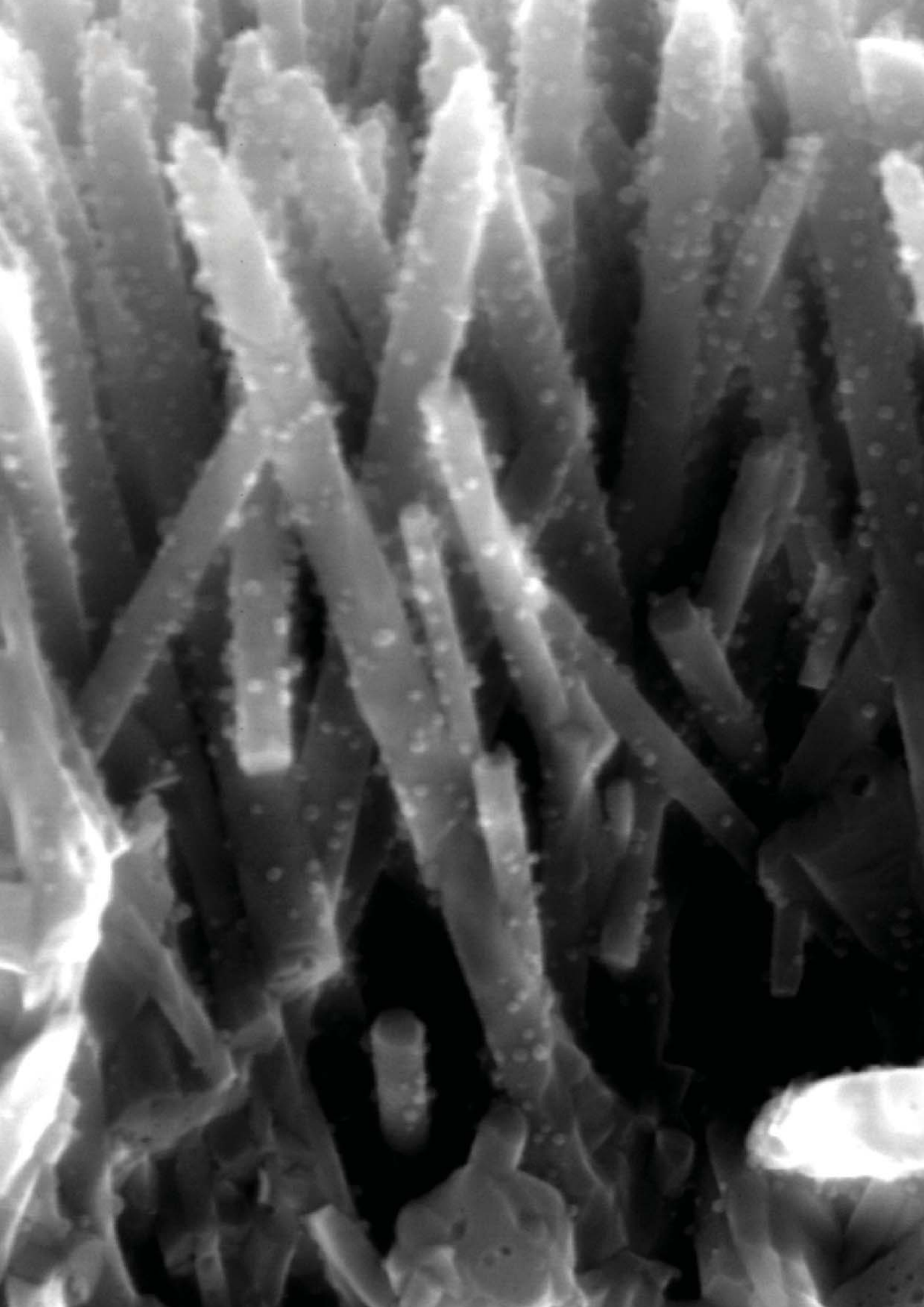

Scientific Highlights
Solar Energy Research 2007/2008

Breakthrough: using temperature-stable ZnO on poly-Si thin film solar cells

F. Ruske, C. Becker, K.Y. Lee, S. Gall, B. Rech
Helmholtz-Zentrum Berlin für Materialien und Energie

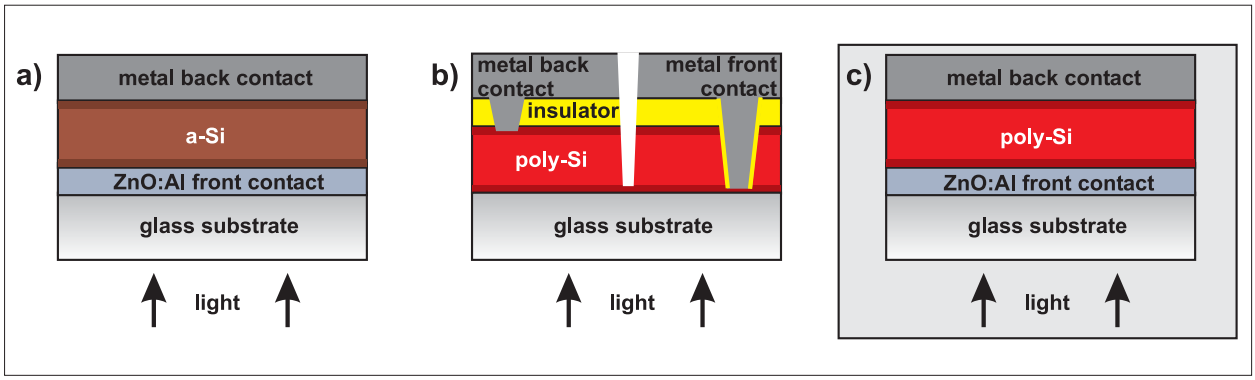

Fig. 1: Structures of state-of-the-art silicon thin film solar cells: a) based on amorphous silicon (a-Si) using a ZnO:Al layer as transparent conductive front contact; b) based on polycrystalline silicon (poly-Si) with the front contacts etched from the rear side (CSG Solar); c) HZB's approach combining both a ZnO:Al front contact layer and high-quality poly-Si produced at high temperatures.

Solar cell contacts are a key issue determining cell efficiency. Contacts have to be applied to both ends of the p-/n-junction of a cell and are usually classified as front or back contacts, depending which side of the solar cell is irradiated with light.

In thin film solar cell technology, the front contact usually consists of a transparent, conducting layer, normally highly doped zinc oxide (ZnO:Al) or tin oxide. Such layers are widely used for thin film silicon solar cells based on amorphous silicon (Figure 1a). In this type of cell the absorber material is deposited at quite low temperatures of about 200°C onto a cheap transparent substrate (e.g. glass), coated with a transparent conducting oxide (TCO) layer. This layer allows the light to enter the absorbing amorphous silicon (a-Si) while the electrical current can be conducted over substantial lateral distances. Due to the high conductivity of these layers resistive losses are still negligible for collection areas with a breadth of several millimetres. Several solar cells of this size can be produced in a series connection by a laser scribing process.

Apart from these advantages, the front contact can also be used to improve the light collection of the cells as the TCO layer reduces cell reflection and can also be used to scatter light into the solar cell, effectively lengthening the light path through the absorber.

Thin film solar cells based on polycrystalline silicon (poly-Si) exhibit the potential for very high material quality and thus better cell efficiency. However, up to now, they have usually been produced without a TCO layer on the substrate, as at some stage in the fabrication process the production of poly-Si requires high temperature treatment which could destroy the TCO layer. At CSG Solar, currently the only company producing poly-Si on a large scale, an annealing step at around 600 °C is applied for several hours.

In order to contact the junction, which is then buried, local wet chemical etching is used to remove parts of the absorber layer, and subsequently contacts are deposited onto the exposed areas (Figure 1b). CSG Solar has developed a sophisticated procedure in which these contacts are formed as point contacts, allowing a series connection of individual cells on large substrates [1].

The present work at HZB aims at combining poly-Si solar cells, offering the potential for high single junction efficiency, with a TCO layer made up of aluminium doped zinc oxide (ZnO:Al) to contact the solar cell from the glass side (Figure 1c). For this approach to be successful it is essential that the zinc oxide layer maintains its high conductiv-

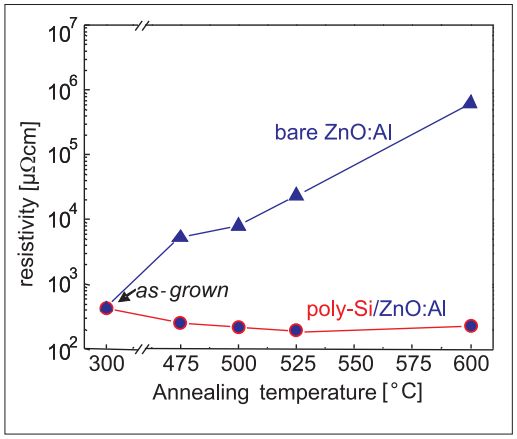

Fig. 2: The resistivity ρ of glass/ZnO:Al/poly-Si (circles) and glass/ZnO:Al (triangles) as a function of the annealing temperature. For all data points up to 525°C the poly-Si films were produced by aluminium-induced crystallisation [4], while the film at 600°C was produced by thermal crystallisation of amorphous silicon.

ity (low resistivity) throughout the thermal treatment needed for poly-Si formation.
In a series of experiments the effect of several hours of thermal treatment on the resistivity of various layer stacks was examined. The resistivity of bare ZnO:Al films on glass was found to degrade quickly compared to the as-grown value (Figure 2, triangles) a finding which had already been documented [2]. By annealing at 600 °C for 24 hours the resistivity was even found to increase by more than three orders of magnitude.

By contrast, the resistivity of the ZnO:Al films coated with silicon is even lower than the resistivity of the as-grown ZnO:Al layer (Figure 2, circles). We ascribe this to an improvement in ZnO:Al quality, as the silicon does not contribute to the total resistance of the stack to any extent. The resulting resistivity of the glass/ZnO:Al/poly-Si samples is almost unaffected by the annealing temperature. Hence, the silicon layer on top of the ZnO:Al effectively prevents the degradation by oxygen or nitrogen [3]. In the case of the samples annealed at 600°C for 24 hours the resistivity of the covered ZnO:Al films dropped from $(4.3 \pm 0.1) \cdot 10^2$ μΩcm to a value of $(3.4 \pm 0.1) \cdot 10^2$ μΩcm. This is a very promising result regarding the application of sputtered ZnO:Al layers in poly-Si thin-film solar cells. The first poly-Si thin film solar cells on ZnO:Al layers were prepared at HZB [5] using high-temperature steps up to 600°C without degradation of the conductivity of the ZnO:Al front contact film.

In conclusion, it was found that the electrical properties of aluminium doped zinc oxide (ZnO:Al) layers remain stable during heat treatment if they are covered by a thin silicon film. These ZnO:Al layers withstand annealing temperatures and times which are typical for poly-Si thin-film fabrication. This means that ZnO:Al thin films can be used as transparent conductive front contact for poly-Si solar cells.

[1] M.A. Green, P.A. Basore, N. Chang, D. Clugston, R. Egan, R. Evans, D. Hogg, S. Jarnason, M. Keevers, P. Lasswell, J. O'Sullivan, U. Schubert, A. Turner, S.R. Wenham, and T. Young, Solar Energy 77, 857 (2004)
[2] T. Minami, T. Miyata, and T. Yamamoto, J. Vac. Sci. Technol. A 17, 1822 (1999)
[3] K. Y. Lee, C. Becker, M. Muske, F. Ruske, S. Gall, B. Rech, M. Berginski, and J. Hüpkes, Appl. Phys. Lett 91, 241911 (2007)
[4] S. Gall, J. Schneider, J. Klein, K. Hübener, M. Muske, B. Rau, E. Conrad, I. Sieber, K. Petter, K. Lips, M. Stöger-Pollach, P. Schattschneider, and W. Fuhs, Thin Solid Films 511-512, 7 (2006)
[5] C. Becker, E. Conrad, P. Dogan, F. Fenske, B. Gorka, T. Hänel, K. Y. Lee, B. Rau, F. Ruske, T. Weber, M. Berginski, J. Hüpkes, S. Gall, and B. Rech, Sol. Energy Mat. Sol. Cells, (2008)

Corresponding author:
S. Gall
gall@helmholtz-berlin.de

Photoconductivity in Single Si/SiO_2 Quantum Wells

Bert Stegemann, Thomas Lussky, Andreas Schoepke, Manfred Schmidt
■ Helmholtz-Zentrum Berlin für Materialien und Energie Berlin, Germany

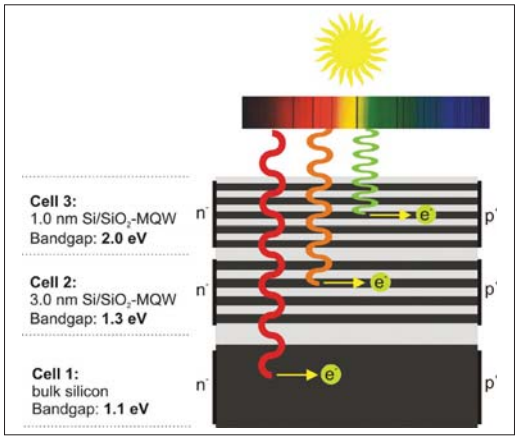

Fig. 1: Conceptual design of an all-Si tandem cell, based on Si/SiO_2 multiple QW superlattices. Two solar cells of different energy bandgaps controlled by QW thickness are stacked on top of a c-Si cell.

Introduction

The major loss factor in conventional solar cells is the thermalisation of hot charge carriers generated by photons with energies exceeding the bandgap energy. Third-generation photovoltaic science aims to significantly increase conversion efficiency by circumventing these thermalisation losses. A promising concept explored by our group is the use of multiple absorbers consisting of Si/SiO_2 multiple quantum wells (QWs), in order to provide energy bandgap tunability via the utilisation of quantum size effects and thus adaptation to the solar spectrum. The conceptual design of such a photovoltaic device is shown in Figure 1: two solar cells of different bandgaps controlled by the QW thickness are stacked on top of a third c-Si cell, so that each stack is able to absorb a different part of the solar spectrum. The basic building block of such superlattices is a single QW. Thus, the present study focused on the well-defined preparation of $SiO_2/Si/SiO_2$-QWs and the analysis of their properties, in order to provide a gateway to the enhancement of solar cell efficiencies by the utilisation of quantum size effects.

Method

Basically, Si/SiO_2 single QWs were prepared under ultrahigh vacuum conditions in four sequential steps: [1] deposition of ultrathin, initially amorphous Si layers onto clean 2" SiO_2 substrates, [2] RF plasma oxidation with thermalised, neutral oxygen atoms at 600°C, [3] crystallisation by thermal annealing at 1000°C, [4] interface passivation by hydrogen treatment. After preparation, the samples were analysed by photoelectron spectroscopy with either x-ray excitation (XPS, 1253.6 eV) or near-UV light excitation (NUV-PES, 6.5 eV). XPS analysis of the chemical shift of the Si2p core level electrons was used to identify interface stoichiometry and NUV-PES was applied to analyse electronic gap state densities at the SiO_2/Si interface. For photoconductivity (PC) measurements, coplanar Ohmic contacts were prepared and the samples were illuminated with monochromatic light of variable photon energy and intensity.

Results and Discussion

The cross-sectional TEM image (inset Fig. 2) shows a typical Si single QW with a homogeneous thickness of ~7 nm, which is covered by a ~2 nm thick SiO_2 barrier. Within the Si layer, lattice planes are clearly visible, indicating a high degree of crystalline order. As evidenced by XPS (Figure 2), the formation of suboxides is highly suppressed by RF plasma oxidation and abrupt Si/SiO_2 interfaces are formed. These physical features are essential prerequisites for the envisaged realisation of Si/SiO_2 superlattices with varying periodicity.
Photoelectrical properties were explored by the analysis of the spectral dependence of the lateral photocurrent, since lateral transport (i.e. parallel to the Si/SiO_2 interfaces of a multi-QW structure) has been demonstrated to be four orders of magnitude more efficient compared to vertical transport across the stack. Figure 3a shows the spectral dependence of the internal quantum efficiency of photoconductivity ($Y_{int,PC}$) for the 7 nm QW. It is evident that even in such ultrathin Si layers a photocurrent can be detected. The onset of the dominant part occurs in the energy range of the direct c-Si bandgaps at 3.6 and 4.2 eV. From $Y_{int,PC}$ a mobility-lifetime-product ($\mu\cdot\tau$) of about 1×10^{-8} cm^2V^{-1} is estimated, and this rather low value suggests a strong influence of Si/SiO_2 interface states on the carrier mobility and lifetime in Si QWs.
Studies on hydrogen passivation revealed a considerable improvement of the photoelectrical performance, resulting in an increase in $Y_{int,PC}$, and

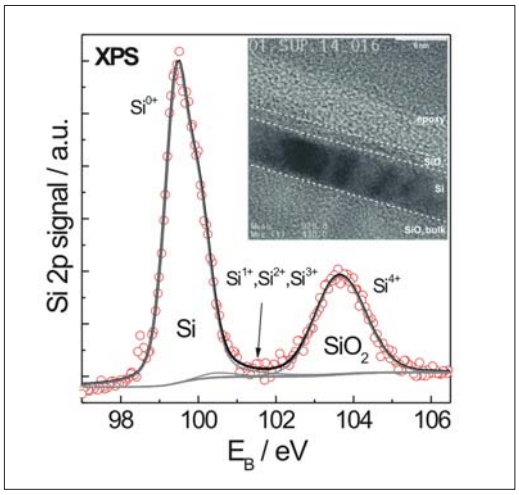

Fig. 2: XPS analysis of the chemical shift of the Si2p signal. Inset: cross-sectional high-resolution TEM image of the Si/SiO_2 single QW.

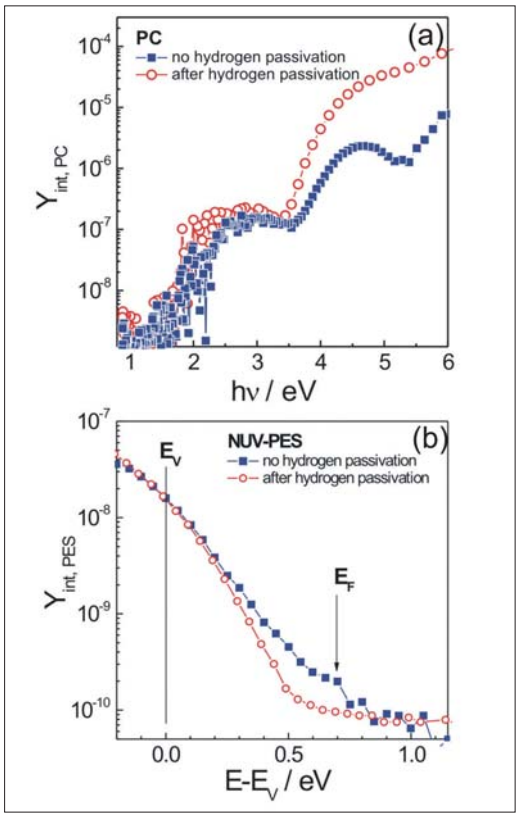

Fig. 3: (a) Spectral dependence of the internal quantum efficiencies of photoconductivity ($Y_{int,PC}$) of a 7 nm Si/SiO_2 single QW, shown on a logarithmic scale. (b) Internal yield from NUV-PES measurements. E_F = Fermi energy, E_V = valence band maximum.

thereby of $\mu\cdot\tau$, by a factor of 10 upon treatment in forming gas (Figure 3a). NUV-PES revealed that this effect is due to the passivation of the occupied defect gap states at the interface of ultrathin SiO_2 and Si. Figure 3b shows the internal photoelectron yield ($Y_{int,PES}$) of the SiO_2/Si(111) interface before and after in situ plasma passivation with hydrogen atoms at nearly thermal impact energies, which turned out to be even superior to forming gas treatment. There is a distinct decrease in $Y_{int,PES}$ particularly around the midgap, where dangling bonds are located. Since, at a first approximation, $Y_{int,PES}$ is proportional to the number of occupied states, it is concluded that this hydrogen treatment efficiently passivates dangling bonds at the SiO_2/Si interfaces as well as at grain boundaries inside the nc-Si layers of the QWs. Moreover, it has been shown that the increase in $\mu\cdot\tau$ (due to dangling bond passivation) is accompanied by a reduction of interface recombination velocity and an increase in effective majority and minority carrier lifetimes, as revealed by constant photocurrent measurements and quasi-steady-state PC respectively .

Summary and Outlook

Si/SiO_2 single-QWs were successfully prepared and studied with respect to possible photovoltaic applications. The presence of a photocurrent in such structures was demonstrated. Internal quantum efficiencies and carrier lifetimes are strongly affected by Si/SiO_2 interface recombination and were enhanced upon hydrogen passivation. These results are promising, but still require substantial improvement before photovoltaic devices based on Si/SiO_2 quantum structures can become widespread in their application.

[1] B. Stegemann, A. Schoepke, M. Schmidt, J. Non-Cryst. Sol. 354 (2008) 2100.
[2] B. Stegemann, D. Sixtensson, T. Lussky, U. Bloeck, M. Schmidt, Chimia 61 (2007) 826.
[3] L. Korte, M. Schmidt, J. Non-Cryst. Sol. 354 (2008) 2138.
[4] R. Rölver, B. Berghoff, D. Bätzner, B. Spangenberg, H. Kurz, M. Schmidt, B. Stegemann, Thin Solid Films 516 (2008) 6763–6766.
[5] B. Stegemann, D. Sixtensson, T. Lussky, A. Schoepke, I. Didschuns, B. Rech, M. Schmidt, Nanotechnology 19 (2008) 424020.
[6] B. Stegemann, A. Schoepke, D. Sixtensson, B. Gorka, T. Lussky, M. Schmidt, Physica E (2009) doi:10.1016/j.physe.2008.08.012.

Corresponding author:
B. Stegemann
bert.stegemann@helmholtz-berlin.de

Room temperature electrical detection of spin coherence in C_{60}

W. Harneit[1,2], C. Boehme[2,3], S. Schäfer[1,2], K. Hübener[1], K. Fostiropoulos[2], K. Lips[2]

■ 1 Freie Universität Berlin, Institut für Experimentalphysik, Arnimallee 14, 14195 Berlin

■ 2 Helmholtz-Zentrum Berlin für Materialien und Energie, Berlin, Germany

■ 3 Department of Physics, University of Utah, 115 S 1400 E, Suite 201, Salt Lake City, Utah 84112-0830, USA

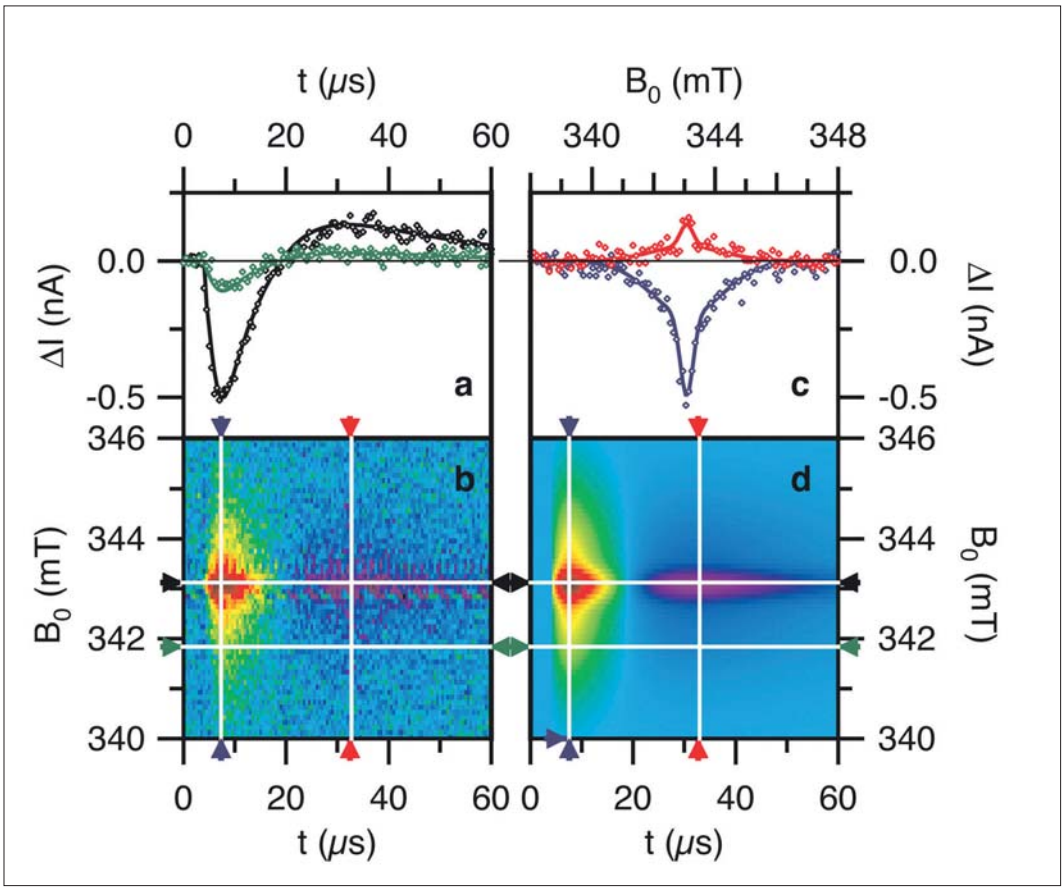

Fig. 1: Transient current ΔI of a C_{60} film illuminated with a halogen lamp, after a microwave pulse. Time traces (a) were recorded at different magnetic fields B_0 to afford the 2D dataset (b). 1D cuts along the field dimension (c) reveal the spin-resonant behaviour. Panel (d) displays a global fit of the data in (b) and markers indicate where the cuts in (a) and (c) were taken (lines = fit, symbols = data).

Spin dynamics and spin coherence in organic materials are of fundamental interest in the applications of organic semiconductors in spintronics [1] and quantum information processing [2], but also in organic photovoltaics. The new method of pulsed electrically detected magnetic resonance (pEDMR) recently developed at SE1, Hahn-Meitner-Institut [3], has been applied here for the first time to thin films of C_{60} fullerenes, an indispensable material for organic photovoltaics [4].

In the field of spintronics and quantum information processing, spin-coherent effects are expected to be sufficiently long-lived only at low temperature. However, we have shown that spin coherence does prevail in this situation even at room temperature [5]. This is due to the fact that, in some sense, organic solids still retain their molecular character. Here, it means that localised electronic (or polaronic) states are often spread out over a few molecules, so that the spin degree of freedom retains the long coherence times well-known for individual molecules.

With our measurements, we detected spin resonance in the photocurrent through thin film devices by way of an ordinary electron spin resonance (ESR) setup that had been equipped with a fast current amplifier [3]. The charge carriers in organic materials are polarons (electrons associated with a surrounding local lattice deformation) that are easily trapped in the often disordered semiconductor matrix. Carrier transport (e.g. hopping) and carrier recombination obey spin selection rules: e.g. P+/P− polaron recombination is fast for spin singlet pair states but slow for triplet pair states. When the organic film is illuminated with an ordinary halogen lamp, a surplus of spin triplet states are therefore generated in the steady state. By placing the sample in a magnetic field and applying resonant microwaves, some of the triplets can be converted into singlets and will undergo fast recombination. We therefore detected a resonant photocurrent quenching as shown in Figure 1.

Spin coherence is evidenced by the fact that the triplet-to-singlet conversion efficiency depends on the length of the microwave pulse in an oscillatory manner. This can be understood as an oscillation of the triplet character, of the polaron pair's wave function. The length of the microwave pulse is proportional to the turning angle φ of the quantum mechanical phase. At $\varphi = (2n + 1)\,\pi$, the triplet-to-singlet conversion is maximal, whilst at $\varphi = (2n)\,\pi$, the original spin pair wave function is restored and no conversion has occurred.

An analysis of the oscillation frequency leads to the assignment of the spin resonance to only one of the polaron pair's spins. A comparison of line width and resonance position (or g factor) with the ESR literature on molecular spin states in C_{60}, leads to the identification of the signal with that of a positive polaron (molecular cation C_{60}^{+}) rather than with that of a negative polaron. The latter is much more mobile and thus likely to be subject to faster decoherence. This assignment is not unambiguous and it has been suggested in the literature that direct C_{60}-C_{60} or 'bridged' C_{60}-O-C_{60} dimers, an ubiquitous impurity in C_{60} films, may be at the origin of this spin resonance. This is in line with our observation that the intensity of the spin signal for separately prepared C_{60} thin films varies considerably even if the total photocurrent is similar.

Our results indicate that spin coherence is present at room temperature in polaronic C_{60} states and therefore, we have begun a more systematic study of this phenomenon in other relevant organic materials and in organic solar cell devices. The goal is to develop a new technique to assess material purity, interface quality and the electronic properties of solar cell devices. This objective may become possible since the spin-dependent phenomena studied here have a direct relation to charge carrier transport and recombination, which are crucial for the efficiency of organic solar cells.

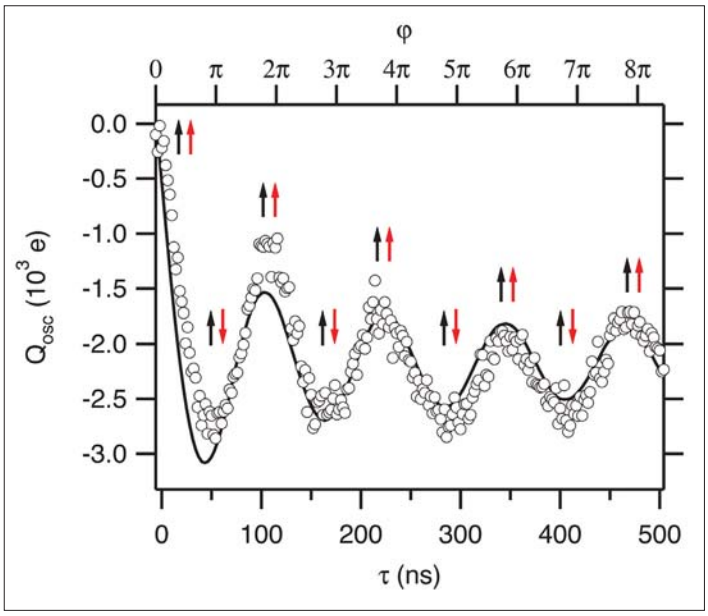

Fig. 2: The oscillatory part of the time-integrated transient current change Q_{osc} (in elementary charges) as a function of microwave pulse length τ. The spin pair state is marked by arrows. The black curve is the theoretical prediction [5] for resonance of only one of the two spins (marked in red).

[1] A.R. Rocha, V.M. García-Suárez, S.W. Bailey, C.J. Lambert, J. Ferrer and S. Sanvito, *Nature Materials* 4 (2005) 335-339.
[2] W. Harneit, *Phys. Rev. A* 65 (2007) 032333.
[3] C. Boehme, K. Lips, *Phys. Rev. Lett.* 91 (2003) 246603.
[4] J. Xue, S. Uchida, B.P. Rand, S.R. Forrest, *Appl. Phys. Lett.* 85 (2004) 5757-5759.
[5] W. Harneit, C. Boehme, S. Schaefer, K. Huebener, K. Fostiropoulos, K. Lips, *Phys. Rev. Lett.* 98 (2007) 216601; W. Harneit, K. Huebener, B. Naydenov, S. Schaefer, M. Scheloske *phys. stat. sol. (b)* 244 (2007) 3879-3884.

Corresponding author:
W. Harneit
w.harneit@fu-berlin.de

In_2S_3 buffer layers for chalcopyrite solar cells

N. Allsop, W. Braun, R. Caballero, C. Camus, Ch.-H. Fischer, S. Gledhill, M. Gorgoi, R. Klenk, T. Köhler, M. Krüger, I. Lauermann, H. Mönig, P. Pistor, F. Schäfers

■ Helmholtz-Zentrum Berlin für Materialien und Energie, Berlin, Germany

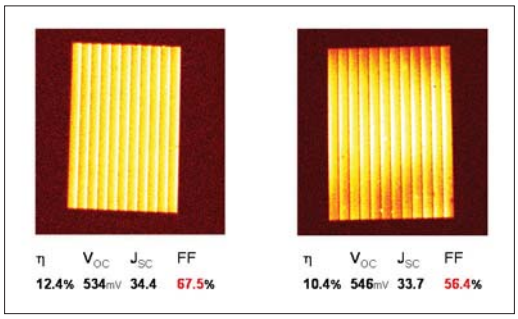

Fig. 1: Thermography and performance of two solar $Cu(In,Ga)(S,Se)_2$ modules with ILGAR In_2S_3 buffer. The increase in efficiency and improved homogeneity of the fill factors are evident (measured at AVANCIS).

ILGAR (Ion Layer Gas Reaction) is an alternative chemical method for the deposition of thin semiconductor layers, developed and patented[1] by HZB. This sequential, cyclic process involves spraying an aerosol containing a solution of a precursor compound, e.g. $InCl_3$ on a heated substrate (200-250°C). Then the sprayer is stopped and a reactant gas, e.g. H_2S is led over the solid precursor film, which is converted into the final product, e.g. In_2S_3. These two steps are repeated until the desired layer thickness is obtained.
Using industrial $Cu(In,Ga)(S,Se)_2$ absorbers produced by AVANCIS, a statistical comparison of the In_2S_3 buffer layers with the standard CBD-CdS buffers was made. The resulting efficiencies were absolutely comparable,[2] as was the stability in accelerated aging tests. ISE Freiburg has certified efficiency of 14.7% for the indium sulfide buffer, which is a very high value for an industrial absorber based cell. A more recent nanostructured ZnS/In_2S_3 buffer reached 15.3%. Additionally, the ILGAR buffer process is very robust with broad parameter windows.
A chamber for 10x10 cm^2 substrates moving over a linear spray nozzle was designed and constructed in house. It demonstrates the easy up-scaling of the process. Figure 1 shows a thermography test of two minimodules revealing that ILGAR buffered modules are homogenous and free of shunts.
Currently, we are working on the buffer deposition on 10 cm wide steel tape in a continuous process. Here, the material yield is clearly superior to the standard CBD process. The In conversion has already been increased to over 30 %. Moreover, the In-recycling is easier due to the lack of by-products, and production speeds should be much higher.

The Spray-ILGAR process can be integrated very easily in an industrial in-line process. CIS-Solartechnik GmbH produces $Cu(In,Ga)Se_2$ solar devices roll-to-roll on steel foil. They chose the ILGAR buffer because of its in-line compatibility, and the process has been successfully integrated into a pilot line. Currently, full production is being planned and a licence contract with HZB has been concluded.
A new collaboration has begun with Stangl Semiconductor Equipment, one of the leading suppliers of wet-chemical equipment for the PV-industry, including equipment for the CBD-CdS buffer layers. Impressed by the advantages of the ILGAR process and the solar cell results with Cd-free ILGAR buffers, the company is now developing industrial ILGAR coaters in cooperation with HZB which should be available commercially in 2009. Stangl will market the ILGAR buffer coaters with the HZB ILGAR process worldwide.

Another approach follows the deposition of In_2S_3 buffer layers by thermal evaporation from the compound In_2S_3. This vacuum deposition method offers full in-line compatibility for module production where the back contact, absorber and window layer are also applied by vacuum methods (e.g. co-evaporation and sputtering.) In this case, the In_2S_3 is deposited onto the cold absorber before completing the solar cell with the ZnO window layer and contacts.
Cells fabricated in this way show only comparatively low efficiencies of approximately 8-10% in the as-grown state. This changes if the completed solar cells are heated to a temperature of 200°C in air. The cell efficiency increases significantly upon annealing -mainly due to increases in the open circuit voltage and fill factor - and reaches values of more than 15% after 35-45 minutes. One of the best cells produced with an $Cu(In,Ga)Se_2$ absorber from the HZB baseline and an evaporated In_2S_3 buffer layer was certified by Fraunhofer ISE, Freiburg, at 15.2% .

In order to understand the effect of the annealing step, several experiments were carried out before and after annealing. We found an increase in the copper content inside the buffer layer after anneal-

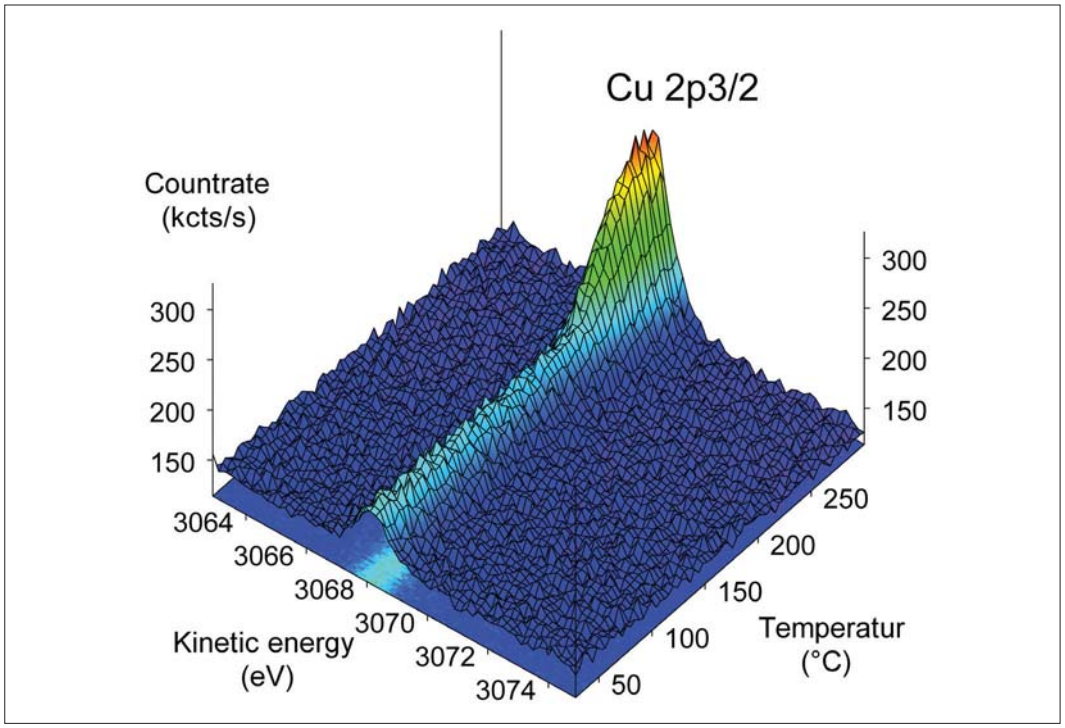

Fig. 2: Development of the high kinetic energy XPS signal of the Cu $2p^{3}/_{2}$ peak during heat up. At the beginning only a small signal from the $Cu(In,Ga)Se_2$ can be detected through the 20 nm In_2S_3 covering layer. Above 200°C Cu starts to diffuse significantly into the In_2S_3 layer and the XPS signal increases.

ing and tried to demonstrate the Cu diffusion into the buffer layer. For this purpose we took advantage of a new tool at BESSY, the HIKE endstation (HIgh Kinetic Energy X-ray photoelectron spectroscopy). This tool offers the opportunity to detect photoelectrons with high kinetic energy of up to 10keV induced by a high resolution and high flux synchrotron beam on the BESSY KMC-1 beamline. The use of higher excitation energies results in high kinetic energy and an increase in the escape depth of the resulting photoelectrons. This vastly extends the information depth by comparison with standard XPS, and photoelectrons can be detected even through cover layers of up to a few tens of nanometres.

In our experiment we used a $Cu(In,Ga)Se_2$ absorber from the HZB baseline and deposited a 20nm In_2S_3 layer on top of it. The absence of a Cu signal for excitation energies $E_{exc.} < 4000$ eV indicated a closed In_2S_3 layer, while for $E_{exc.} > 4000$ eV a low intensity Cu $2p^{3}/_{2}$ signal was detectable through the In_2S_3 layer. At 4000 eV, Cu 2p spectra were recorded continuously while heating the sample up to 300° C. The results are presented in Figure 2. The interdiffusion of the Cu from the absorber into the In_2S_3 layer is clearly indicated by an increase in the Cu signal at temperatures above approximately 200° C. This interdiffusion and the corresponding changes at the $In_2S_3/Cu(In,Ga)Se_2$ interface are probably the key to the increase in the performance of solar cells after annealing and will be addressed in future work.

Acknowledgement: The authors would like to thank Dr. T. Niesen (AVANCIS GmbH, Munich) for the $Cu(In,Ga)(S,Se)_2$ absorbers and the measurements on the minimodules.

[1] Fischer, Ch.-H.; Lux-Steiner, M. Ch.; Möller, J.; Könenkamp, R.; Siebentritt, S.: *"Verfahren und Anordnung zur Herstellung dünner Metallchalkogenid-Schichten"*, German Patent 198 31 214.8 and various Internat. Patents.

[2] N. A. Allsop, A. Schönmann, H.-J. Muffler, M. Bär, M. C. Lux-Steiner and Ch.-H. Fischer, *"Spray-ILGAR Indium Sulfide Buffers for $Cu(In,Ga)(S,Se)_2$ Solar Cells"*, Prog. Photovolt: Res. Appl. 2005; 13:607–616

1 P. Pistor, et al., acccepted for Sol. Energy Mater. Sol. Cells (2008), doi:10.1016/j.solmat.2008.09.015

2 P.Pistor, et al., *"Cu in In_2S_3: interdiffusion phenomena analysed by high kinetic energy X-ray photoelectronspectroscopy"*, submitted to physica status solidi, October 2008

Corresponding author:
Christian-Herbert Fischer
fischer@helmholtz-berlin.de

Beyond conventional thin films: growth and characterisation of chalcopyrite nanocrystals

D. Fuertes Marrón[1,2], S. Lehmann[1], J. Kosk[3], S. Sadewasser[1], and M.Ch. Lux-Steiner[1]
■ 1 Helmholtz-Zentrum Berlin für Materialien und Energie Berlin, Germany ■ 2 Instituto de Energía Solar – ETSIT, Universidad Politécnica de Madrid, Avd. Complutense s.n., 28040 Madrid, Spain ■ 3 Gdansk University of Technology, Danzig, Poland

Introduction

Devices based on Cu-containing chalcopyrite absorbers, with efficiencies around 20 % [1], are currently state of the art in thin-film solar cell technology. In addition to their application in thin film solar cells, chalcopyrites have unique properties, like high absorption coefficients, complex valence band structures, forgiving defect chemistries that also make them interesting for other branches of microelectronics, including sensors, spintronics and non-linear optical devices. In these fields, patterning and lateral structuring at reduced dimensions is commonplace. Even within the field of photovoltaics, the possibility of implementing high-structuring schemes of active materials might be of relevance. For these reasons, it is expected that the development of strategies aiming at the growth of highly structured material will become relevant for new applications, and in turn, widen the potential applications of chalcopyrites beyond standard PV-devices. Additionally, the study of complex structures can provide further knowledge on the basics of growth mechanisms, as well as the structural and electronic properties of chalcopyrite materials.

In view of this, we developed a method for the growth of laterally structured chalcopyrite materials of the $Cu(In,Ga)(S,Se)_2$ type based on the deposition of metal precursors [2-4]. When the set of processing parameters are properly selected, nanocrystals and sub-micrometre polycrystalline dots can be grown in this way, either as isolated units or, alternatively, as embedded structures in a matrix of a binary chalcogenide compound. General investigations of the growth process and characterisation by scanning probe techniques have been performed.

Experiment

The growth of highly structured semiconducting material was considered as a two-fold problem: i) the structuring, i.e. the ability to control the shape and size during the deposition process of the material; ii) the chemistry, i.e. the growth of high-quality material. In order to accomplish both conditions, we opted for a sequential process: 1) the use of metallic precursors deposited on standard Mo-coated glass substrates by evaporation or sputtering to control the structuring, ranging from nanoparticles, macroscopic clusters, or semi-transparent ultra-thin-films; 2) the use of chemical vapour deposition (CVD) as the exemplary reaction process for obtaining the target compounds to control the chemistry. As a precursor, Cu was used in two different forms:

- Cu-nanoparticles were evaporated onto Mo-coated glass substrates. The evaporation process was only run for a few seconds in order to provide a fairly random distribution of Cu particles of nanometre-size, but avoid the formation of a closed Cu overlayer.
- Macroscopic Cu-dots were evaporated using a mask in the form of dots with 500 µm diameter and some 200 nm thickness.

The substrates with the Cu-precursor were subsequently introduced into an open-tube CVD reactor and were exposed to a reactive gas atmosphere containing Ga and Se in the form of metal halide and H_2Se [5]. Scanning probe techniques, namely scanning electron microscopy (SEM), atomic force microscopy and scanning tunnelling microscopy, were used for the characterisation of the structures [2,3].

Results And Discussion

As for any conventional CVD-based process, the effective volatilisation and deposition of material for given temperature T and pressure p can be satisfactorily explained by the unbalance of the chemical potentials µ (molar free energies) of the different species contained in the gas and the solid phases, according to $\Delta\mu=\mu_{gas}-\mu_{solid}$ (Figure 1 A-C). For $\Delta\mu>0$, deposition from the gas continues into the solid phase and for $\Delta\mu<0$, the reaction is perpetuated into the gas phase. The presence of finite precursors on the substrate exposed to the reactive gas introduces lateral variations in the chemical potential inequalities. These variations are responsible for the selective deposition into the solid phase of both the isolated structures at the spots where the precursor is located (Figure 1 B) or, alternatively, for the simultaneous occurrence of reactions into the solid phase *at* and *off* the precursor (Figure 1 C). The result of such pro-

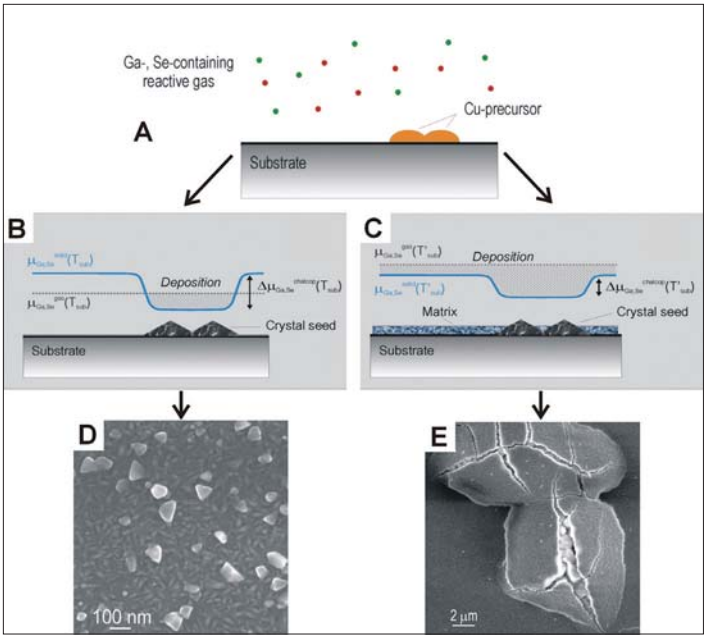

Fig. 1: A: Schematics of the general method employed for the growth of chalcopyrite nanocrystals. The size and distribution of metal precursor particles determine the size and distribution of the crystallites. B: For a given pressure p and temperature T_{sub}, the condition for the growth of isolated clusters of ternary compound relate locally to the precursor for net deposition (hatched area). C: The conditions for the growth of chalcopyrite dots embedded in a matrix formed from the elements contained in the gas phase are shown in C. Local differences still exist for the different solid phases that do or do not contain the precursor as constituent. D: SEM top view of isolated $CuGaSe_2$ nanocrystals grown onto Mo-coated glass. E: SEM top view of $CuGaSe_2$ structures embedded in Ga_2Se_3 after a single reaction process.

cesses is the formation of chalcopyrite structures, either as isolated or as embedded structures in a matrix of a different semiconducting compound. Under the growth conditions at the CVD reactor, the critical parameter governing the switch from one process to the other was the substrate temperature, which can easily be adjusted even during the process.

Single-phase isolated $CuGaSe_2$ nanocrystals were grown on Mo-coated glass from Cu-precursors of nm-size by exposing the precursors to $GaCl_x$ and H_2Se reactants at a substrate temperature T_{sub}= 530°C (Figure 1 D). The growth of semiconductor material takes place at the spots where the Cu-precursor is present, as confirmed by compositional studies *at* and *off* the crystallites.

The adjustment of processing parameters allows the isolated structures to be embedded in a matrix of a binary semiconductor during a single processing step, as shown in Figure 1 E. In this case, $CuGaSe_2$ crystals grown onto Mo-coated glass substrates appear to be covered by a thin Ga_2Se_3 overlayer that probably fractured during fast cooling down due to thermal stress. At the crack, the embedded structures are visible. Similar, crack-free structures have been grown with macroscopic clusters and tiny nanocrystals embedded in them.

The possibility of forming self-assembled semiconductor heterojunctions in a single process is a clear advantage in comparison with alternative methods. A typical tuned process combines a short reaction time at higher temperatures (aiming at the formation of the embedded target material), with a lower temperature last stage, providing the homogeneous coating and more or less inhibiting further reactions between embedded and embedding phases.

Acknowledgments

The authors would like to thank M. Kirsch, S. Wiesner, M. Hafemeister, and J. Albert for technical support and Dr. Ch. A. Kaufmann for SEM/EDX analysis.

[1] I. Repins, M.A.. Contreras, B. Egaas, C. DeHart, J. Scharf, C.L. Perkins, B. To and R. Noufi, Prog. in Phot.: Res. and Appl. 16, 235, (2008)

[2] D. Fuertes Marrón, S. Lehmann, J. Kosk, S. Sadewasser, M.Ch. Lux-Steiner, in *Thin-Film Compound Semiconductor Photovoltaics—2007*, edited by T. Gessert, K. Durose, C. Heske, S. Marsillac, T. Wada (Mater. Res. Soc. Symp. Proc. Vol. 1012, Warrendale, PA, 2007), pp. Y02-07.

[3] D. Fuertes Marrón, S. Lehmann, and M.Ch. Lux-Steiner, Phys, Rev. B 77, 085315 (2008).

[4] D. Fuertes Marrón, S. Sadewasser, S. Lehmann, and M.Ch. Lux-Steiner, patent pending.

[5] D. Fuertes Marrón, A. Meeder, R. Würz, S.M. Babu, M. Rusu, Th. Schedel-Niedrig, and M.Ch. Lux-Steiner, in Proc. Int. Conf. *PV in Europe - From PV technology to energy solutions*, 7-11 October 2002, Rome, Italy, edited by WIP Munich-ETA Florence, pp. 421-424 (2002), and references therein.

Corresponding author:
Sascha Sadewasser
sadewasser@helmholtz-berlin.de

Solar cells based on ZnO nanorod arrays with extremely thin sulphide absorber

Th. Dittrich, A. Belaidi, D. Kieven, J. Tornow, K. Schwarzburg, N. Allsop, M. Rusu, M. Kunst, J. Chen, L. Aé, M. Lux-Steiner

■ Helmholtz-Zentrum Berlin für Materialien und Energie, Berlin, Germany

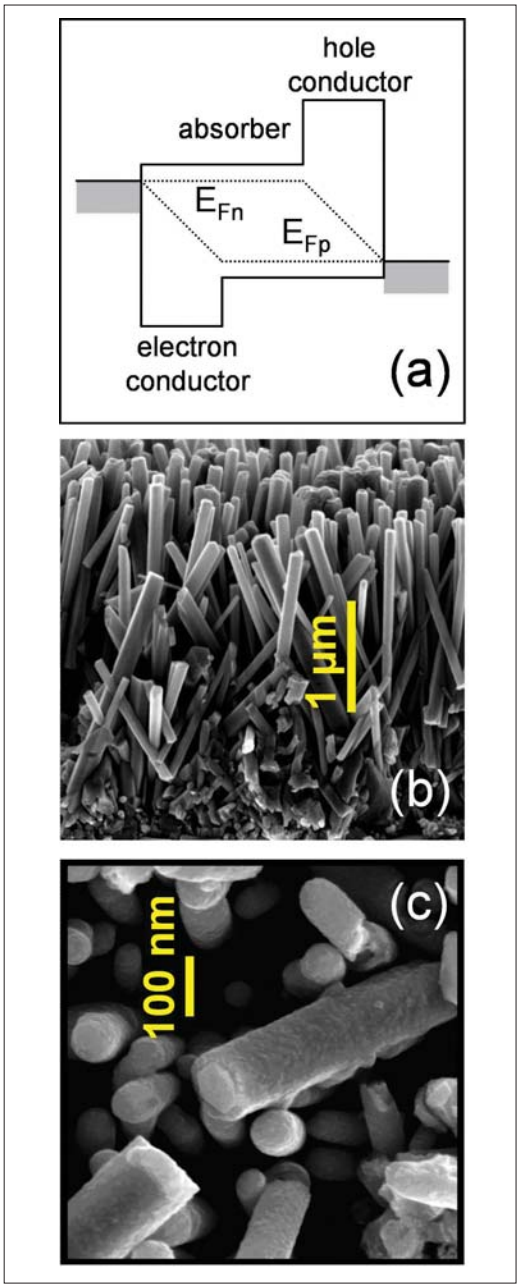

Fig. 1: (a) Idealised local band diagram under illumination. (b) Cross section view of a ZnO nanorod array prepared chemically. (c) Cross section view of a broken ZnO nanorod coated with In_2S_3.

The extremely thin absorber concept

By using nanostructured materials as contacts and absorbers, solar cells with extremely thin absorber (eta) offer the possibility of low-cost solar cells with high efficiency. The eta-concept is based on the high optical density of inorganic absorber layers with a low diffusion length of photo-generated charge carriers (L_{diff}). The absorber is sandwiched between transparent electron and hole conductors (Figure 1). The interface area between the electron and hole conductors is increased by structuring, in order to increase the effective absorber layer thickness and also to incorporate measures of photon management or light trapping [1]. The *local* thickness of the absorber layer (d_{local}) should be less than L_{diff} but larger than the tunnel-ling length (l_{tunn}). This limits d_{local} to the order of tens of nm which is usually significantly lower than the absorption length of the absorber (α^{-1}). Therefore, the absorber has to be folded to reach an effective absorber layer thickness (d_{eff}) which is significantly larger than α^{-1}. The roughness factor (K) is defined as the ratio d_{eff}/d_{local}. In a theoretical model, it has been shown that efficiencies of up to 15% could be reached with d_{local} between 15 and 20 nm and L_{diff} and K being in the order of 10 nm and 10, respectively [2]. For proof of this concept, we developed a model system consisting of ZnO/In_2S_3/In_2S_3:Cu/CuSCN to investigate the roles of interface formation, d_{local} and d_{eff}.

ZnO nanorod arrays as a structured electron conductor

ZnO nanorods were prepared chemically in a chemical bath (CBD) or electrochemically. Figure 1(b) shows an example of a ZnO nanorod array prepared by CBD. Well defined columns of ZnO were formed, with diameters in the range of 40 to 100 nm and lengths in the order of several µm. In this way, K could be changed systematically between 1 and 30 [3]. The ZnO nanorods were highly n-type doped after preparation. The concentration of free electrons was decreased by annealing. The defect concentration in ZnO nanorods was greatly reduced by applying an electrochemical preparation method and in this case, the internal quantum efficiency of the photoluminescence signal of exciton recombination was very high [4, 5].

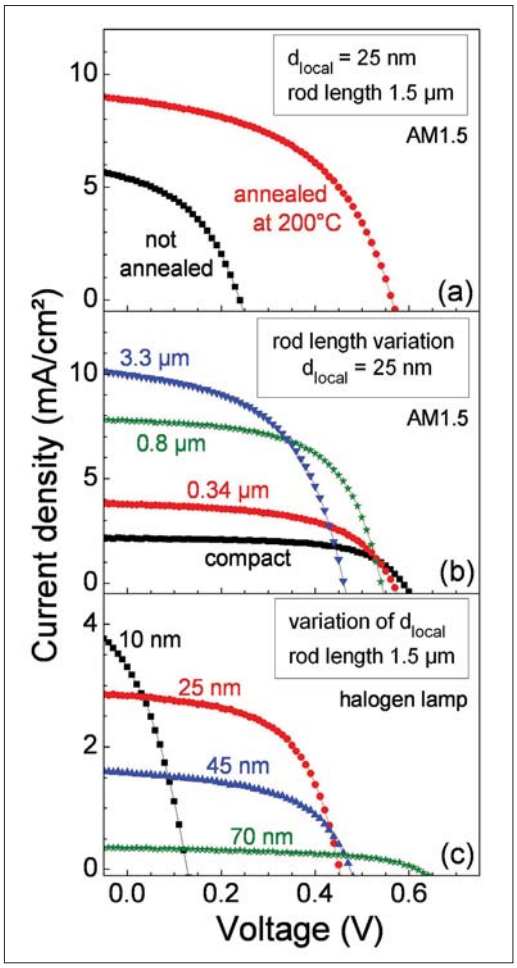

Fig. 2: Current-voltage characteristics of: (a) compact ZnO/In_2S_3/CuSCN before and after annealing at 200°C in air under illumination at AM1.5, (b) of annealed eta-solar cells with constant d_{local} and varying rod length, (i.e. d_{eff}) under illumination at AM1.5, and (c) of annealed eta solar cells with constant rod length and varying d_{local}, under illumination with a halogen lamp.

Sulphide absorber and CuSCN hole conductor

The ILGAR (ion layer gas reaction) technique was used for conformal deposition of In_2S_3 layers on ZnO nanorod arrays. The value of d_{local} was changed to between 10 and 70 nm [6]. The value of d_{eff} was controlled by XRF (x-ray fluorescence). The transparent CuSCN (band gap 3.5 eV) hole conductor was deposited by impregnation from solution. Time resolved microwave photoconductivity measurements showed that L_{diff} ranges between 20 and 30 nm for the given absorber layers and that the mobility of excess holes in CuSCN is of the same order as the mobility of excess electrons in ZnO nanorods. Small area solar cells with Au back contacts were investigated by temperature dependent current-voltage and quantum efficiency (QE) measurements. After the annealing of the solar cells, the QE as well as the surface photovoltage signal increased in the near infrared region due to diffusion of Cu.

The roles of annealing in air and the thickness of local and effective absorber layers

The formation of the charge selective contact at the site of the hole conductor is crucial for reaching relatively high open circuit voltages (VOC). As s A very good correlation between K and the short circuit current density has been demonstrated [3], and is shown in Figure 2(b). However, VOC decreases with increasing K due to increasing diode saturation current density.

Using ZnO nanorods of fixed length, the highest ISC was obtained for the lowest dlocal (Figure 2(c)), [6]. The ISC decreases if the d_{local} is increased from 10 to 25 nm, which gives evidence for L_{diff} < 25 nm. At the same time, VOC increases greatly with increasing d_{local} due to a in decreasing tunnelling recombination.

Summary

The eta solar cell concept has been proven by using a system consisting of ZnO nanorod arrays with In_2S_3/In_2S_3:Cu absorber. The high optimisation potential for this type of solar cell has been demonstrated. At present, energy conversion efficiencies of up to about 3.6% have been reached. Future challenges include the application of alternative building blocks for absorber layers, such as nano-crystallites and quantum dots.

The project was supported by EFRE (WK-2012 / 10133711).

[1] K. Ernst, A. Belaidi, and R. Könenkamp, Semicond. Sci. Technol. 18 (2003) and refs. therein.
[2] K. Taretto, U. Rau, Prog. Photovolt.: Res. Appl. 12 (2004) 573.
[3] D. Kieven, Th. Dittrich, A. Belaidi, J. Tornow, K. Schwarzburg, N. Allsop, M. Lux-Steiner, Appl. Phys. Lett. 92 (2008) 153107-153109.
[4] J. Chen, L. Aé, Ch. Aichele, M. Ch. Lux-Steiner, Appl. Phys. Lett. 92 (2008) 161906.
[5] L. Aé, J. Chen, M. Ch. Lux-Steiner, Nanotechnol. 19 (2008) 475201.
[6] A. Belaidi, Th. Dittrich, D. Kieven, J. Tornow, K. Schwarzburg, M. Lux-Steiner, phys. stat. sol. (RRL) 2 (2008) 172-174.
[7] Th. Dittrich, D. Kieven, M. Rusu, A. Belaidi, J. Tornow, K. Schwarzburg, M. Lux-Steiner, Appl. Phys. Lett. 93 (2008) 053113.

Corresponding author:
Th. Dittrich
dittrich@helmholtz-berlin.de

Electronic properties of grain boundaries in polycrystalline, chalcopyrite-type thin films in solar cells

Daniel Abou-Ras, Jürgen Bundesmann, Raquel Caballero, Christian A. Kaufmann, Jo Klaer, Melanie Nichterwitz, Roland Scheer, Thomas Unold, Hans-Werner Schock

■ **Helmholtz-Zentrum Berlin für Materialien und Energie, Berlin, Germany**

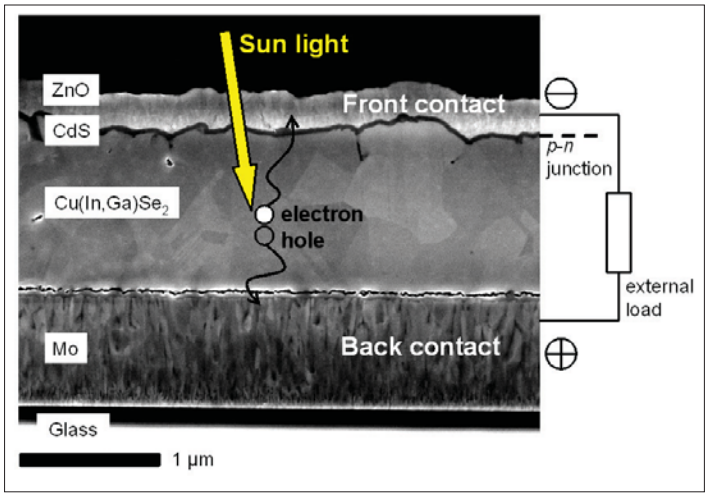

Fig. 1: Scanning electron micrograph from a $Cu(In,Ga)Se_2$ solar cell (cross-section), and the schematics of its mode of operation.

Thin-film solar cells based on polycrystalline, chalcopyrite-type absorbers such as $Cu(In,Ga)Se_2$ or $CuInS_2$ show the potential for high photovoltaic conversion efficiencies at low-cost. It is not yet clear why polycrystalline, chalcopyrite-type, thin-film solar cells exhibit high solar cell performances, as the grain sizes are rather small (averaging about 0.5-1 µm in diameter) and therefore the densities of grain boundaries that are expected to represent locations of enhanced losses, are rather large. The grain boundaries of $CuInS_2$ and $Cu(In,Ga)Se_2$ thin films in completed solar cells were studied by in-line electron holography in a transmission electron microscope, as well as by cathodoluminescence (CL) and electron-beam induced current (EBIC) in combination with electron backscatter diffraction (EBSD) measurements. Grain boundaries were divided into two types exhibiting different electronic activities, Σ3 (twin) and non-Σ3 boundaries ("random").

A scanning electron micrograph from a $Cu(In,Ga)Se_2$ thin-film solar cell in cross-section is shown in Figure 1. The *p-n* junction of the solar cell is composed of the *p*-type $Cu(In,Ga)Se_2$ and the *n*-type CdS and *n*-type ZnO, which also acts as a transparent front contact.

EBIC and EBSD measurements acquired at this cross-section were used to investigate the influence of grain boundaries and grain boundary types on local charge collection. It was found that profiles extracted across grain boundaries from EBIC images show a small yet significant drop in the electron beam induced current for the random boundaries, whereas at the Σ3 (twin) boundaries showed no significant contrast. Quantitative analysis of the electron beam induced current collection was performed by use of a simulation model that took account of the grain boundary recombination velocity, cross-section surface recombination velocity and the bulk diffusion length of carriers. As is shown in Figure 2, grain boundary recombination velocities of $\leq 5x10^3$ cm/s were detected by the EBIC experiment, whereas grain boundary recombination velocities of $<10^3$ cm/s did not lead to a detectable contrast. From comparison of this simulation with the experimentally detected profiles, it may be concluded that random boundaries show recombination velocities in the range of 10^4 cm/s, whereas the recombination velocities of Σ3 (twin) boundaries can be estimated to be lower than the detection limit of 10^3 cm/s.

Complementary information about the electronic and chemical nature of grain boundaries can be extracted from TEM focus series experiments, which were performed on a comparable set of samples. From this experiment, phase distribution images of the regions around Σ3 (twin) and random boundaries in a $Cu(In,Ga)Se_2$ thin film were reconstructed. From the phase distribution images, variations in the mean-inner potentials (MIPs) can be calculated (see Reference 1 for details). The MIP profiles shown in Figure 3 were extracted across Σ3 (twin) and random boundaries and each averaged over 50 individual profiles. It can be seen that the depths of these MIP wells are much larger for the random boundary. Since the extent of the MIP well is about 2-4 nm and therefore much smaller than the estimated Debye length of about 50 nm (density of free carriers about $3x10^{16}$ cm^{-3} in $Cu(In,Ga)Se_2$), the phase contrast cannot be ex-

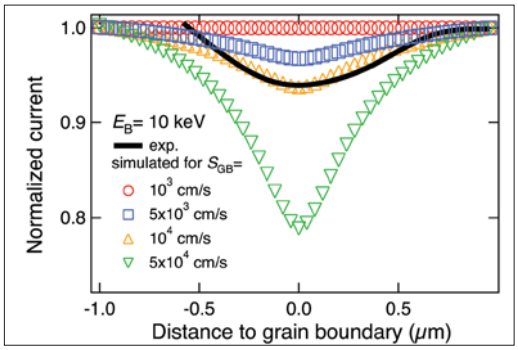

Fig. 2: Extracted EBIC profile across a random boundary (solid line) and corresponding simulations of the current for various grain boundary recombination velocities (coloured icons). The best match between experimental values and simulations is given for a recombination velocity of $1x10^4$ cm/s.

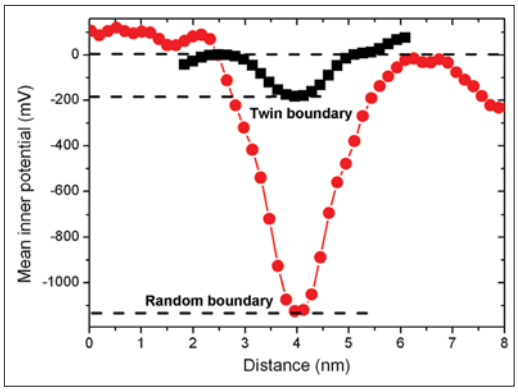

Fig. 3: Mean-inner potential profiles across Σ3 (twin) boundaries (black) and random boundaries (red), obtained from phase images, which were reconstructed by the evaluation of Fresnel fringes in transmission electron microscopy focus series.

plained by a variation in the electrostatic potential around the grain boundary. The estimate of free charge carriers includes the free carriers generated by the electron beam in the experiment and was calculated to be lower than $2x10^{15}$ cm^{-3}. This suggests that the MIP well detected at the grain boundary is likely to be due to a change in composition at the grain boundary.

EBSD and CL images were acquired from solar cells using the related chalcopyrite absorber material $CuInS_2$ (not shown here). These measurements provide direct access to local crystal orientations, grain boundary types and recombination properties. Across several grain boundaries in the $CuInS_2$ absorber layer, CL linescans were extracted with the detection wavelength centred on the band-

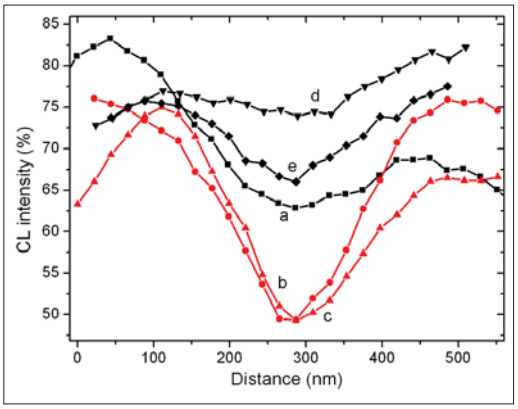

Fig. 4: Profiles extracted from CL images across Σ3 (twin) boundaries (black) and random boundaries (red).

band transition, which is dominant at room temperature. As shown in Figure 4, the CL signal is much reduced at random boundaries (Figure 4, curves b and c) and may be explained by a higher density of defects, acting as (non-radiative) recombination centres. In contrast, this density appears to be significantly smaller at Σ3 (twin) boundaries. In conclusion, the results suggest that Σ3 (twin) boundaries in chalcopyrite-type thin films are electronically less active than random boundaries, as has already been revealed for adamantine systems [3]. A certain density of recombination centres can be expected for all grain boundary types in $Cu(In,Ga)Se_2$ or $CuInS_2$. However, the recombination velocities revealed are rather low, which gives rise to the assumption that there is a mechanism, e.g. a change in composition, which results in a partial compensation of electrically active defects at grain boundaries. In-line electron holography measurements also show a possible compositional difference between grain boundaries and grain interiors.

The authors are grateful to N. Blau, C. Kelch, M. Kirsch, P. Körber and T. Münchenberg for solar-cell processing, and to U. Bloeck and P. Schubert-Bischoff for help in sample preparation.

[1] D. Abou-Ras, C.T. Koch, V. Küstner, P.A. van Aken, U. Jahn, M.A. Contreras, R. Caballero, C.A. Kaufmann, R. Scheer, T. Unold, H.-W. Schock, to be published in Thin Solid Films (2009).
[2] M. Nichterwitz, D. Abou-Ras, K. Sakurai, J. Bundesmann, T. Unold, R. Scheer, H.W. Schock, to be published in Thin Solid Films (2009).
[3] E. Billig, M.S. Ridout, Nature 173 (1954) 496.

Corresponding author:
Daniel Abou-Ras
daniel.abou-ras@helmholtz-berlin.de

Insights into structure and microstructure of thin films by grazing incidence X-ray diffraction

S. Schorr, Ch. Stephan, H.-W. Schock

■ Helmholtz-Zentrum Berlin für Materialien und Energie, Berlin, Germany

Surface sensitive X-ray diffraction can be achieved by using small incidence angles and a multilayer mirror to produce a parallel incoming beam. Because wave penetration is limited, grazing incidence X-ray diffraction (GIXRD) is a powerful method for depth-resolved studies of the structure and microstructure of thin polycrystalline films. The difference to conventional powder X-ray diffraction, which applies the Bragg-Brentano geometry, is that in GIXRD a non-symmetric configuration of incident and reflected beam is used (Figure 1). Thus the lattice plane which fulfils Bragg's law and contributes to a Bragg peak is not parallel to the sample surface. The incident angle is very small (usually between 0.5° and 5°). A GIXRD experiment consists of several detector scans (2θ-scan) measured with different incident angles (0.5° - 5.0°). By increasing the incident angle, the X-ray penetration depth increases, thus revealing structural information from different depths within the thin film.

GIXRD is the method of choice for studying the structure and microstructure of absorber and buffer layers in thin film solar cells. The benefits are that it is non-destructive and fast; moreover, no sample preparation is necessary.

A few characteristic examples will be presented here. Two of them deal with the structure and

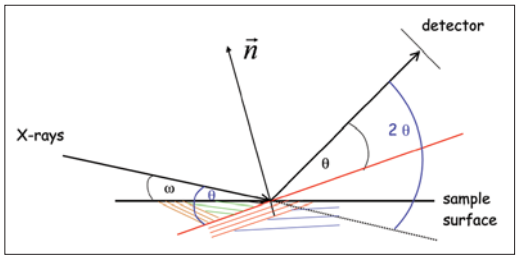

Fig 1: Principle geometry of a GIXRD experiment. The angles are named as follows: ω – incident angle, θ – Bragg angle. The lattice plane normal is marked by $\vec{n}$.

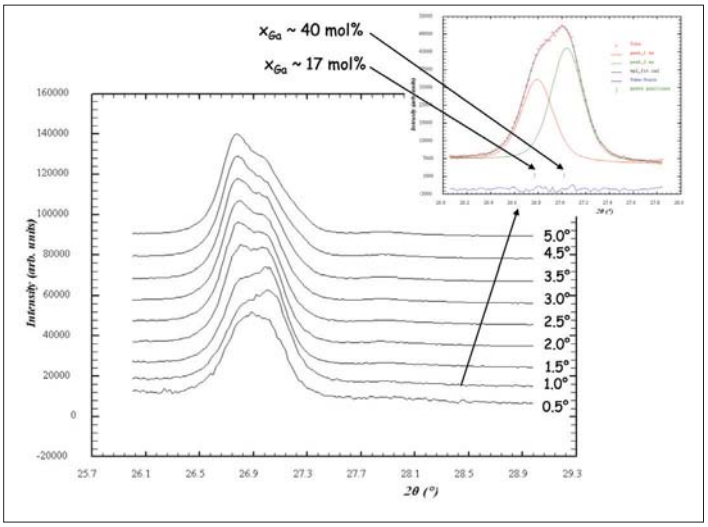

Fig. 2: Part of the GIXRD diffraction pattern (112 Bragg peak) of a $Cu(In_{1-x}Ga_x)Se_2$ polycrystalline thin film with chalcopyrite type structure deposited on PI. The inset shows the multi-peak fit, corresponding to two phases with different Ga content.

phase content of polycrystalline thin films within a thin film solar cell. The $Cu(In,Ga)Se_2$ (CIGSe) absorber is characterised by variations in the Ga content from the top to the bottom of the layer, resulting in a variation in the structural and electronic properties. To investigate this Ga gradient, GIXRD is applied. Analysing the shift in the Bragg peaks of the chalcopyrite type phase, the Ga content can be determined according to depth. Analysing the intensity ratios between the main Bragg reflections, information about the preferred orientation of the layer can be obtained. It should be noted that the Ga gradient determined by GIXRD closely corresponds to values resulting from an EDX (energy dispersive X-ray) analysis of the absorber profiles.

To create the p-n junction of the thin film solar cell, a buffer layer is deposited on top of the absorber layer. This more complex layer structure will be discussed in the third example.

(1) Low temperature growth of $Cu(In,Ga)Se_2$ thin film solar cells on polyimide substrates

Lightweight, flexible $Cu(In_{1-x}Ga_x)Se_2$ (CIGSe) thin film solar cell modules, which are very attractive for space applications, can be produced by the deposition of the CIGSe absorber on a flexible substrate, e.g. polyimide foil (PI).

The structure of a CIGSe absorber layer on PI was studied by GIXRD [1]. The diffraction pattern taken at different incident angles (0.5°-5°) revealed the presence of several CIGSe phases with chalcopyrite type structure but different Ga content (Figure 2). Analysing the shift in the 112 Bragg peak of the different phases, the Ga content was determined. The changes in the measured peak profile de-

pending on the incident angle indicated a strong Ga content within the layer. Detailed analyses have revealed that the absorber surface is Ga rich (x_{Ga} ~ 40%) and the Ga content decreases to x_{Ga} ~ 17% on the Mo back contact within the layer.

(2) Structural investigations of the first stage of the Cu(In,Ga)Se_2 three-stage process

A well established method, the three-stage co-evaporation process, was used for growing polycrystalline Cu(In,Ga)Se_2 (CIGSe) thin films, used as absorber layers in thin film solar cells. In the first stage, In, Ga and Se were deposited as a Ga-Se/In-Se/Ga-Se/InSe sequence to form the precursor layer. The structure and microstructure of the subsequent phases, which depend on the substrate temperature, were studied by GIXRD [2]. The diffraction pattern showed the existence of $(Ga_xIn_{1-x})_2Se_3$ mixed crystals with varying Ga content. By increasing the substrate temperature the intermixing of In and Ga was also increased (see Figure 3). In addition to the Bragg peaks of γ-In_2Se_3, it was possible to identify $(Ga_xIn_{1-x})_2Se_3$. Moreover, changes in the microstructure were revealed depending on the substrate temperature: At a low substrate temperature the γ-In_2Se_3 layer was microcrystalline; with increasing temperature the size of the crystallites increased. Thus it became obvious that in a standard three-stage process the deposition sequence Ga-Se/In-Se/Ga-Se/InSe in the first stage does not result in a stack of γ-In_2Se_3 and Ga_2Se_3. The precursor is formed by $(Ga_xIn_{1-x})_2Se_3$ mixed crystals with varying Ga content resulting in a thin film with a slight Ga gradient.

(3) Structure of sputtered In_xS_y buffer layers in Cu(In,Ga)Se_2 thin-film solar cells

In_xS_y layers – used as a buffer in CIGSe thin-film solar cells – were deposited by magnetron sputtering on CIGSe/Mo/glass stacks at three different temperatures (without any heating, at 230°C and at 340°C) and studied by means of GIXRD [2]. The GIXRD diffraction pattern showed that with increasing deposition temperature, new phases were formed by the diffusion of Cu and Ga from CIGSe into In_xS_y and the diffusion of In from In_xS_y into CIGSe. These phases, identified by their Bragg peaks, are the spinel-type phase $CuIn_5S_8$ and the ordered vacancy compounds (OVC) $Cu(In_{1-x}Ga_x)_5Se_8$ and $CuGa_3Se_5$. The latter exhibits a microcrystalline structure which causes a broadening of the corresponding Bragg peaks. GIXRD measurements taken at different incident angles (0.5°-5°) revealed the stacking of the different phases according to $CuIn_5S_8$ / $CuGa_3Se_5$ / $Cu(In_{1-x}Ga_x)_5Se_8$/ $Cu(In,Ga)Se_2$/Mo (Figure 4). Moreover, by evaluating the 112 Bragg peak position and applying Vegard's rule, the Ga content of the $Cu(In_{1-x}Ga_x)Se_2$ phase and the $Cu(In_{1-x}Ga_x)_5Se_8$ phase was determined to be x~31% and x~ 28%, respectively.

These are just a few examples of a number of different applications of the GIXRD technique which demonstrate the variety of information on phase content, structure, microstructure and even chemical composition which can be gained by careful analysis of GIXRD data.

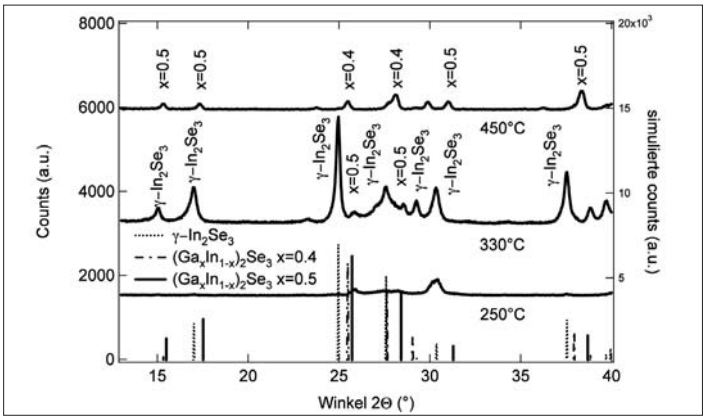

Fig. 3: GIXRD-measurements (incident angle 2°) of In-Se/Ga-Se layers deposited at various substrate temperatures. The Bragg peaks of γ-In_2Se_3 and $(Ga_xIn_{1-x})_2Se_3$ (x=0.4 and 0.5) are indicated.

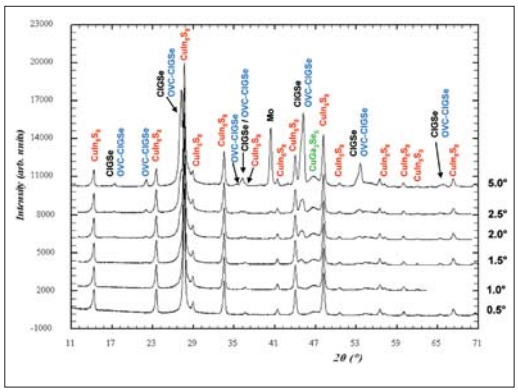

Fig. 4: GIXRD pattern of the 340 °C sample, measured at various incident angles (values given on the right). Peaks attributed to various phases are indicated.

[1] Ch. Kaufmann, R. Caballero, T. Unold, R. Hesse, S. Schorr, M. Nichterwitz, H.-W. Schock, Sol. En. Mat. Sol. Cells (2008) in press

[2] R. Hesse, R. Caballero, D. Abou-Ras, T. Unold, C. A. Kaufmann, H.-W. Schock, SPIE Optics+Photonics, San Diego (2007)

[3] D. Abou-Ras, G. Kostorz, D. Hariskos, R. Menner, M. Powalla, S. Schorr, and A.N. Tiwari, Thin Solid Films 517 (8) (2009) 2792-2798.

Corresponding author:
Susan Schorr
susan.schorr@helmholtz-berlin.de

We have take off: $Cu(In,Ga)Se_2$ thin film solar cells – recent developments in space applications

C.A. Kaufmann, R. Caballero, R. Scheer, P. Körber, H.-W. Schock (HZB-SE3), R. Klenk (HZB-SE2)
G. Oomen, C. Hofkamp (Dutch Space B.V., P.O.Box 32070, 2303 DB Leiden, the Netherlands)
■ **Helmholtz-Zentrum Berlin für Materialien und Energie, Berlin, Germany**

Over the last few years, flexible $Cu(In,Ga)Se_2$ (CIGSe) thin film technologies have attracted increasing interest due to their potential for space applications. What is behind it? The answer is

– high power-to-weight ratio, i.e. the technology is very light,
– high packing density,
– tolerance of space radiation that is superior to that of crystalline space technologies for photovoltaic power generation [1]
– and low cost.

The Helmholtz-Zentrum Berlin, formerly Hahn-Meitner-Institut Berlin, has been working on the development of flexible CIGSe thin film solar cells on titanium foil substrates for space and terrestrial applications [2,3] since 2002. This work has largely been funded by ESA and undertaken in collaboration with the Zentrum für Sonnenenergie- und Wasserstoff-Forschung Baden-Württemberg (ZSW) in Stuttgart, and Dutch Space B.V. in the Netherlands. A single solar cell device (27.1 cm^2, AM1.5, without anti-reflective coating) with conversion efficiency of 15% [2] and a mini-module (4 cells, aperture area 108.4 cm^2, AM1.5, without anti-reflective coating) with aperture efficiency of 12.6% [3] have been demonstrated, in both cases on titanium foil substrates. On a smaller scale, we have made devices in our labs with conversion efficiency of 17% (0.5cm^2, AM1.5, without anti-reflective coating) .

After laborious testing of the CIGSe thin film devices in phase 3 of the ESA TFSC programme, the solar cells were finally deemed fit to be included on a test flight of the Delfi-C3 mission at an orbit of 630 km [4]. This mission was extremely important not only as a test for CIGSe thin film technology on titanium foil itself, but also for the interconnection technology and a high-ε coating that were both specifically developed for devices on flexible conductive substrates by Dutch Space. Figure 1 shows a blow-up schematic diagram of the mini-module assembly, of which 4 have been integrated into the Delfi-C3 micro satellite. Launched on 28 April 2008, the mission has been a complete success so far and the solar cells are in perfect working order at the time of writing this article (Nov 08). About 150,000 sets of I-V curves have been recorded, one of which is shown in Figure 2. Although it would be critical for further evaluation to ascertain the in-flight AM0 efficiency of the mini-modules in space, this is difficult to do: Delfi-C3 is a tumbling satellite and it is not easy to determine whether the solar cell surfaces are oriented towards the sun. Furthermore, it is also necessary to take account of albedo-earth shine, the brightness of the earth.

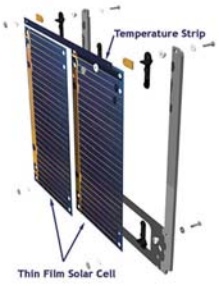

Fig. 1: Blow-up schematic diagram of the CIGSe thin film solar cell mini-module assembly as flown on Delfi-C3 (the temperature strip determines the temperature of the device).

Recent developments in the area of epitaxially grown triple junction (3J) solar cells, based on III-V compounds, have shown the feasibility of greatly reducing the thickness of single 3J devices while maintaining an efficiency level approaching 30%. Although these thin single cells are flexible in principle, they still need support structures to ensure the system's stability during launching and protection against radiation. Despite this, ESA considers this development so promising that it has called a halt to further funding of CIGSe based technology development [5]. However, CIGSe technology, as flown on Delfi-C3, will have another chance to be tested in space when it is incorporated in the MISSE7 mission. It will fly on board the ISS for a year, starting in 2009. This has the advantage that after the flight the assembly will be returned to earth and can be analysed with a view to further optimisation.

Meanwhile, HZB has been working on the transfer of CIGSe technology to a polyimide (PI) substrate. This work is funded by Deutsche Luft- und Raumfahrt (DLR) and is being conducted together with the scientific partner, ZSW, and the industrial partners, Solarion AG, Leipzig and HTS GmbH, Dresden. CIGSe solar cells consist of a layer stack in the order Mo/CIGSe/CdS/i-ZnO/ZnO:Al. Molybdenum is the back contact material. CdS, deposited by chemical bath deposition, is used as a buffer layer between the p-type semiconductor CIGSe absorber layer and the n-type semiconductor i-ZnO/ZnO:Al transparent front contact. The devices are generally completed with a Ni/Al front contact grid which is deposited onto the ZnO front contact in

order to facilitate current collection. Prior to CIGSe deposition a NaF precursor layer is evaporated onto the Mo back contact. The challenge posed by using PI as substrate foil is the large thermal expansion coefficient of the material and in particular its low stability at temperatures above 420°C. On titanium and glass substrates high efficiency CIGSe absorber layers are generally deposited at temperatures above 500°C. In order to optimise the CIGSe growth process for low temperatures, it was found that the amount of Na was critical. At low growth temperatures the sodium influences the layer morphology, the In-Ga interdiffusion during the growth process and the charge density of the resulting CIGSe absorber layer [6]. Figure 3 shows a cross-sectional scanning electron microscope image of just such a CIGSe thin film solar cell on a PI substrate. The whole solar cell is only a few micrometres thick. By optimising both the sodium content and the growth temperature it has been possible to achieve efficiency of, so far, up to 13.6% for the total area on a 0.5 cm^2 device under AM1.5 illumination and without an anti-reflective (AR) coating (see Table 1). The current record efficiency for low temperature devices on PI foil is 14.1% (total area) which was grown without sodium during CIGSe deposition. Here the Na has been added via a post deposition process [7]. Introducing the sodium after the CIGSe absorber has been finished is known to be beneficial as the layer formation process is not impeded by the presence of Na. The collaborative project on the development of flexible CIGSe technology on PI foils is aiming to produce highly efficient, large area, single solar cell devices of 4×8 cm^2 in order to demonstrate the future low cost potential of flexible CIGSe solar cell technology - not only for space but also for terrestrial applications.

[1] A. Messenger, R. Walters, G. Summers, T. Morton, G. La Roche, C. Signorini, O. Anzawa and S. Matsuda, A Displacement Damage Dose Analysis of the Comets and Equator-S Space Solar Cell Flight Experiments, Proc. 16th European PVSEC, 1-5 May 2000, Glasgow, United Kingdom

[2] A. Neisser, C.A. Kaufmann, R. Klenk, R. Scheer, H.-W. Schock, M.A. Kroon, G. Oomen, D. Herrmann, F. Kessler, M. Powalla, Flexible Solar Cells for Space: A new Development based on Chalcopyrite Thin Films, Proc. 7th ESPC, 9-13 May 2005, Stresa, Italy

[3] C.A. Kaufmann, A. Neisser, K. Sakurai, P. Körber, H.-W. Schock, R. Klenk, M.C. Lux-Steiner, A flexible, $Cu(In,Ga)Se_2$ based, thin film solar cell module, in Annual Report 2005 – Selected Results, Hahn-Meitner-Insitut Berlin (HMI-B 608), Berlin, 2006

[4] http://www.delfic3.nl

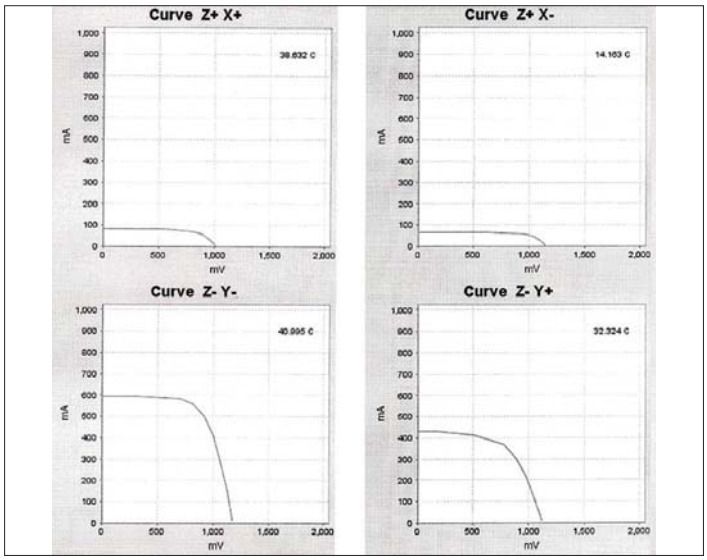

Fig. 2: A full set of I-V curves, of which around 150,000 have been recorded; Z and X indicate the position of the mini-module; the module temperature as indicated by the temperature strip is also given.

[5] C. Signorini, T. Blancquaert, G. Dudley, L. Gerlach, M. Schautz, E. Simon, F. Tonicello, Power and Energy Conversion Technology: ESA R&D Roadmap and Applications, Proc. 8th ESPC, 14-19 Sep 2008, Constance, Germany

[6] R. Caballero, C.A. Kaufmann, T. Eisenbarth, T. Unold, S. Schorr, R. Hesse, R. Klenk and H.-W. Schock, The effect of a NaF precursor on low temperature growth of CIGS thin film solar cells on polyimide substrates, Proc. 16th ICTMC, 15-19 Sep 2008, Berlin, Germany - accepted for publication in Physica Status Solidi

[7] D. Rudmann, D. Brémaud, H. Zogg and A.N. Tiwari, Na incorporation into Cu(In,Ga)Se2 for high-efficiency flexible solar cells on polymer foils, Journal of Applied Physics 97, 084903

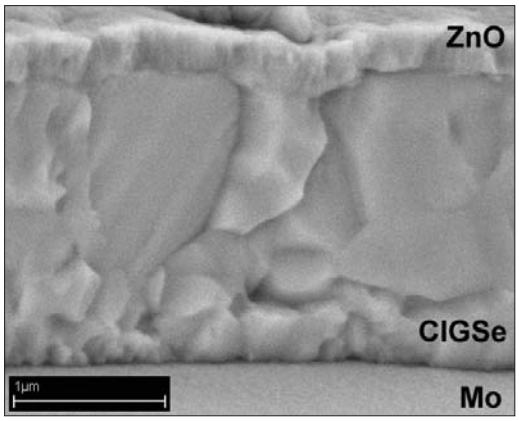

Fig. 3: X-sectional scanning electron microscopy image of the layer structure of a CIGSe thin film solar cell deposited onto PI foil.

Corresponding author:
C.A. Kaufmann
kaufmann@helmholtz-berlin.de

In-situ control and verification of single-domain III-V growth on Si substrates

H. Döscher1, T. Hannappel1, B. Kunert2, K. Volz2, W. Stolz2
■ 1 Helmholtz-Zentrum Berlin für Materialien und Energie, Berlin, Germany
■ 2 Philipps-Universität, Marburg, Germany

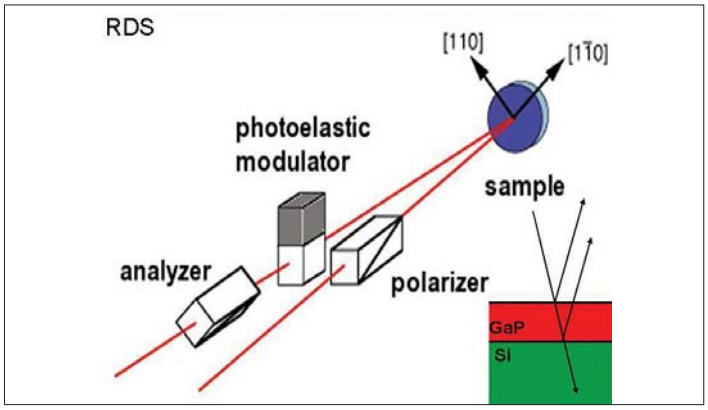

Fig. 1: Measurement principle for RAS. The sample's surface is illuminated in normal incidence geometry with light polarised in two perpendicular directions from the surface. The observed difference in reflection is extremely surface sensitive for all materials with inversion symmetry in the lattice structure.

This work on the in-situ quantification of the surface domain structure of thin gallium phosphide (GaP) films grown on Si(100) [1] was recently awarded, by an independent committee, the 'LayTec In-situ Monitoring Award'. The work was the result of a close collaboration between Helmholtz-Zentrum Berlin für Materialien und Energie and Philipps-Universität, Marburg.

In-situ reflectance anisotropy spectroscopy (RAS, Fig.1) was used for the quantification of antiphase domains on the surfaces of thin GaP films, deposited onto Si(100) by metal-organic vapour phase epitaxy (MOVPE). For the first time, single-domain III-V growth on silicon (100) was determined via the analysis of RAS peak intensities in reference to homoepitaxially grown GaP(100). The in-situ signals were directly correlated (benchmarked) to surface sensitive, UHV-based tools. More specifically, the surfaces were observed with scanning tunnelling microscopy (STM), low energy electron diffraction (LEED) and photoemission (PES). Both pre-processed Si(100) substrates and MOVPE as-grown GaP/Si(100) films were also characterised ex-situ, by atomic force microscopy, to identify the formation of mono- and diatomic surface steps and to analyse of the domain distribution, respectively.

The integration of III-V-based opto-electronic devices on to the standard silicon (100) substrates that are used by the established micro-electronic industry is considered to be a major challenge for the semiconductor industry. In photovoltaics, this would allow the combination of high efficiency, multi-junction solar cells with Si(100)-substrates, which would be both competitive and superior in many technological aspects. In addition, there is generally a strong scientific and technological interest in the realisation of III-V semiconductor hetero-epitaxy on silicon substrates, in particular, the industrial scalability of the metal-organic vapour phase epitaxy (MOVPE) technique.

However, the material properties of III-V semiconductors are especially susceptible to lattice defects, and the growth on a non-polar substrate, like silicon, creates additional defect mechanisms [2]. In particular, anti-phase domains (APDs) are typically initiated at the III-V/Si(100) interface during hetero-epitaxial deposition and usually propagate with growth. For the specific study of this crucial defect mechanism, pseudomorphic GaP films were grown on Si(100) by MOVPE and characterised by optical in-situ spectroscopy. Well-ordered GaP/ Si(100) surfaces formed by hetero-epitaxial deposition could potentially be used as quasi-substrates, for the integration of III-V-based devices on Si(100) substrates. An in-situ technique for reliably determining the single-domain character of large-area surfaces is essential for the application of GaP/Si(100) quasi-substrates. In normal incidence geometry, RAS shows the normalised difference in the reflection of light, polarised in two perpendicular directions from the surface, $\Delta r / r$ (Figure1). In materials with inversion symmetry, the bulk does not contribute to the sample's anisotropy and in these cases it causes the desired surface sensitivity of RAS. Different terminations have been identified and were assigned to characteristic RD spectra (Figure 2a) [3]. In the current experiment, the atomic structure of the standard GaP(100) surface was essentially formed by buckled P dimers stabilised by a hydrogen atom (Figure 2b). On the Si(100) surfaces even- and odd-numbered atomic steps can occur resulting either in a (2x1)/(1x2) two-domain surface or a single domai- surface reconstruction [4].

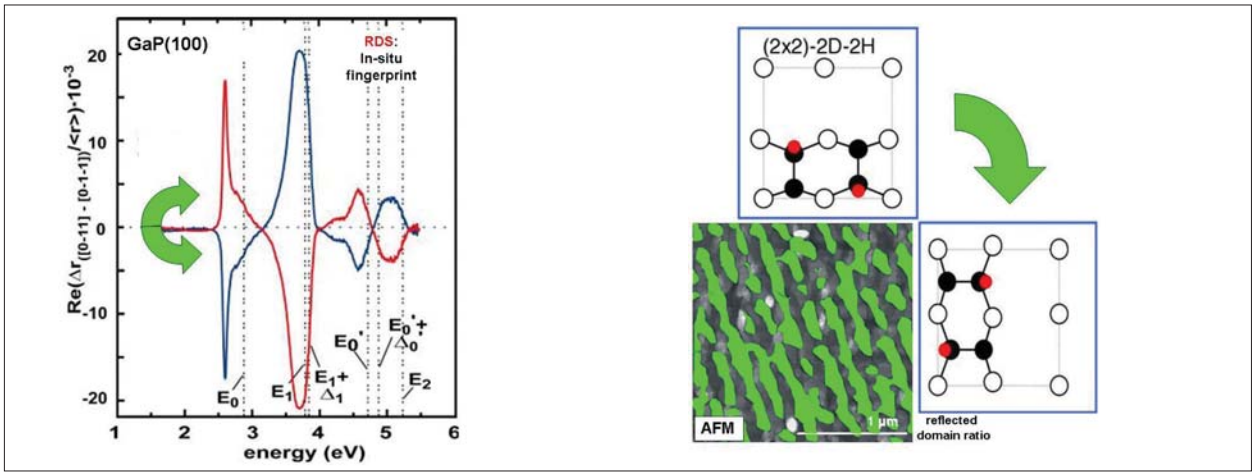

Fig. 2a: In-situ RAS signal of the P-rich GaP(100) surface at 20K. The spectrum shows two extremely intense structures peaking at about 2.6 eV and 3.8 eV, respectively (blue curve). The signal is inverted if the surface directions are exchanged against its definition (red curve).

Fig. 2b: Atomic structure of standard GaP and AFM picture of a hetero-epitaxial GaP film deposited on Si(100). Standard preparation leads to the extensive formation of defective anti-phase domains (coloured in green). In the surface areas, the unit cell of the surface reconstruction is rotated by 90°.

In this experiment, RAS was successfully employed to measure the APD density over the entire spot size (about 0.5 cm^2) by correlating the RAS "fingerprints" and the corresponding surface reconstruction domains under MOCVD growth conditions. According to its definition, RAS signals originating from alternating, vertically aligned domains (e.g., APDs) are reversed. Thus, degradation of the RAS signal intensity occurs corresponding to the relative amount of APDs on the surface of the deposited film. In contrast, on Si(100) that is preferentially prepared with biatomic steps, the GaP/ Si(100) surface produces a far less distorted RAS signal with significantly higher amplitude. Hence, the peak intensity at 3.4 eV (Figure 3) correlates directly to the density of APDs. For GaP/Si(100) growth, the maximum RAS amplitude corresponds to a 100% single domain GaP surface with the RAS value of zero indicating a 50:50% distribution for both types of surface domains. These results also provide information about the initial Si(100) surface reconstruction domain ratio prior to GaP epitaxy, as the atomic structure of the Si substrate is a major origin of the detected anti-phase disorder.

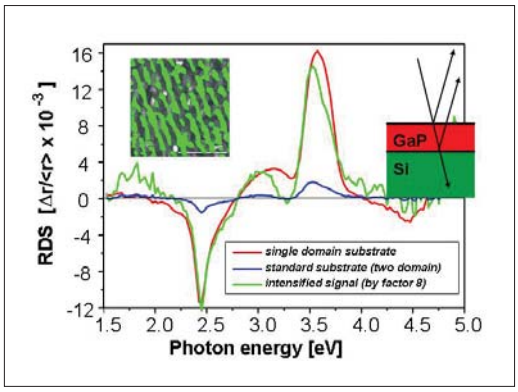

Fig. 3: In-situ RAS/RDS signal for GaP/Si(100) thin films. After an advanced preparation procedure the surface is free of defective anti-phase domains (APDs) as proven by the intense signal (red curve). Samples from standard preparation that contain lots of APDs only give a poor signal (blue curve). Its amplification still reproduces the characteristic RDS peaks and is used for the in-situ quantification of the APD-content.

In summary, single domain preparation of hetero-epitaxially grown III-V films was demonstrated, in-situ, as being a fundamental contribution to future integration of III-V semiconductors into Si technology. The key issue, that was addressed in this joint result, is the quantitative in-situ measurement of the density of anti-phase domains (APDs) during III-V-epitaxy on Si(100) employing RAS. The analysis of in-situ RAS peak intensities was used for a quantitative measurement of the APD concentration of thin GaP(100) films grown on Si(100) substrates.

[1] H. Döscher, T. Hannappel et al., Appl. Phys Lett 93 (2008) 172110.
[2] H. Kroemer, J. Cryst. Growth 81 (1987) 193.
[3] L. Töben, T. Hannappel et al., Surf. Sci. Lett. 494 (2001) L755.
[4] D. J. Chadi, Phys. Rev. Lett. 59 (1987) 1691.

Corresponding author:
Thomas Hannappel
hannappel@helmholtz-berlin.de

The Ultrafast Temporal and Spectral Characterisation of Electron Injection in ZnO and TiO_2 based hybrid systems

J. M. Szarko, A. Neubauer, A. Bartelt, L. Socaciu-Siebert, F. Birkner, K. Schwarzburg, T. Hannappel, R. Eichberger
■ Helmholtz-Zentrum Berlin für Materialien und Energie, Berlin, Germany

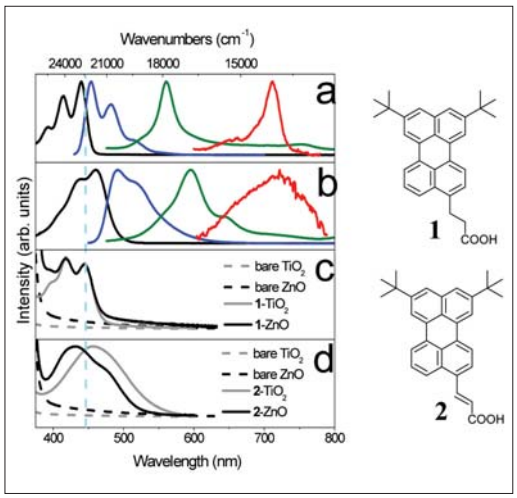

Fig. 1a,b: Absorption and emission spectra of molecules 1 (a) and 2 (b): ground state absorption in methanol (—), emission spectra in methanol (—), cation absorption spectra prepared in concentrated H_2SO_4 (—) and excited state absorption spectra in methanol (—). (c, d) Ground state absorption spectra of molecules 1 (c) and 2 (d) attached to ZnO and TiO_2 colloids. The UV/Vis absorption spectra of the unsensitised colloidal films of ZnO and TiO_2 are also shown. The blue dotted line at 445 nm denotes the central position of the pump beam in the fs Transient Absorption experiment.

ZnO is a promising semiconductor material for charge transport electrodes in low-cost hybrid nano-composite solar cells and may, in the future, eventually replace the widely used colloidal TiO_2 in such devices [1]. ZnO shows enhanced structural and electronic features that could be advantageous for future dye sensitised solar cells (DSSCs). For example, by separating the photo-excited electrons from the cationic dye molecule more quickly, DSSCs made from ZnO nanorods have shown faster electron transport rates which could lead to higher efficiencies. However, TiO_2 DSSCs are currently the most efficient hybrid solar cells with a conversion efficiency of over 10% [2], whereas ZnO based DSSC efficiencies remain below 6% [3]. Charge separation at the dye/ZnO interface is poorly understood, and reported injection dynamics at ZnO nm-structured electrodes range from hundreds of fs to hundreds of ps and are much slower when compared to TiO_2 [4].

In order to gain a more fundamental insight into the dynamics of the photo-induced electron transfer processes at dye sensitised nanocrystalline ZnO and at TiO_2 electrodes, the two systems were studied and directly compared using Femtosecond Transient Absorption in ultra-high vacuum. Two perylene derivatives were used as model sensitiser chromophores, chemisorbed onto the ZnO and TiO_2 semiconductor surfaces either by a propionic acid (-CH_2-CH_2-COOH) (molecule 1), or an acrylic acid (-CH)CH-COOH) (molecule 2), which respectively discriminated between weak and strong electronic coupling. The molecules differ only in one unsaturated bond that delocalises the excited-state electron over the entire acrylic acid bridge and therefore couples it more closely to the colloidal surface.

The steady state absorption spectra of the ground, cationic and excited states of the perylene derivatives in solution and the ground state absorption of the four dye/semiconductor systems are depicted in Figure 1.

Figure 1c shows the linear ground-state absorption spectra of 1-TiO_2 and 1-ZnO that are similar to the ground state spectra of the molecules in solution. The vibronic peaks are slightly broadened, which is characteristic for electronic coupling and ultrafast electron injection. The ground-state absorption spectra of molecule 2 attached to TiO_2 or ZnO colloids (Figure 1d) do not show the vibronic progression, which indicates an even stronger electronic coupling and faster electron injection. This trend is confirmed by the fs pump-probe measurements exciting the perylene dyes at 440 nm and probing with an ultra-short white-light continuum. The experiment simultaneously monitored the evolution of

the cationic and excited state dynamics in a broad spectral window (Figures 2 and 3).

The transient absorption spectra for the systems 1-ZnO and 2-ZnO are characterised by three main components (Figure 2). The area from 630-750 nm shows an instantaneous rise-time due to the excited-state species that decreases in a time window from 100 fs to 1 ps. The 550-620 nm region shows an increase in time due to the rise of the cationic signal, as the electron is transferred from the molecule to the semiconductor. The measured time constants for the cationic state rises and for the excited state decays at early times (ranging from 200 to 250 fs for the two systems), showing a complimentary behaviour suggestive of direct electron transfer from the excited state of the adsorbed molecule into the semiconductor. This is further supported by an isosbestic point observed at 625 nm, indicating that only two species are present in the depicted time range. The negative signal from 530-550 nm is ascribed to the ground state bleaching of the chromophore quenched by ultrafast electron transfer.

The transient absorption spectra of 1-TiO_2 (Figure 3a) look similar to the 1-ZnO spectra, but the cationic peak for the 1-TiO_2 system is more pronounced due to a larger percentage of the excited-state being already depleted within the duration of the exciting laser pulse, due to faster electron injection. The injection time is much shorter for this system, being 57 fs, as previously reported [5]. The transient absorption spectrum of 2-TiO_2 (Figure 3b) shows a large negative signal at 530-550 nm (ground-state bleaching) which is attributed to an ultrafast direct charge transfer that competes with the excited state at 710 nm. The cationic state rise-time in this system was previously reported as 10 fs [5].

In conclusion, the injection dynamics of the ZnO based systems was found to be slower compared to the TiO_2 counterparts but show a similar trend in dynamics making it a good candidate for DSSCs. The injection times of around 200 fs for the ZnO based systems are, overall, the shortest for any dye-sensitised ZnO colloid system accurately time-resolved so far.

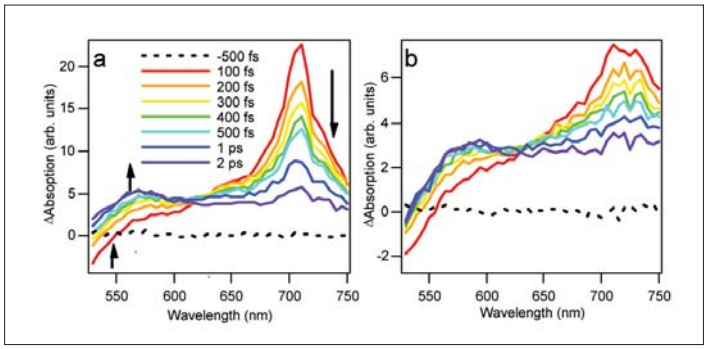

Fig. 2: Transient absorption spectra of 1-ZnO (a) and 2-ZnO (b) showing cationic and excited state dynamics

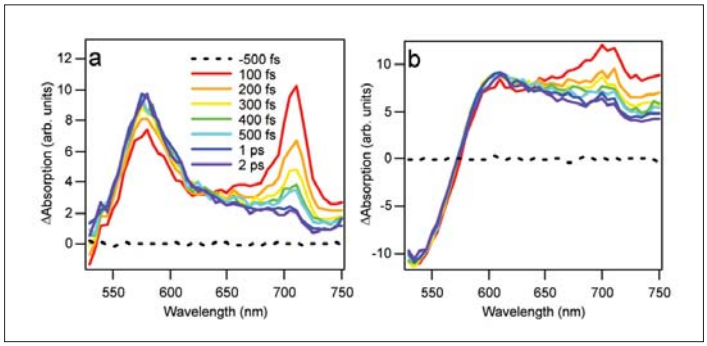

Fig. 3: Transient absorption spectra of 1-TiO_2 (a) and 2-TiO_2 (b) showing cationic and excited state dynamics.

[1] M. Law, L. E. Greene, J. C. Johnson, R. Saykally, P. Yang, Nat. Mater. 4, 455 (2005)
[2] M. Grätzel, Nature 414, 338 (2001)
[3] K. Keis, E. Magnusson, H. Lindström, S. Lindquist, A. Hagfeldt, Sol. Energ. Mat. Sol. C. 73, 51 (2002)
[4] J. M. Szarko, A. Neubauer, A. Bartelt, L. Socaciu-Siebert, F. Birkner, K. Schwarzburg, T. Hannappel, R. Eichberger J. Phys. Chem. C 112, 10542 (2008)
[5] Ernstorfer, R., Ph.D. Thesis, Freie Universität Berlin, 2004

Corresponding author:
R. Eichberger
eichberger@helmholtz-berlin.de

Development of a membrane for photo-induced hydrogen generation

S. Fiechter, H.J. Lewerenz, P. Bogdanoff
Helmholtz-Zentrum Berlin für Materialien und Energie, Berlin, Germany

It is well known that solar cells are able to convert sunlight into electrical energy. As sunlight is not permanently available, however, a part of this energy has to be stored, for example, by using rechargeable lithium batteries. Another option is the storage of chemical energy in the form of hydrogen, produced by water splitting via solar energy. Compared with battery systems and hydrocarbons such as benzene or diesel, hydrogen has an extraordinarily high energy density and can be stored in pressurised bottles or as metal hydrides. The low weight of hydrogen and its high energy content also make it attractive as fuel for mobile applications. By comparison: 6kg H_2 correspond to 200kWh of chemical energy while the weight of a 540kg lithium ion battery is needed to deliver 100kWh of electrical energy. Subsequent conversion of this chemical energy into electricity by a fuel cell system (typical efficiency: 50%) means that the overall energy conversion efficiencies are comparable. Since cheap metal hydrides are not yet available for technical application, compressed hydrogen has to be stored in dedicated containers. Based on present technology, the system weight of 125kg (H_2) still compares favourably with a battery system weighing 830kg.

Thus to store chemical energy in the form of hydrogen efficiently, novel storage systems (e.g. metal hydrides, methanol) as well as efficient energy converting systems have to be developed in order to use sunlight as a virtually inexhaustible, renewable energy source. Therefore to envisage a future hydrogen economy, efficient catalysts and efficient energy converting devices have to be developed. In contrast to the process of photosynthesis in which non-noble metal catalysts (Mn- and Fe-Ni-clusters) convert CO_2 and water into O_2 and hydrocarbons, current artificial systems - combining solar cells with an electrolyser - employ platinum and ruthenium oxide in the process of water splitting. One of the intriguing research goals is therefore the mimicking of the thylakoid membrane in plants. Thus the development of an artificial "water splitting membrane", allowing the direct conversion of sunlight into hydrogen and oxygen, is of particularly high importance. Approaches that include organic and inorganic systems to achieve this goal have been proposed. The basic problems relate to the stability of organic artificial systems and so we have introduced a design that uses hitherto inorganic components: a thin film photovoltaic monolithic, so called back-to-back tandem structure with integrated catalysts at the photocathode (hydrogen generation) and the photoanode side (oxygen generation) to facilitate water splitting by sunlight (Figure 1).

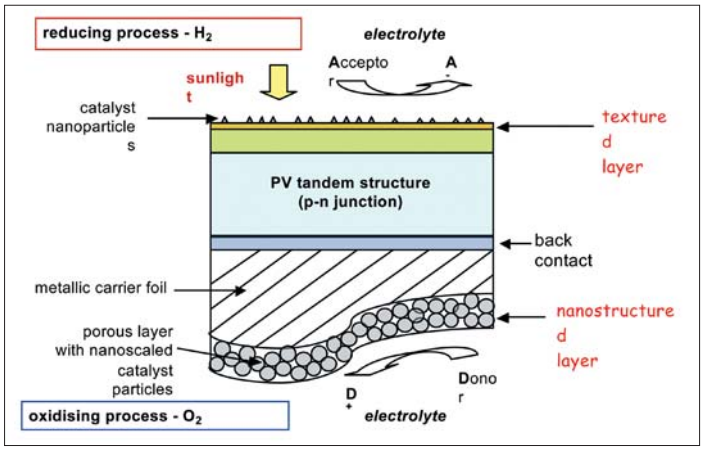

Fig. 1: Schematic cross section of a water splitting membrane combining a thin film tandem solar cell structure with nano-scaled catalysts to generate hydrogen at the cathode and oxygen at the anode side under irradiation of the device with sunlight after immersion in water (adapted from [2]).

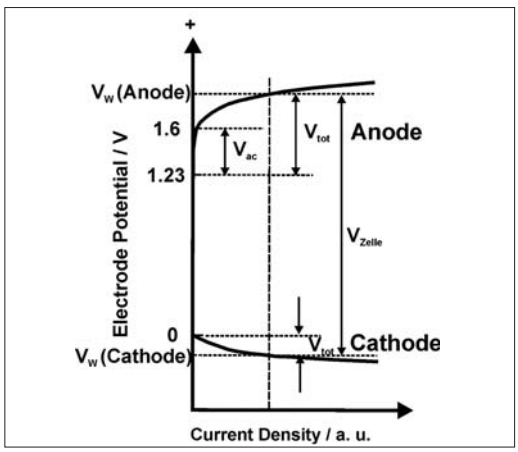

Fig. 2: Schematic representation of the dependency of the current density from the applied potentials Vw on the cathode and the anode sides. The I-U curves shown increase exponentially with increasing current density. The current density particularly increases on the anode side where oxygen evolution occurs during water splitting.

The concept of an integrated monolithic photoelectrochemical-photovoltaic design, splitting water directly upon illumination, was realized for the first time in 1998 by Khaselev and Turner using a high efficiency GaAs-GaInP$_2$-based tandem structure [1]. At the Helmholtz-Zentrum für Materialien und Energie a first prototype has been constructed by Neumann et al. [2-3] using a chalcopyrite thin film solar cell absorber with a niobium-doped TiO_2 emitter layer and adsorbed platinum particles at the cathode. At the photoanode, a porous TiO_2 layer was used. The photovoltage achieved by the illuminated chalcopyrite solar cell was too small to split water directly because of the small solar photon flux in the spectral region where TiO_2 is absorbed. In order to test the concept further, more intense UV radiation was applied to the anode side to precipitate the process, which did result in water splitting. The main reasons for promoting the general concept of monolithically integrated systems rather than a separate photovoltaic-electrolyser approach are that it seems to promise more technological applications and lower costs [4-5].

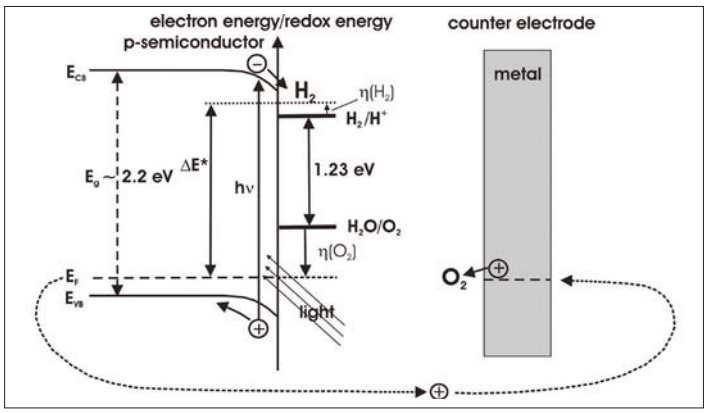

Fig. 2: Overall energetic restraints for the evolution of H_2 and O_2 at semiconductor-electrolyte interfaces; η denotes the overpotentials (VW) in electrochemical notation, ΔE* is the cell voltage V_{cell} of Figure 2. The system drawn uses a *p*-type semiconductor at which H_2 evolution takes place by electron injection into the electrolyte from the conduction band. O_2 evolution energies are included to visualise the overall energetic situation.

The thermodynamic potential of water dissociation reaction according to the chemical equation

$$H_2O\ (liquid) \rightarrow H_2\ (gaseous) + \frac{1}{2}O_2\ (gaseous)$$

is given by the electromotoric force $V_0 = -\frac{\Delta G^0}{nF}$,

where the free Gibb´s enthalpy ΔG^0 is defined by $\Delta G^0 = \Delta H^0 - T\Delta S^0$. At pH = 0 and T = 25°C a value of V_0 = 1.23V is obtained. The main challenges besides the surface stability of the light absorbing material and the stability of the nano-scaled catalysts are posed by so-called overvoltages. In particular, the overvoltage on the anode side, where four electrons have to be transferred via the electrode–electrolyte interface to oxidise two water molecules in order to obtain one O_2 molecule, tends to be high, reaching values of between 0.4 and 0.6V. The size of this value strongly depends on the properties of the catalyst used. Because these overvoltages are an inherent limiting parameter of the process, they affect the efficiency $\eta_{photoelectrolysis} = \eta_{PV} \times \eta_{electrolysis}$ with $\eta = \frac{1.23V}{V_{cell}}$ of the process substantially.

Figure 2 shows a schematic energy diagram illustrating the dependency of the working potentials VW at the electrodes of half cells from the current density. Although no numbers are given in the diagram a current density of e.g. 10mAcm^{-2} can necessitate a potential V_{cell} which is 30% to 50% higher than the thermodynamic value of 1.23V.
Application of these considerations to the semiconductor-electrolyte phase boundary demands that the absolute positions of the semiconductor conduction and valence bands are located so that the reduction reaction of protons to H_2 can proceed from the conduction band and the valence band is energetically located below the potential for anodic water decomposition. In addition, with semiconductors, a driving force for charge separation as reflected in the energy band bending is required and resistive losses in the electrolyte and series resistance also have to be taken into account. This adds a value up to about 2.2eV - 2.3eV for the energy gap of a suitable semiconductor. The respective energy diagram is shown in Figure 3 together with the basic fuel generation reaction schemes. With a limiting energy gap of ~2.3eV, the theoretical solar energy conversion efficiency for a single junction is in the range of 14% under AM 1.5 conditions, making tandem structures that evolve hydrogen and O_2 more promising with respect to higher system efficiencies [6].

[1] O. Khaselev, J, A. Turner; Science 280 (1998) 425.
[2] H.Tributsch, B. Neumann; International Journal of Hydrogen Energy 32 (2007) 2679.
[3] B. Neumann,F. Birau, B. Johnson, C. A. Kaufmann, K. Ellmer, H. Tributsch; phys. stat. sol. B 245 (2008) 1849.
[4] N.S. Lewis, Nature 414 (2001) 589.
[5] A.J. Bard, M.A. Fox, Acc. Chem. Res. 28 (1995) 141.
[6] C.A. Grimes, O.K. Varghese, S. Ranjan; Light, Water, Hydrogen, The Solar Generation of Hydrogen by Water Photoelectrolysis, Springer, Berlin, 2007.

Corresponding author:
S. Fiechter
fiechter@helmholtz-berlin.de

Preparation of photoactive WS_2 nanosheets by rapid crystallisation of amorphous WS_{3+x} films: an in situ, real-time X-ray diffraction study

Stephan Brunken[1], Rainald Mientus[2], Klaus Ellmer[1]
■ 1 Helmholtz-Zentrum Berlin für Materialien und Energie, Berlin, Germany
■ 2 Opto-Transmitter-Umweltschutz-Technologie e.V., Berlin, Germany

Tungsten disulphide (WS_2) belongs to the class of layer-type transition metal dichalcogenides (MoS_2, WSe_2, $MoSe_2$ etc.), which have been investigated for more than 30 years as prospective absorber materials for solar cells [1]. WS_2 crystallises in a hexagonal structure and consists of S-W-S triple layers, which are stacked over each other along the c direction (Fig. 1). Whilst the bonding within the layers is covalent, the bonding between the S-W-S sandwiches (i.e. between sulphur atom planes) is of the van der Waals type (~0.15 eV/S atom). The sulphur-terminated (001) planes are nearly free of dangling bonds, allowing the preparation of good heterojunctions for solar cells of a high electronic quality. The band gap of about 1.8 eV and its very high absorption coefficient (> 10^5 cm^{-1}) makes WS_2 a candidate as absorber layer in thin film solar cells.

In this research project, the growth of WS_2 layers in the desired (001) orientation was investigated by in-situ, time-resolved energy-dispersive X-ray diffraction (EDXRD) at the synchrotron radiation source HASYLAB in Hamburg. Here a white X-ray beam (6-60 keV) is diffracted at the sample and detected by a germanium detector. The diffraction patterns were measured at a fixed diffraction angle of about 4° with time resolutions of 1-10 seconds during the growth and the crystallisation of the WS_2 films [2, 3]. In order to prepare highly (001)-textured WS_2 films, a procedure first described by the Tenne group [4] was used:

1. Deposition of a thin metal film on the substrate, for instance a nickel film of 5 to 50 nm thickness
2. Deposition of an amorphous film by reactive magnetron sputtering from a tungsten target in an Ar/H_2S gas atmosphere at temperatures <100 °C.
3. Rapid crystallisation of the amorphous $WS_{4.5}$ films to WS_2 by annealing in H_2S atmosphere of about 10 Pa.

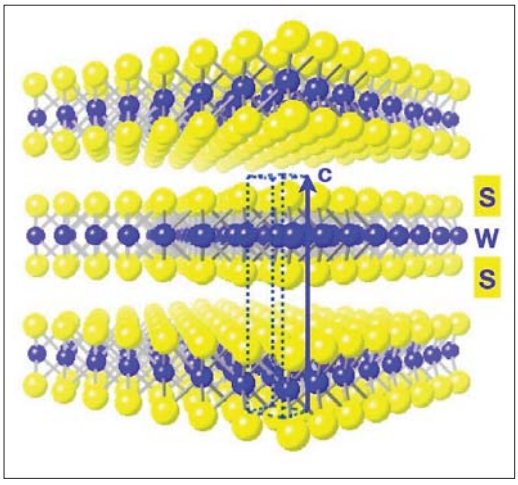

Fig. 1: Crystal structure of WS_2

The steps 2 and 3 were observed by time-resolved EDXRD and an example is shown in Figure 2, where the Ge-detector count rate (colour coded) is displayed as a function of the photon energy over the annealing time . Initially, only fluorescence peaks of nickel (K_α) and tungsten ($L_{\alpha,\beta}$) and a weak diffraction peak (111) of the nickel layer can be seen. The Ni(111) peak vanishes immediately

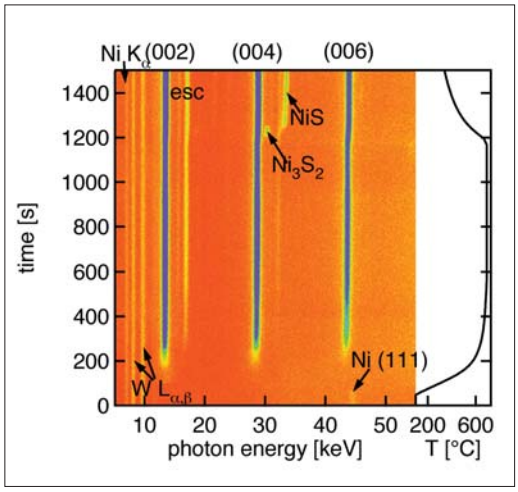

Fig. 2: In-situ real-time EDXRD during an annealing process in H_2S of an amorphous WS_{3+x} film on a nickel-coated oxidized silicon substrate. The intensity of the diffracted synchrotron light is plotted color-coded.

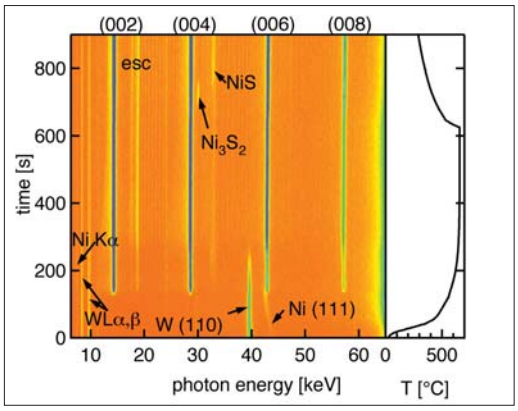

Fig. 3: In-situ real-time EDXRD of an annealing process in H_2S atmosphere of an W film on a nickel-coated oxidized silicon substrate. The intensity of diffracted synchrotron light is plotted color-coded.

after the start of heating. At this moment, $WS_{4.5}$ loses its excess sulphur and converts to WS_2, and the WS_2 (002*l*) diffraction peaks then start to grow rapidly. Using Rutherford backscattering, it was verified that the sulphur-rich $WS_{4.5}$ films are transformed to stoichiometric WS_2 crystals by evaporation of the excess sulphur at about 300 °C. During cooling the liquid nickel sulphide crystallises and forms the Ni_3S_2 phase and later the more sulphur-rich phase NiS. Nickel also induces the sulphidation of the tungsten film (Fig. 3). With increasing temperature a shift of the nickel (111) peak towards lower energies occurs, which is caused by the dissolution of tungsten in nickel. When Ni (111) disappears, WS_2 (002*l*) grow rapidly and the W (110) diffraction vanishes.

The onset of rapid crystallisation occurs at a temperature of about 650 ± 50 °C. We attribute this crystal growth to the formation of a liquid NiS_x. When oversaturation occurs, highly (001)-textured WS_2 sheets crystallise out of the liquid NiS_x nucleation seeds. As well as nickel, cobalt and palladium can also be used as crystallisation promoters [3].

The morphology of rapidly crystallised WS_2 films using a palladium (a) and a nickel (b) film for crystallisation is shown in Figure 4. The WS_2 crystallites exhibit lateral dimensions of up to 3 µm. Between the large WS_2 nanosheets, smaller NiS_x or PdS_x crystallites can be found, which mostly sit on top of the WS_2 crystallites. When the crystallisation is performed without the promotion of Ni, Co or Pd, the films exhibit very small nanocrystallites, thus proving the essential role of the metal sulphide promoters. From the in-situ, time-resolved EDXRD analysis and from morphological investigations by scanning electron microscopy, a modified model for the rapid crystallisation was established. The crystal growth involves an amorphous solid – liquid – crystalline solid process, which is similar to the well known vapour-liquid-solid process for the growth of nanorods [5].

The rapidly crystallised metal-sulphide assisted WS_2 films exhibit a hole carrier concentration in the range of 10^{17} cm^{-3} with a mobility of up to 80 cm^2/Vs at room temperature, which is in the same range as the mobility in WS_2 single crystals. These films are photoactive, which was proved by time-resolved microwave conductivity measurements with an excitation wavelength of 532 nm. This suggests that such rapidly crystallised WS_2 nanosheets should be suitable as good absorber layers in thin film solar cells, and this is to be investigated in the near future.

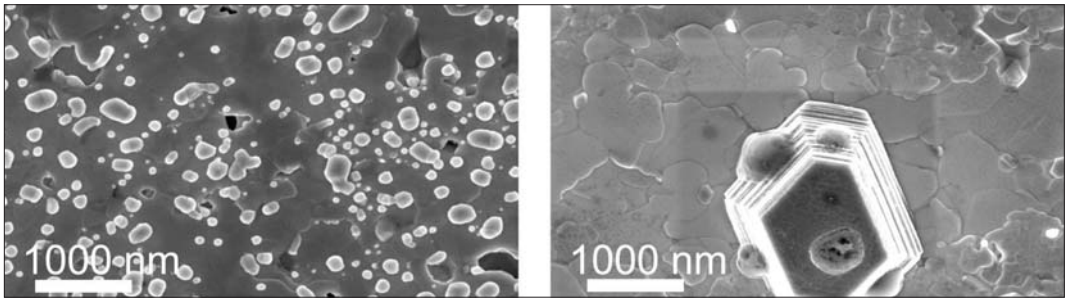

Fig. 4: Scanning electron micrographs of WS_2 films, crystallized on a (a) palladium and a (b) nickel-coated substrate.

1. Tributsch, H., Ber. Bunsenges. Phys. Chem., 1977. 81: p. 361-369.
2. Brunken, S., R. Mientus, S. Seeger and K. Ellmer, J. Appl. Phys., 2008. 103(6): p. 063501-6.
3. Ellmer, K., Phys. Stat. Sol. (b), 2008. 245(9): p. 1745.
4. Salitra, G., G. Hodes, E. Klein and R. Tenne, Thin Solid Films, 1994. 245(1-2): p. 180-185.
5. Wagner, R.S. and W.C. Ellis, Appl. Phys. Lett., 1964. **4**(5): p. 89-90.

Corresponding author:
Stephan Brunken
stephan.brunken@helmholtz-berlin.de


PILS

Facts and Figures

HMI – Facts and Figures

Founded in 1959

Locations:
Main campus: Berlin Wannsee
Second campus: Berlin-Adlershof

Member of the Helmholtz Association of German Research Centres

Legal Status: limited liability company (GmbH)

Directors:
Prof. Dr. Michael Steiner, Scientific Director
Dr. Ulrich Breuer, Administrative Director

Scientific divisions: Structural Research and Solar Energy Research

Budget:

Financed by the shareholders:
German Federal Government (90%)
City State of Berlin (10%)

In 2007/2008, the annual budget amounted to 79 Million Euros, including 5,5 Million Euros Third Party funding

Personnel:

In 2007/2008, HMI/HZB employed 679 people (full time equivalents). In addition to that, there were 62 apprentices in various professions

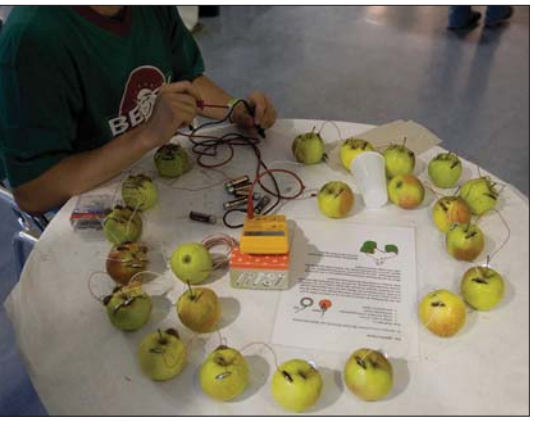

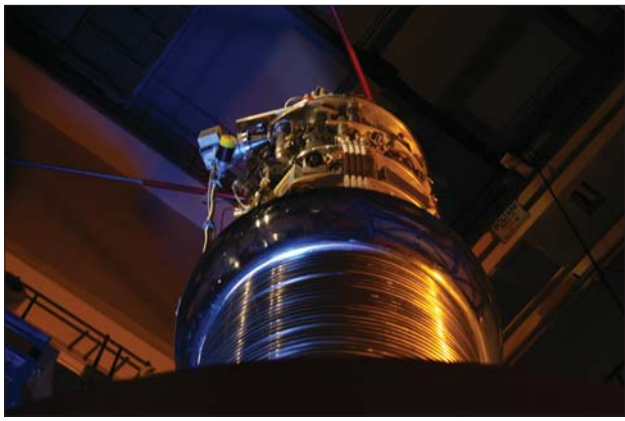

Board of Governors

Dr. Beatrix Vierkorn-Rudolph
Federal Ministry of Education and Research

Wolfgang Eckey
Senate Department for Education, Science and Research of the City State of Berlin

Dr. Bruno Broich
Technology Foundation Berlin

Dr. Jan Grapentin
Federal Ministry of Education and Research

Hans Jürgen Hardt
Federal Ministry of Finance

Hans-Jürgen Reil
Senate Department for Finance of the City State of Berlin

Prof. Dr. Ulrich Merkt
Institute of Applied Physics and Centre for Microstructure Research at the University of Hamburg

Prof. Dr. Eberhard Jaeschke
BESSY GmbH

Dr. Andrea Denker
HMI – Department SF4

Dr. Reiner Klenk
HMI – Department SE2

Scientific Advisory Board

Prof. Dr. Hans Henrik Andersen
Ørsted Laboratory, Copenhagen, Denmark

Prof. Dr. T.W. Clyne
Department of Materials Science and Metallurgy, Cambridge, UK

Prof. Dr. Dame Julia Higgins
Polymer Sciences Department of Chemical Engineering Imperial College London, London, UK

Prof. Dr. Michael Grunze
Physikalisch-Chemisches Institut
Universität Heidelberg, Heidelberg, Germany

Dr. Franz Karg
Shell Solar GmbH, Munich, Germany

Prof. Dr. Bernhard Keimer
Max-Planck-Institut für Festkörperforschung, Stuttgart, Germany

Prof. Dr. H.J. Kreuzer
Department of Physics and Atmospheric Science, Halifax, Nova Scotia Canada

Prof. Dr. Dieter Neher
Universität Potsdam Institut für Physik und Astronomie, Potsdam, Germany

Prof. Dr. W.C. Sinke
Solar Energy, Energieonderzoek Centrum Nederland (ECN) Petten, The Netherlands

Dr. Uschi Steigenberger
Science and Technology Facilities Council
Rutherford Appleton Laboratory,Harwell
Science and Innovation Campus, Didcot, UK

Prof. Dr. Lars Stolt
Solibro Research AB, Uppsala, Sveden

Prof. Dr. Martin Stutzmann
Physics Department (E25), Technische Universität München, Munich, Germany

Prof. Dr. Dr. Hartmut Zabel
Chair of Experimental Physics/Condensed Matter Physics, Faculty of Physics and Astronomy, Ruhr-Universität Bochum, Bochum, Germany

Dr. Ehrenfried Zschech
AMD Saxony LLC & Co. KG, Dresden, Germany

Organigramm HMI Berlin

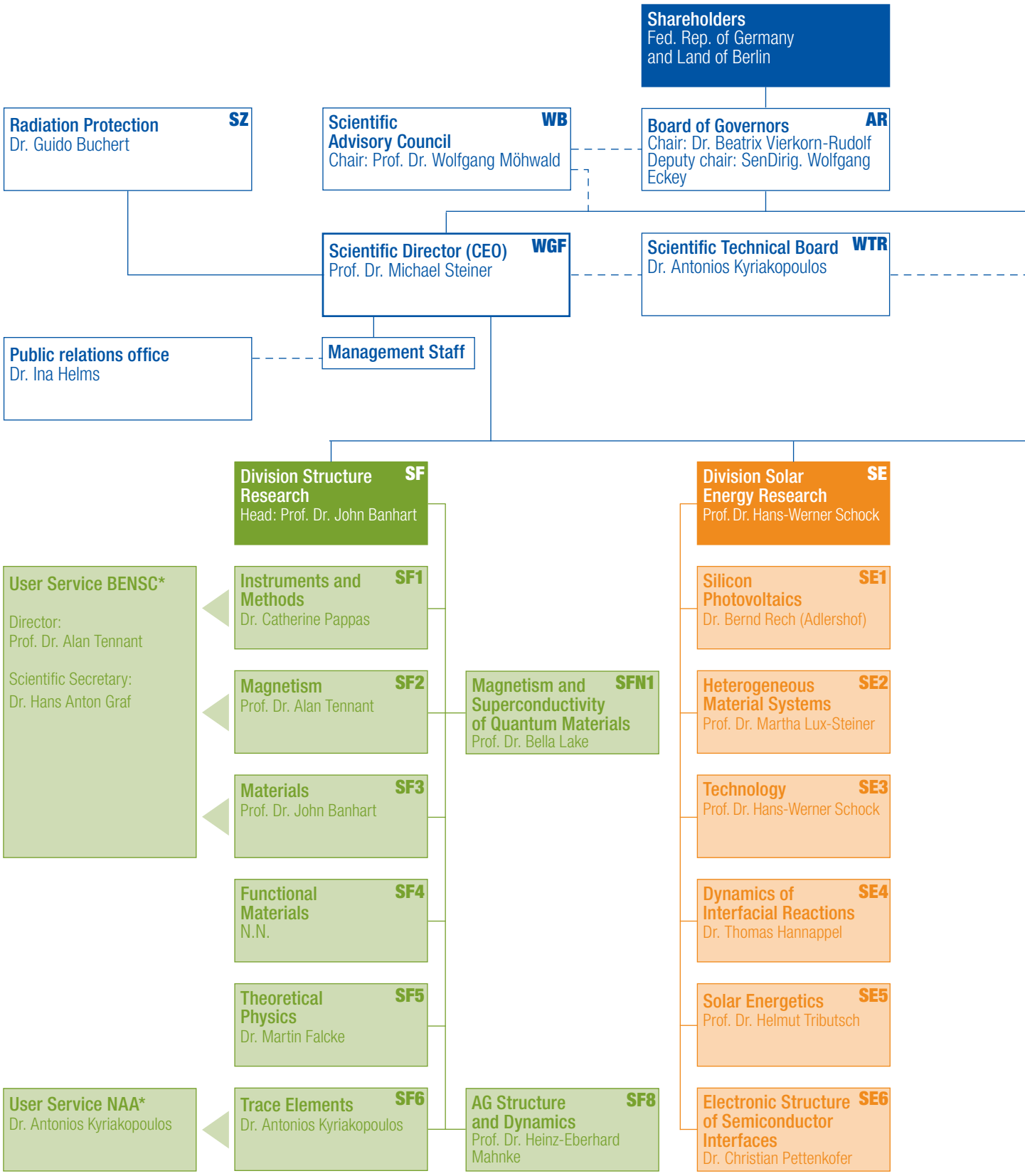

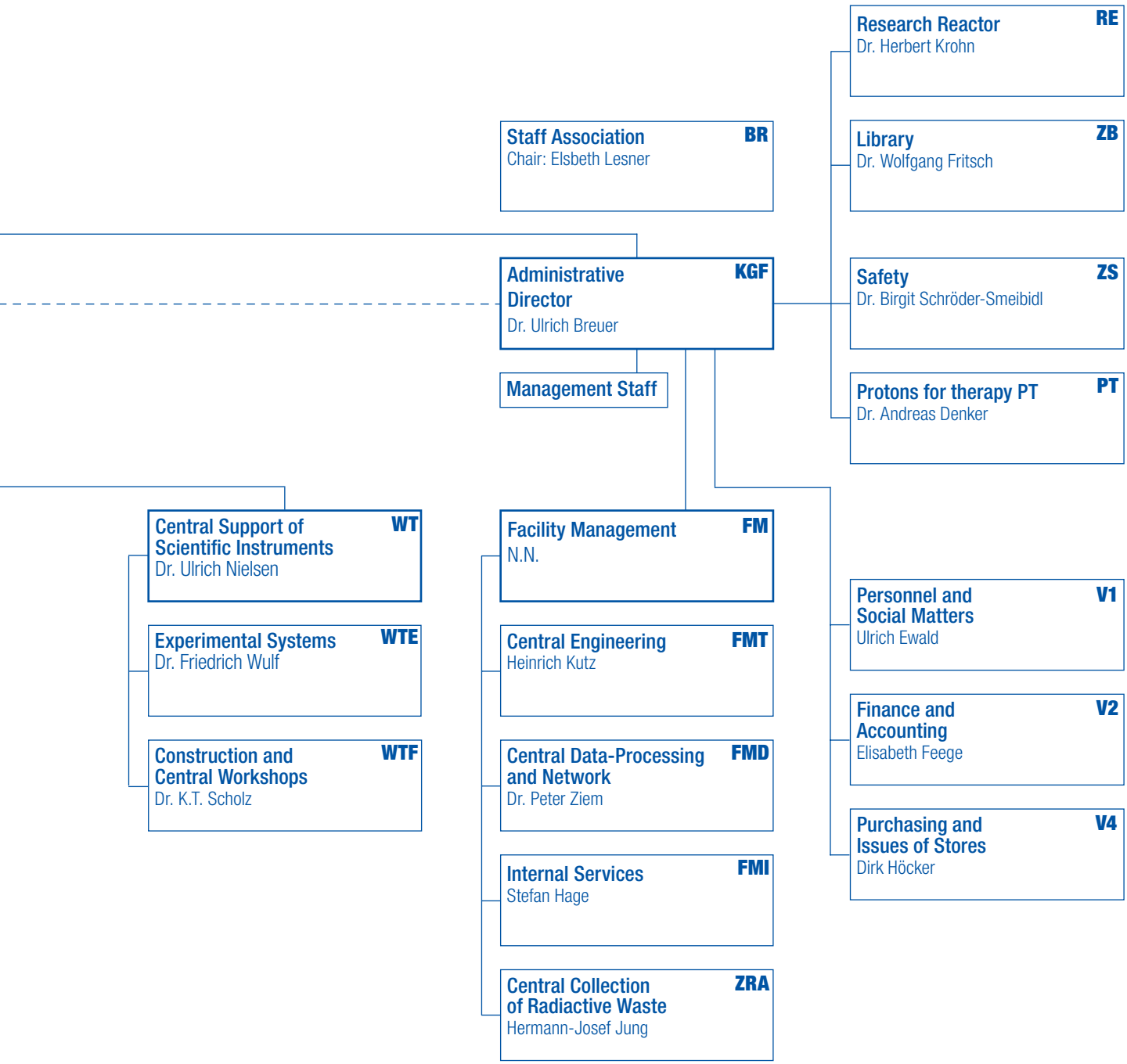

ORGANIGRAMM (Stand 09/08)

*BENSC = Berlin Neutron Scattering Center
*NAA = Neutron Activation Analysis

Imprint

1. Edition
March 2010

Annual Report 2007/2008
Selected Results

Published by
Helmholtz-Zentrum Berlin für
Materialien und Energie GmbH
Hahn-Meitner Platz 1
14109 Berlin
Germany

mail@helmholtz-berlin.de
www.helmholtz-berlin.de
Phone: (+49) (0) 30-8062-0
Fax: (+49) (0) 30-8062-2998
Member of the Helmholtz Association

Concept
Dr. Paul Piwnicki

Coordinating Editor
Erik Zürn
erik.zuern@helmholtz-berlin.de

Book Design
Frenkelson Werbeagentur, Potsdam
www.frenkelson.de

Printing
Druckerei Format, Berlin
www.formatdruck.de